UNIVERSITY COLLEGE LONDON

Faculty of Mathematics and Physical Sciences

Department of Physics & Astronomy

# *IN SITU* STUDIES OF CLAY HYDRATION FOR THE ENHANCED EXPLORATION OF OIL AND GAS

Thesis submitted for the Degree of Doctor of Philosophy of the University of London

by

Radhika Patel

Supervisors:

Prof. Neal Skipper

Prof. H Chris Greenwell

Examiners:

Prof. John Brodholt (Internal)

Dr. Stuart Clarke (External)

March 15, 2016

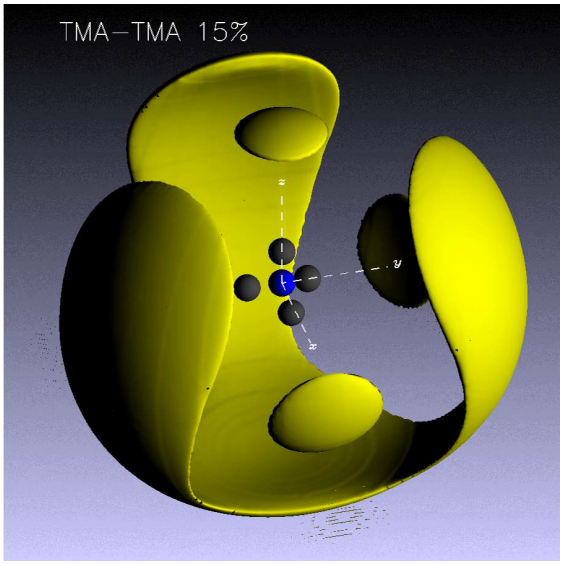


*I told you I could do it Dad.*

I, RADHIKA PATEL, confirm that the work presented in this thesis is my own. Where information has been derived from other sources, I confirm that this has been indicated in the thesis.

# Abstract

A major problem in understanding the clay and shale hydration process in oil exploration is the ability to merge information on the microscopic and macroscopic swelling nature of the minerals. Added to this, is the introduction of elevated pressures and temperatures in forming a realistic picture of these processes.

In this project, I present neutron diffraction experiments from 22°C and 50 bar to 140°C and 600 bar pressure in conjunction with isotopic substitution of hydrogen for deuterium, to determine full orientational structure of hydrophobic, clay swelling inhibitors tetramethylammonium chloride (TMA Cl) and intersolvent structure of hexamethylenediamine (HMDA) at 22°C and 1 bar. An increase in the intersolvent structure was observed within the inhibitor solution compared to bulk however followed bulk like trends with increasing p & T. Also investigated, for the first time at these elevated conditions, is the effect of TMA and HMDA inhibitors on the swelling response of vermiculites. Aside from an initial *d*-spacing increase of ∼3 %, no further interlayer expansion of the Li-vermiculites or TMA-vermiculites was observed with $HMDA_{(aq)}$ or $D_2O$ flooding respectively and increasing p & T.

Conversely, macroscopic swelling measurements performed primarily on compacted Li and TMA-vermiculite samples, using a bespoke rig, have shown that there is fluid absorption and a height increase of up to 50% upon flooding with water, brine and $HMDA_{(aq)}$. Spin-echo small angle neutron scattering was employed to investigate the route of fluid into the compacted clay. Intuitively, it revealed that large pores fill before smaller (interlayer) pores highlighting that the locus of the swelling problem may shift to within the meso-macro pore spaces of the natural shale.

Highlighting the speeds at which interlayer water diffuses, quasi-elastic neutron scat-

tering performed on hydrated terephthalate (TA) exchanged layered double hydroxides showed that the terephthalate does not contribute to the translational diffusion of the system even at water content of 1:16.24 TA:water and up to temperatures of 320 K. A slightly elevated $D_{trans} = 6.0 \times 10^{-9} m^2 s^{-1}$ for the interlayer water was measured at 320 K.

# Acknowledgements

With much respect, I wish to thank my primary supervisor Professor Neal Skipper for his unerring patience, guidance and his ability to turn every negative into a positive! Also my second supervisor Professor Chris Greenwell, for inviting me to work with his wonderful group in Durham. I would like to thank Mike Hodder and Steve Cliffe at M-I Swaco for generously providing my with a CASE sponsorship and agreeing to host and supervise me in Aberdeen.

I express my sincerest gratitude to the instrument scientists at ISIS, especially the high pressure engineers and Dr. Tristan Youngs who truly went beyond the call of duty during difficult neutron experiments. In a similar vein, also to Stephen Lishman in Durham, for his help in the manufacture and improvements of my swell-o-meter. I must also thank Dr. Alan Soper, Dr. Daniel Bowron and the rest of the EPSR community for all their helpful hints along the way!

Many invaluable and difficult lessons have been learnt with Dr. David Buckley, Dr. Patrick Cullen and Dr. Chris Howard who have been very much like big brothers: irritating all of the time but also always there with wisdom and support in all aspects of life. I am also very grateful for the enjoyable working environment created by the F10b crew over the years.

I respectfully acknowledge my family for accommodating my love for physics. Without them, none of this work would be possible.

Finally I thank you too, Dr. Seto Balian, not only for your incredible patience as I write but for reminding me of the joys of hard work and for leading by example which we must all remember to do.

# Contents

# List of Figures

# List of Tables

# Chapter 1

# Introduction

Clay minerals, such as kaolinite, illite, vermiculites and smectites are naturally occurring layered alumino-silicates and together with water, they are the most commonly found material in the earths crust[11–13]. They are the main constituents in shale, a sedimentary rock composed of high clay mineral content, mud and small fragments of other minerals like quartz and calcite[14]. The hard laminar form associated with shale is due to the chemical change of smectite to anhydrous illite transformation which is a major diagenetic reaction that occurs in the Earths crust[15–17]. The conditions and timescales along which this occurs are also ideal for the transformation of organic matter (OM) to petroleum hydrocarbons[14] and thus shale is readily encountered during the exploration of oil and gas. Due to their high clay mineral content, the chemical and physical properties of shales are very much governed by the phases of clay present within them.

Clay minerals are composed of stacks of 2-dimensional layers, with each layer carrying a net negative charge. To balance this charge, there are counter-ions, namely sodium and calcium in the inter-layer region[13]. Driven by the high enthalpy of hydration of these counter-ions, water and other polar molecules readily enter the inter-layer region causing the clay mineral to swell as the layers move apart to accommodate the additional water. This interlayer crystalline swelling occurs in a stepwise fashion from one to four layers of water under increasing humidity, a phenomenon which has been widely studied and is quite well understood[18–23].

Thus, reactive (high expandable clay mineral content) shale will also undergo macro-

scopic swelling[24]. Further expansion is caused between clay quasi-crystals in the pore spaces, osmotic swelling and is typically governed by longer-range electrostatic forces[13,18,19,22]. This allows the absorption of unlimited amounts of water between clay quasi-crystals which can lead to full delamination of the clay mineral. It has thus been been proposed that the mechanisms and time scales of this osmotic capillary swelling have a far greater impact on the bulk swelling of the clay minerals and hence to shale deformation compared to the crystalline regime of interlayer swelling[25,26]. Alongside this, illitic and kaolinitic shales may also be unstable[27,28], inferring that interlayer expansion cannot therefore be considered as the sole mechanism causing shale instability.

Swelling of reactive shale formations is particularly problematic to the oil and gas exploration sector as the oil/gas reservoir will have often have a mud stone/shale cap-rock with high swelling clay content[29]. As water-based drilling fluids (WBDF) are increasingly being used over oil and synthetic-based drilling fluids (OBDF & SBDF) for oil and gas exploration, swelling of the reactive shale formation is a real problem. This is due to the recent implementation of stringent laws governing acceptable drilling fluid impact on the environment[30] and the costs associated with the disposal of oil-contaminated waste. Bulk swelling of the shale formation is extremely problematic during drilling operations as it results in both short-term and long-term issues of agglomeration of drilled cuttings on the drill-bit and wellbore instability respectively. Thus leading to loss of production costs estimated as greater than $500 M per annum, particularly in North Sea fields[31,32]. It is therefore useful to investigate the effects of pressure and temperature on the swelling properties and pore-fluid structure of these minerals and the drilling fluid inhibitors alongside diffusive motion of water and inhibitors within the materials. This will allow for a better understanding of fluid processes akin to those encountered in the well-bore and to improve on current methods of clay swelling inhibition for both the short and long-term problems.

There are limited experimental studies into the combined effects of pressure and temperature on the swelling of clay minerals and experiments have mostly been designed to investigate the crystalline swelling in pure phases of clay minerals with Group 1 and 2 metal interlayer cations. Studies on smectite dehydration using synchrotron sources and diamond anvil cells, revealed a three to two layer hydrate with increasing pressure and temperature[33–35]. Similarly for vermiculites in the presence of hydrostatic pressure and temperature, a decrease in $d$-spacing also occurs[36] however at slightly lower temperatures

than for those observed for smectites. Na-smectites in brine solutions under elevated conditions[37] however showed no changes in the *d*-spacing inferring that the mineral exists as a two-layer hydrate. This is supported by computer simulations showing evidence for enthalpy driven dehydration of Na-smectites at increased pressures temperatures and the stability of 1-2 water layer hydrates[38–41]. Focussing more on clay-water-inhibitor systems, neutron scattering investigations into the effect of hydrostatic pressures on the osmotic swelling of alkylammonium-exchanged vermiculite showed that the there was a five and a half times increase in the *d*-spacing as the pressure was increased from ambient to 2000 bar[42]. This was attributed to the favourable entropy change with the change in volume from the compacted to swollen phase however this work was not accompanied with any increasing applied temperature. Conversely, MD simulations[43] show that compounds with long hydrophobic backbones and charged end groups may serve best as clay swelling inhibitors since they can cation exchange with the existing interlayer counter-ions and interaction of water molecules with the hydrophobic backbones would be unfavourable helping to keep water out from the interlayer.

The method of re-compaction is a standard technique used to study the macroscopic response of the wellbore clay and shales[44,45] however this introduces capillarity effects with the introduction of air at atmospheric pressures[46]. Moreover at depth, samples remain saturated with extremely low suction pressures[24,46] demonstrated by the fact that preserved shale samples remained inert when immersed in water in laboratory conditions[47]. On the other hand, Wyoming Bentonite is particularly good as a synthetic shale for its observable swelling properties, thought to be due to its low porosity when compared to different types of bentonite[48], and is therefore a useful indicator for the effectiveness of swelling inhibitors[49,50]. However the simplicity of the Wyoming bentonite becomes invalid when considering the larger non-clay content found in natural shales and thus the wider variety of pore sizes[51] as well as the diagenetic and sedimentary features found in a typical shale.

There is limited information on the combined effect of pressure and temperature on clay-water-inhibitor systems which we aim to investigate. There is also a gap in our understanding of how the microscopic swelling properties translate to the macroscopic effects observed in the wellbore which we also aim to bridge. We aim to primarily use neutron scattering to investigate the swelling behaviour of clay-inhibitor systems at these elevated pressures and temperatures alongside investigations of their macroscopic swelling

in order to optimise and refine clay swelling inhibitive methods for use in the oil industry.

# Chapter 2

# Background and Motivation

This section aims to brief the reader in the fields applicable to this work and to introduce the scientific and technological motivation for *in situ* studies of clay hydration. The chapter reviews the relevant aspects of the hydration of clay minerals science, explains the application of clay minerals in oil and gas exploration and reviews the hydration inhibition techniques currently in use for their optimisation and refinement.

For more detailed information on the structure and chemistry of clay minerals see *Crystal Structure of Clay Minerals and their X-ray Identification*[13] and *Chemistry of Clays and Clay Minerals*[19].

## 2.1 Structure of Clays

Clay minerals are formed from two structural elements: corner sharing $YO_4$ tetrahedra forming an infinite two-dimensional sheet; and edge linked octahedral cations Z of composition $ZO_6$ to form another two-dimensional sheet. In a perfect case, the tetrahedral co-ordinated Y cation is $Si^{4+}$ and the octahedral co-ordinated Z cation is $Al^{3+}$ or $Mg^{2+}$ as shown in Figure2.1.

These tetrahedral (T) and octahedral (O) sheets alternate giving the clay its layered structure to form clay platelets and the name phyllosilicate.

When one tetrahedral sheet is linked to one octahedral sheet as the repeated unit, a T-O or 1:1 clay layer is formed as in kaolinite($Al_2Si_2O_5(OH)_4$)[19]; when one octahedral

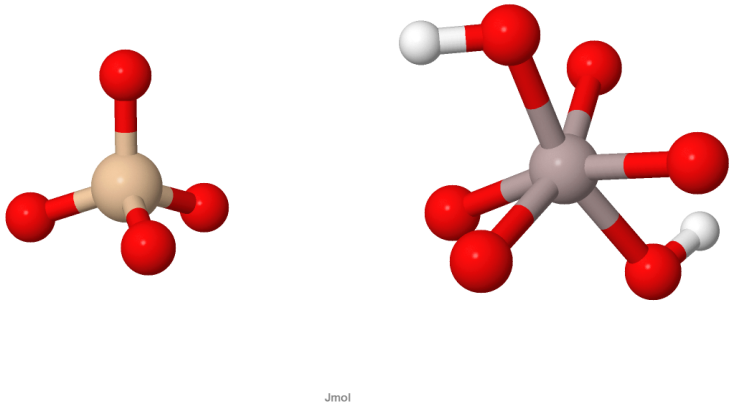


(a) (b)

Figure 2.1: Building blocks of clay sheets in their condensate trimorphic form. In these structures, O=red, H=white, Si=beige, Al=grey. **(a)**:tetrahedral building block of clay sheet. **(b)**:octahedral building block of clay sheet.

| Mineral Group | | Nature of Octahedral Sheet(s) | | Structural Formula | Negative charge per silicate layer |
|---|---|---|---|---|---|
| 1. | Kaolinite | 1:1 | dioct | $Y_4Z_4O_{10}(OH)_8$ | 0 |
| | Serpentine | 1:1 | trioct | $Y_6Z_4O_{10}(OH)_8$ | 0 |
| 2. | Pyrophyllite | 2:1 | dioct | $Y_4Z_8O_{20}(OH)_4$ | 0 |
| | Talc | 2:1 | trioct | $Y_6Z_8O_{20}(OH)_4$ | 0 |
| 3. | Micas | 2:1 | dioct | $Y_4Z_8O_{20}(OH)_4$ | 2 |
| | | 2:1 | trioct | $Y_6Z_8O_{20}(OH)_4$ | 2 |
| | Brittle micas | 2:1 | dioct | $Y_4Z_8O_{20}(OH)_4$ | 4 |
| | | 2:1 | trioct | $Y_6Z_8O_{20}(OH)_4$ | 4 |
| 4. | Chlorite | 2:1 | dioct | $Y_4Z_8O_{20}(OH)_4$ | variable |
| | | 2:1 | di,trioct | $Y_4Z_8O_{20}(OH)_4$ | variable |
| | | 2:1 | trioct | $Y_6Z_8O_{20}(OH)_4$ | variable |
| 5. | Smectite | 2:1 | dioct | $Y_4Z_8O_{20}(OH)_4$ | 0.5 - 1.2 |
| | | 2:1 | trioct | $Y_6Z_8O_{20}(OH)_4$ | 0.5 - 1.2 |
| | Vermiculite | 2:1 | dioct | $Y_4Z_8O_{20}(OH)_4$ | 1.2 - 1.9 |
| | | 2:1 | trioct | $Y_6Z_8O_{20}(OH)_4$ | 1.2 - 1.9 |
| 6. | Palygorskite | - | - | $Y_4Z_8O_{20}(OH)_2(OH_2)_4$ | - |
| | Sepiolite | - | - | $Y_8Z_{12}O_{30}(OH)_4(OH_2)_4$ | - |

Table 2.1: Classification and generalised structural formulae of phyllosilicates. Dioct - dioctahedral clay, trioct - trioctahedral clay.

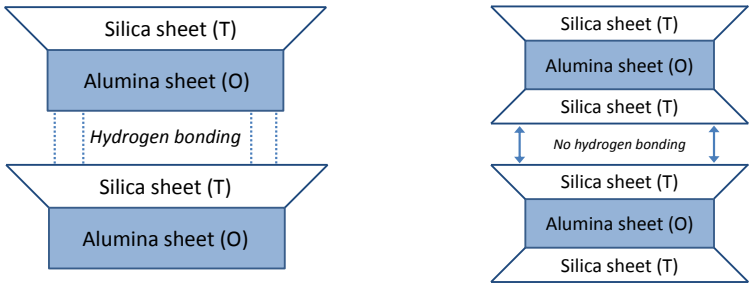


(a) (b)

Figure 2.2: Illustrations of the structure of **(a)**:1:1 clay minerals, **(b)**: 2:1 clay minerals. Compared with the 1:1 case, no hydrogen bonding between platelets occurs for the 2:1 case.

sheet is sandwiched between two tetrahedral sheets a, a T-O-T or 2:1 clay is formed as in talc and vermiculite as shown in Figure 2.2.

The unshared oxygen atoms from the octahedral sheet become hydroxyl groups ($OH^-$) which extend into the centre of the hexagonal cavities of the tetrahedral sheet. In order to obtain charge neutrality, all positions in the octahedral sheet must be occupied in the case of $Mg^{2+}$ however only 2/3 of positions need be filled in the case of $Al^{3+}$ thus generating vacancies in this layer. We therefore obtain two further subgroups for classifying clay types according to the composition of this octahedral sheet:

- Trioctahedral when all positions in the octahedral layer are filled, e.g. $Mg^{2+}$.
- Dioctahedral when 2/3 of the positions in the octahedral layer are filled and the remaining sites are vacant, e.g. $Al^{3+}$.

When these clay minerals were formed in the Earths crust, $Si^{4+}$, $Al^{3+}$ and $Mg^{2+}$ were not always present in the correct ratios so perfect cases of 1:1 and 2:1 clay minerals are uncommon. Instead, these cations underwent isomorphic substitution and were replaced by cations of similar size but of lower valence leaving the clay sheets with a permanent net negative charge. In the tetrahedral sheet, the $Si^{4+}$ is replaced by $Al^{3+}$ and in the octahedral sheet, typically there is a distribution of $Al^{3+}$, $Mg^{2+}$, $Fe^{3+}$ and $Fe^{2+}$. The size of the layer charge is an important parameter for clay classification as shown in Table 2.1 [19]. To achieve electro-neutrality of the clay sheets, charge balancing counter-ions such as $Na^+$, $Li^+$ or $Ca^{2+}$ intercalate into the spacing between individual clay platelets or adsorb onto the surface. Clay sheets oriented with parallel $c$ axes and randomly oriented $a$ and $b$

axes[52] form clay platelets (quasi-crystals) which vary in size from microscopic in the case of smectites and macroscopic such as the vermiculites. Each quasi-crystal consists of between two to many thousand individual layers stacked together.

Water must also be present during formation of the clay minerals, thus the interlayer region may contain water in the form of (partially) hydrated balancing counter-ions. Micas do not possess water in the interlayer region, i.e. they have un-hydrated balancing counter-ions and chlorites have positively charged hydroxide sheets in the interlayer region; thus they have fixed repeated cell units of 10 Å and 14 Å respectively[19]. Hydration of the charge balancing counter-ions in smectites and vermiculites does occur and varies with humidity and therefore they have variable thicknesses. It is the hydration (solvation) of these interlayer counter-ion species that partially gives rise to the property of shale swelling.

### 2.1.1 Layered Double Hydroxides

Similarly to the chlorites, there are a class of hydrotalcite-like materials or layered double hydroxides (LDHs) which have repeating units of positively charged hydroxide sheets. They are represented by the general formula:

$$[M^{(II)}_{1-x}M^{(III)}_{x}(OH)_2]^{x+}[A^{m-}_{x/m}nH_2O]^{x-} \tag{2.1}$$

with $0.1 < x < 0.33$. The positive surface charge is as a result of partial substitution of divalent by trivalent cation and the excess layer charge is compensated by the incorporation of anions into the interlayer space. The term 'hydrotalcite' is reserved for the forms in which $Mg^{2+}$ and $Al^{3+}$ occupy the cation sites and the $CO_3^{2-}$ anions originally occupy the interlayer spacing. As with their oppositely charged clay counterparts, the charge-balancing anions draw water into the interlayer region, usually in the form of a monomolecular film as seen in Figure 2.3. The layered structure is similar to that of 1 : 1 clays.

## 2.2 Clay, Shale, Petroleum

The decomposition of organic matter (OM) under prolonged exposure to elevated pressures and temperatures and in the absence of oxygen will lead to the formation of fossil fuels.

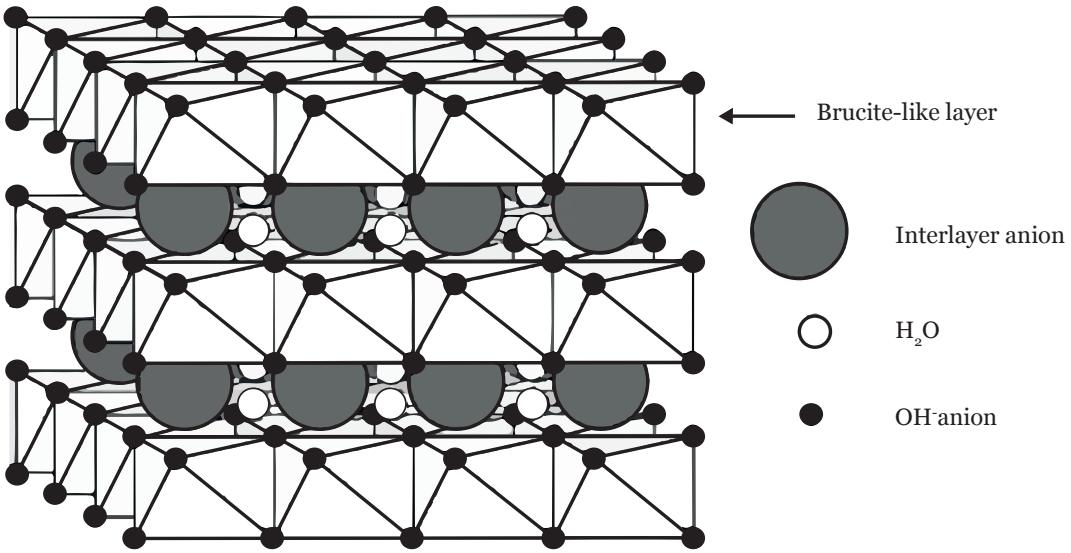


Figure 2.3: Schematic of a hydrotalcite layered double hydroxide.

The ideal temperatures and pressures required for this transformation are found in all sedimentary basins and lead to the formation of sedimentary, oil/gas sources such as sandstones, carbonates and shale.

Weathering of the Earths surface begins the formation of all clay minerals which are transported by rivers into sedimentary basins and subsequently buried. The clay mineralogy responds to the change in chemical conditions from weathering to burial in a sedimentary basin, and undergoes *diagenesis*, the irreversible, chemical transformation from one mineral to other mineral types. The clays have a long residence time in the sedimentary environment and during the burial process, organic matter and water are adsorbed onto the clays[53]. Burial is also accompanied with an increase in temperature and pressure of the environment subjecting the clays to heating over various periods of time and incurring further diagenesis. All these factors govern the route that the clay diagenesis will take, driven towards higher thermodynamic stability and thus the various proportions of clay types in the environment. The last stage of clay mineral diagenesis is the beginning of metamorphism which describes the recrystallization of the clays into larger grains and varying crystallographic compositions, as well as the creation of new silicate materials so that the phase of clay minerals no longer persists in the environment.

Porosity of a formation is a measure of the percentage of total volume that is pore-space and in the case of clay minerals, the volume occupied by interlayer fluid. Depending also on the geothermal gradient, which in the North Sea fields[14,53,54] is 30 - 40 $^{\circ}\mathrm{Ckm}^{-1}$,

we have a general formula for porosity, $\phi$ of a shale:

$$\phi = \frac{\text{bulk (wet) volume - grain (dry) volume}}{\text{bulk volume}} \tag{2.2}$$

Initial porosity of the formation is high (between 50 - 80 %[14,53]); the expandable clay minerals contain several layers of adsorbed water and have no directional arrangement at the surface. The near surface sediments are also comprised of mostly expandable clay minerals. As time is spent in burial, mechanical compaction aligns the minerals creating the bedding plane and squeezes pore-water from the sediment reducing porosity exponentially with distance[14] to approximately 20 % in the first kilometre[53]. The compaction of the clay minerals and quartz in the environment due to burial begins the formation of shale. Beyond this to about 1700 m, chemical compaction causes water to be expelled from the clay mineral lattices decreasing porosity linearly and therefore vertical permeability. This is associated with the gradual disappearance of swelling clays and the appearance of non-expandable clays, i.e. the smectite to illite transformation (I-S transformation) which is the beginning stage of metamorphism. Beyond 1700 m, porosity is reduced below 15 % alongside a drastic reduction of water permeability and at this point, the swelling clay content is enormously reduced.

The formation now has a far greater proportion of non-swelling clays such as illite or hydromica which contain no interlayer water. The general structural formula for these non-swelling clays as given by North[14] is:

$$(Al_4Fe_4Mg_4)(Si_7Al)O_{20}(OH)_4 \bullet K \tag{2.3}$$

Organic material requires subjection to moderate temperatures over long periods for the transformation to kerogen (the precursor of petroleum). This transformation occurs from shallow depths to ∼1000 m and from temperatures of 50°C up to 150°C[14,55], where one would find high expandable clay mineral content in the formation. It is a misconception that very high temperatures (300 - 400°C) are required for transformation of OM to petroleum. Instead, the OM requires subjection to moderate temperatures over long periods and therefore places swelling clays in an environment favourable for the formation of petroleum[14,55].

## 2.3 Hydration of clays

Clay minerals are subject to two types of swelling processes: i) crystalline swelling occurring between individual clay sheets involving the limited intercalation of water molecules into the interlayer spacing; ii) bulk swelling due to several different processes which will be described in Section 2.3.2 leads to unrestrained adsorption of water by the clay up to 10g $H_2O$/g clay[18] between individual clay layers and theoretically, an unlimited amount of water between quasi-crystals. Immersion of swelling clays in dilute aqueous solutions is generally when macroscopic swelling will occur and leads to formation of the clay into a gel like phase and in the case of excess water, fully dispersed clay layers, i.e. the clay quasi-crystal has completely delaminated into individual sheets within the solution. This latter type of swelling is what causes the problems specific to the hydration of clays in the oilfield.

### 2.3.1 Crystalline Swelling

Microscopic or crystalline swelling is a short-range process that occurs in discrete steps where one observes the occurrence of one to four layers (beyond this, the regime is no longer considered crystalline) in the clay interlayer under increasing relative humidities[18,23,56–58]. The extent and rate of crystalline swelling is dependent on the species of the charge balancing counter-ion and the size of the surface charge of the clay[59,60]. It has been found that water intercalation and adsorption decreases with increasing interlayer counter-ion valence; the biggest difference occurring between mono- and di-valent counter-ions[59]. This is very important when thinking about methods for the inhibition of crystalline clay mineral hydration since it is the solvation of the interlayer counter-ions which drives water into the interlayer[56,61]. This occurs in discrete steps, after which a maximum of four water layers is observed[18,19,62]. This process has been seen to be hysteretic[63] which is supported by the results of molecular simulations performed by Tambach *et al*[64] and Zheng *et al*[65].

Slade *et al*[23] observed that the counter-ions within the clay interlayer and the cations in the external solution compete for water molecules. As the interlayer counter-ion concentration is very high (∼4 molal) and if only the attractive potential energy which arises from the Coulombic attraction between the positive interlayer counter-ions and the negatively charged sites in the clay sheet, caused by isomorphous substitution, hinder the solvation of the counter-ions, very high concentrations of cations in the external solution would

| **Ion** | $Li^+$ | $Na^+$ | $K^+$ | $TMA^+$ | $Mg^{2+}$ | $Ca^{2+}$ | $Fe^{2+}$ |
|---|---|---|---|---|---|---|---|
| **Hydration Enthalpy** kJ $mol^{-1}$ | -545 | -418 | -351 | -396 (Nagano 1988)[67] | -1923 | -1653 | -1981 |

Table 2.2: Enthalpy of hydration for mono- and di-valent cations commonly found in the interlayer[7].

be needed to limit swelling. This was later verified by Laird[63] through X-ray diffraction measurements of osmotically controlled swelling in Na-smectites.

Therefore in general, it is the 2:1 smectite and vermiculite clay minerals that show the strongest swelling properties. For the 1:1 clays, the individual clay platelets are very strongly hydrogen bonded and have a very small layer charge therefore swelling of kaolinite is not usually seen. Although crystalline swelling is the necessary first stage of the very initial hydration processes of clay minerals, it only amounts to an uptake of approximately 0.5g $H_2O$/g clay and this is not enough to cause the types of problems that occur in the oil field.

#### Effect of Interlayer Counter-ions on Swelling

The effect of the type of charge balancing counter-ion present in the interlayer region is heavily correlated with the swelling properties of the clay. The role of counter-ion charge and its hydration energy in the swelling of the clay mineral is so great that it can even inhibit crystalline swelling entirely as in the case of potassium substituted clays[31,66] and subsequently, potassium levels partially govern the rate and degree to which smectites transform to anhydrous illite in a clay mineral containing formation. Table 2.2 presents the data for the enthalpy of hydration for some mono- and di-valent cations. The counter-ions are mobile within the interlayer region and when immersed in a salt solution of differing cation but same charge, the counter-ions can undergo a cation exchange reaction. The rate at which this exchange occurs for a particular clay type is called its cation exchange capacity (CEC). CEC is conventionally expressed in the units milliequivalents per gram (meq $g^{-1}$) however as it also represents a charge per unit mass, in SI units is expressed as coulombs per unit mass (C $g^{-1}$). Typically for that of a medium charge montmorillonite, the CEC is 96.5 C $g^{-1}$. Vermiculites in general have a much higher layer charge of 80 - 150 C $g^{-1}$.

Counter-ions can also be solvated with polar organic solvents such as methanol and ethyl glycol[18,66] and substituted with larger ions such as alkyl- ammonium derivatives[68–70].

The exchange of counter-ion species with these surfactants lowers the surface energy of the clay and can render the phyllosilicate compatible for polymer intercalation[71]. [43] suggested that the substitution of counter-ions with surfactants such as tetramethylammonium (TMA) and tetraethylammonium (TEA) will lower the swelling potential of clay minerals but this has yet to be studied and data on TMA exchanged vermiculite is presented in this study in chapter 5.

In this project, a variety of clay minerals and natural samples have been investigated. For the natural shale systems, counter-ion species and proportions of clay mineral depend on where the sample is quarried in terms of its geographical location and depth below the Earths surface. For the experiments involving single types of clay minerals, each set of samples have been prepared in mono-ionic form. Experimental work has well established the effect of counter-ion species for vermiculites and smectites[59,61].

### 2.3.2 Bulk Swelling

When swelling clays with specific types of interlayer counter-ion combinations are immersed in dilute aqueous solutions, the minerals can absorb water such that the spacing between individual platelets can reach 900 Å as observed in vermiculite by Crawford *et al*[72] or even become fully dispersed as in smectites[26] and other mineral combinations[73].

Before bulk swelling can occur, it has been postulated by Skipper *et al*[74] that one layer of water must exist between the interlayer counter-ions and the clay layer. This would act as a screening potential between the charges and once the attractive electrostatic forces between the counter-ions and the layers was overcome it would allow an unlimited amount of water into the interlayer region. Thus in turn, allowing osmotic access of water from the external solution into the pores and the formation of the electric double layer (EDL[75]). A portion of total negative charge of a quasi-crystal is expressed on an external surface forming one half of the electric double layer and therefore a net positive charge in the solution adjacent to that external surface, called the diffuse region of the clay platelet. When two platelets approach due to Brownian motion such that their positively charged diffuse regions overlap, an electrostatic repulsive force develops. There have been many discussions on balancing the stability of this diffuse double layer (DDL) repulsion with a long-range attractive force driven by van der Waals interaction and is described by the well-established DLVO theory[76,77] named after Derjaguinand Landau, Verwey and Overbeek.

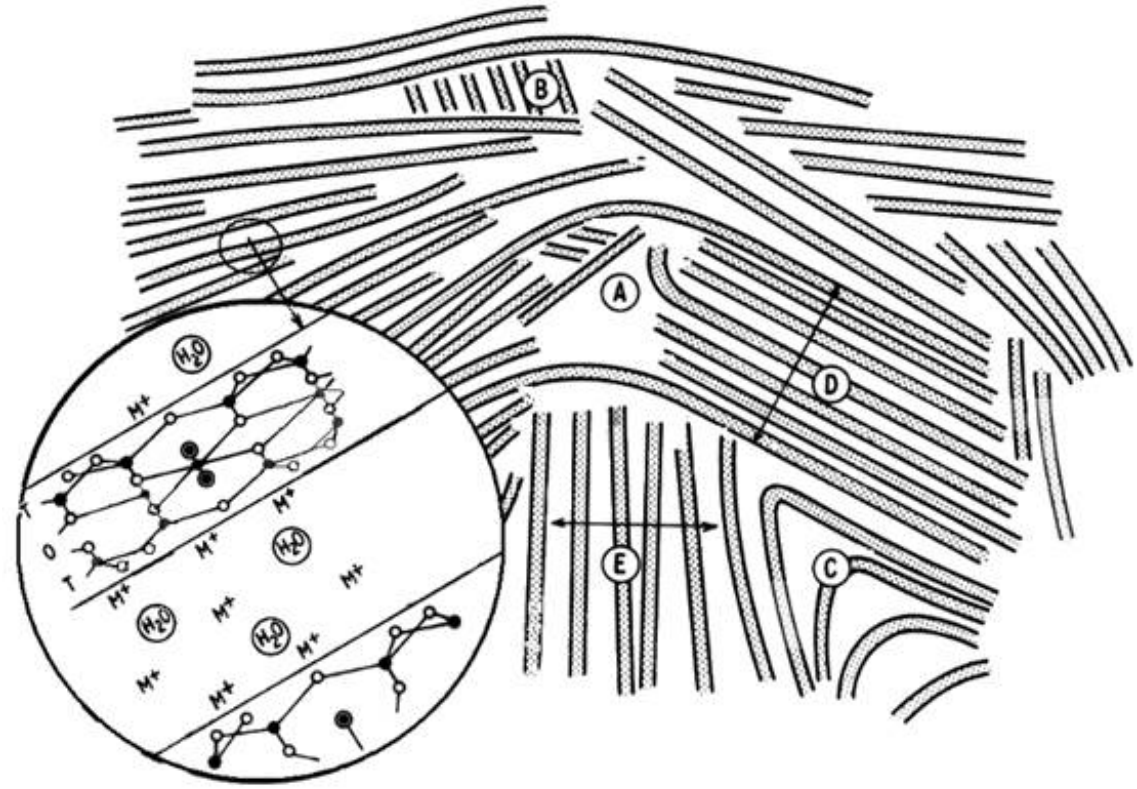


Figure 2.4: Schematic of a natural clay system[1] showing bulk arrangements of clay platelets (shaded) and structural defects A, B, C, D, E described in text. Inset shows the crystalline arrangement of montmorillonite.

### 2.3.3 Pore Swelling

The environments in which swelling clay minerals are found however, have a more complicated structure than simple layering. Due to the existence of other material in the natural sample and the compression over time, natural samples contain faults shown in Figure 2.4[1]: (A) voids, (B) edge to face stacking, (C) regions of excessive folding, (D) ordered domains and (E) disordered stacking.

When considering natural samples, swelling within the interlayer portion of the clay mineral cannot solely contribute to the total swelling response of the natural material since illitic and kaolinitic shales are also found to be unstable in the wellbore[27,28]. Though the DLVO theory describes the double-layer swelling Laird[26] describes several other processes which contribute in conjunction to macroscopic swelling of the clay including the formation and breakup of quasi-crystals, cation demixing which is a problem when clay minerals with different interlayer counter-ions are present, co-volume swelling and Brownian swelling; the latter two being entropic processes. Also, since the DDL thickness is found to be

of similar or larger magnitude than the micro and meso-pores in compressed shale, the exposed clay surfaces in the pore spaces would lead to electrostatic repulsion and increased pore/hydration pressure in these illitic and kaolinitic shales[51].

In the context of real oil drilling systems, the consideration of these processes becomes very important due to the mechanical disturbance that drilling has on the shale formations thereby exposing the pore network, (A) in Fig 2.4, of the natural clay to the drilling fluid unlike the static conditions applied in a laboratory experiment. In this situation, the problematic regions with respect to shale instability and its inhibition is moved from the interlayer of the swelling clays to the charged external surfaces of the various clay minerals that face the walls of the shale pores.

## 2.4 Effect of Pressure and Temperature on the Swelling of Clay Minerals

Investigations into the combined effect of pressure and temperature to the interlayer structure of clay minerals have traditionally been difficult to perform. This is mostly due to the difficulty in building apparatus required to be able to apply both pressure and temperature to macroscopic samples and allow incident radiation onto the material to measure the interlayer spacing. Studies on smectite dehydration using synchrotron sources by Huang *et al*[34] and Wu *et al*[35] revealed a three to two layer hydrate with increasing pressure and temperature between 200 - 605°C and 1 - 1.4kbar pressures. Increasing temperature and pressures required for dehydration were in the order Mg, Na, Ca. Previous high pressure and temperature work performed by De Sequeira *et al*[25,36] focussed on the effect of interlayer cation ( $Mg^{2+}$,$Ca^{2+}$ and $Na^{+}$) on smectites and vermiculites under hydro-static pressures and temperatures using time-of-flight neutron scattering. The results revealed a decrease (001) peak as a transition from three-layer hydrate at ambient to two-layers above 180°C and 900 bar for $Ca^{2+}$ and $Na^{+}$ however a stable interlayer *d*-spacing for $Mg^{2+}$. Conversely, n-butylammonium vermiculite in a 0.1 M solution of n-butylammonium chloride under applied hydrostatic pressures of 1050 bar at 20°C, has been observed to osmotically swell to an expanded *d*-spacing 6 times of the original *c*-axis value[42]. The process was found to be entropically favourable with the volume change of the phase transition.

More recently, there have been advances in high pressure chambers developed to study mineral interactions with gasses at elevated pressures and temperature developed

by Koster van Groos and Guggenheim[78]. Their work however focussed on the response of smectites under $CO^{2+}$ pressure in increasing brine concentration solutions with applications in enhanced oil recovery (EOR).

## 2.5 Problems faced in the oil field

Swelling is a general property of clay minerals and occurs in many parts of the drilling process. However, this project is focused on studying the effects of WBDF when they initially come into contact with the reactive shale at the very start of the drilling process and studying the hydration of the rock foundation and the drilling fluid itself during the first five minutes of the drilling process.

### 2.5.1 Role of Drilling Fluid

For a comprehensive review of the role of drilling fluids see *Composition and Properties of Drilling and Completion Fluids* by Gray[79]. In conjunction with minimising the hydration of the surrounding shale formation, the drilling fluid has many functions:

- **Control subsurface pressures.**

In order to compensate for the loss in pressure when a well-bore is drilled, the drilling fluid must have sufficient density to maintain the subsurface pressure. I.e. The density of the fluid must match or be higher than that of the formation.

- **Remove cuttings from the well.**

When drilling the well bore, the shale excavated to create the well must be removed efficiently and effectively such that blockage of the hole does not occur.

- **Minimise damage to the oil reservoir** through prevention of the inflow of fluids (oil/gas/water) into permeable rocks penetrated.

- **Maintain the stability of uncased sections of the borehole.**

- **Optimise the drilling process through:**

  - Maintenance of Rates of Penetration (R.O.P.). This is the speed at which the drill-bit breaks the rock under it, typically measured in *metres per hour*.

  - Lubrication of the drill bit and drill string (the assembly of drill pipes behind the drill-bit).

In order to keep the process cost effective, the drilling fluid must allow for drilling rates (R.O.P.) to be maintained and lubrication of the drill-bit is key to this.

- Assist in the collection and interpretation of information available from the drilling cuttings, cores, fluid sampling and electrical logs detailing the resistivity of the geological formations penetrated by a borehole (this requires a conductive medium).

- **Compliance with HSE acceptability.** The drilling fluid *must* comply with the Health and Safety Executive regulations set out as in the HSE safety reports[80] for the North Sea area. A risk assessment scheme can also be found in the CHARM[81] report.

Oil-based drilling fluids (OBDF) are the most effective at keeping formation damage to a minimum and providing well-bore stability as well as being excellent lubricants for the drill-bit, therefore maintaining high R.O.P. and returning drilled cuttings back to the surface. OBDF are also more effective at meeting the other drilling fluid functions such as having temperature stability. However due to the revised environmental laws describing the correct treatment of oil-contaminated waste cuttings and off-shore regulations[80], this leads to huge increases in costs due to the difficulty in containment and disposal of these cuttings and used drilling fluid[82]. The requirements for the treatment of waste when using OBDF thus pose a problem towards the industrys drive for improved cost-effectiveness.

Hence a huge shift has been made towards using water-based drilling fluids as the dangers to the environment and treatment of cuttings and fluid are minimised. However there are some cases when OBDF are currently the only option. For example in very deep wells when the fluid may be subject to extremely high pressures and temperatures as there is no stability of WBDF above 250°C[83].

Despite this, water based drilling fluids are still preferential in their use due to their compliance with environmental laws.

### 2.5.2 Problems of Clay Swelling in the Oilfield.

This move to the increased use of WBDF in the oil field introduces water into the clay mineral containing shale formation and therefore the problems associated with uncontrolled

hydration/dehydration of the clay minerals.

- **Cuttings disintegration.**

With the release of the cutting from the formation, the *in situ* stresses are suddenly released and the fluid that makes up the drilling mud has an opportunity to infiltrate the cuttings. If the mud pressure is too low then water and other additives in the drilling fluid will enter the cuttings thereby causing them to break apart.

- **Well-bore instability.**

Pore network of shale allows filtrate to invade into shale along a pressure gradient and therefore hydration of clay minerals in the rock formation. This causes sloughing of the walls of the well-bore leading to mechanical failure of the rock due to softening of the formation and increased pore pressure.

- **Agglomeration of drilled cuttings.**
  The hydration of drilled cuttings softens them due to the water uptake by the clay minerals. This makes them plastic like[29] and "sticky" therefore leading to:
  - **Reduced hole-cleaning efficiency.** - Softened cuttings stick to the drill-string and are difficult to remove.
  - **Stuck pipe and difficulty when running casing.**
  - **Bit-balling.** - this is a problem due to the cuttings sticking to the drill-bit and thereby reducing its efficiency at drilling the wellbore.
  - **Reduced R.O.P.**

The most effective method of clay swelling inhibition is to use oil-based muds as they do not invade the cuttings or the rock formation. They provide a solution to reducing the risk of clay agglomeration and therefore bit-balling to maintain high rates of penetration. This is not a long-term solution to clay hydration inhibition however due to the environmental difficulties associated with oil based muds[84] and subsequently the huge costs in the treatment and disposal of oil-contaminated cuttings.

## 2.6 Current solutions for the inhibition of clay hydration

There are many ways in which inhibition of clay hydration is addressed governed by the chemo-mechanical properties of the formation encountered and the conditions which the formation is subject to. Whether the oil/gas reservoir is on-shore or off-shore also plays an important role. Thus, many factors have to be taken into consideration before a specific inhibition method is chosen. For ease of comparison, the following swelling inhibitor solutions have been arranged chronologically. A comprehensive study into the problems associated with the swelling of shales in the oilfield and current inhibitive methods has been performed by Van Oort[29] and Anderson[32].

### 2.6.1 Potassium Chloride (KCl)

Traditionally, the solution when using WBDF has been to add large concentrations of potassium chloride into the drilling fluid. If $K^+$ is added in excess, it undergoes cation exchange with existing counter-ions present in the clay and due to its low enthalpy of hydration[31,85], inhibits the swelling of the clay minerals. Conveniently, $K^+$ is approximately the same size as the interlayer spacing which aids in keeping it unhydrated.

### 2.6.2 Surfactant muds

#### Partially-hydrolysed Polyacrylamide (PHPA)

$K^+$ is generally used in conjunction with other polymer compounds which act to displace the water molecules around the pillared cations. One of the first polymers to be used in conjunction with potassium chloride is partially hydrolysed polyacrylamide (PHPA). PHPA is a water-soluble anionic synthetic polymer with a high molecular weight. It is believed to seal micro-fractures and coat shale surfaces with a thin filter-cake making it impermeable to water. PHPA therefore helps maintain pressures within the formation and inhibits dispersion and disintegration of cuttings[86]. PHPA has become the precursor to developing and using hydrogels that are formed *in situ* and thus more efficient at blocking pore throats and keep individual clay platelets from dispersing[87]. This does improve the stability of the shale formations but does not eliminate the swelling from the shale completely[88].

**Glycol Additives**

Muds containing the addition of glycols, glycerols and polyalkylene glycols have been used since the genesis of oil exploration. Polyols are a useful addition to WBDF as they form monolayers in the interlayer region in the presence of $K^+$ [89]. Polyglycol/glycerol alone does not inhibit shale swelling but needs the presence of KCl to be effective as they require potassium to bind to as opposed to binding to layers themselves.

It is believed that the glycol added to the drilling fluid disrupts the hydrogen bonding network of water with the siloxane surface, i.e. displaces water molecules. $Na^+$, $Li^+$ and $Ca^{2+}$ have higher charge density therefore more difficult to remove solvated water from around these ions. However there is still a controversy over the inhibition mechanisms of polyol additives.

These polyols are seen to work at large depths however they cannot be used at high temperatures $> 150°C$ as the surfactants become thermally unstable [90]. It is therefore of interest to use polyalkalene glycols. The stability of the carbon-carbon double bond means that they can be used to temperatures up to 250°C in the absence of oxygen which is the environment in which oil and gas is found [91].

As shown by Liu *et al* [92], glycols are most effective when used in conjunction with KCl however, potassium as an inhibitor is environmentally undesirable and in some areas, such as the Gulf of Mexico, high concentrations of potassium are not permitted having a negative impact on the performance of most glycols. Thus, there is a clear need for potassium-free WBDF to perform as a viable alternative.

### 2.6.3 Silicates

Soluble silicates invade into the shale and react with ions in the pore fluid forming insoluble precipitates. The precipitates form a coating around shale cutting, known as a "silicate-cake", which act as an osmotic membrane preventing flow of water into the shale but still allowing osmotic transfer of water observed by Van Oort *et al* [93]. This property is then exploited as chemical potential gradients can be set-up using high concentrations of $K^+$ or $Na^+$ to dehydrate the shale. Silicates are most often used in conjunction with KCl.

### 2.6.4 Amine chemistry

The advantages of using amines as swelling inhibitors has been known for some time[94], but it is only recently that the mechanisms behind the behaviour of amines have been probed for their exploitation.

Due to the similar hydration volume (ionic radius) that the ammonium cation, $NH_4^+$, has to the potassium ion, it was thought that ammonium salt derivatives could be used in an analogous way to potassium chloride. By performing Fourier Transform Infrared Spectroscopy (FT-IR) of PPO-$NH_2$ intercalated $Na^+$-montmorillonite, Greenwell *et al*[95] showed that significant H-bonding occurs between the unprotonated amines and clay surfaces; this was also observed through performing similar studies on diamines by Zhong *et al*[49]. For the case of the protonated ammonium ion however, it has long been known that it ion exchanges with the interlayer cation[96]. Thus, the two mechanisms via which amines can inhibit clay swelling are *i*) direct cation exchange of ammonium ions with the interlayer counterion and *ii*) intercalation of amine into the interlayer region where the amine groups hydrogen bond with the siloxane surface.

The simplest quaternary ammonium salt is tetramethylammonium chloride(TMACl)[1], $(CH_3)_4N^+$, which has been used for shale swelling inhibition along with other higher molecular weight quaternary ammonium salts[97] (see Table 2.2). Research beyond the small $TMA^+$ ion has shown that longer chain amines such as hexamethylene diamine (HMDA) perform better as swelling inhibitors as they can be synthesized to have hydrophobic backbones which help keep water out of the interlayer region once they have been expelled by the exchange of the ammonium headgroups with the clay counterions[49,98]. Not only is there a reduction of water in the interlayer region but once the amines are bound to the surface of the clay layers, Xuan *et al*[99] have shown using X-ray photoelectron spectroscopy and zeta-potential measurements, that for the case of dopamine(DA) intercalated montmorillonite, the DA monomers polymerize in the interlayer region. At high enough monomer concentration, this polymerization eventually leads to the collapse of the diffuse double layer causing aggregation of clay platelets.

Inhibitor synthesis based on ammonium salts has boosted the WBDF use as they can be used without the presence of KCl thus can be used on land and in areas where there is a requirement of low salinity[94,100–104]. However they are far from being optimised as

[1]It should be noted that in industry, tetramethylammonium chloride is referred to as TMAC.

there is a lack of information on the structure and behaviour of amine-intercalated clays when subjected to burial conditions. Investigating the effects of elevated pressures and temperatures on the structure of clay intercalated ammonium salts and polymeric amines, will form the basis of the large-scale experiments performed for this project.

# Chapter 3

# Characterisation Through Scattering

Neutron and X-ray scattering are excellent tools for investigations into the structure and dynamics of matter. The experimental techniques used in this PhD. to investigate the structure of clay-drilling fluid-inhibitor systems were neutron and X-ray diffraction, time-of-flight and spin-echo small angle neutron scattering (SANS) and quasi-elastic neutron scattering (QENS).

## 3.1 Neutron Scattering

Neutrons are uncharged particles. They are therefore able to penetrate deeply into matter without interaction or destruction of the material unlike X-rays and electrons. The de Broglie relationship for neutrons permits the tuning of neutron velocities (energies) such that they are comparable to that of inter-atomic spacing and molecular excitations. Neutron wavelengths can also be tuned to those of larger scale structures comparable to those within amorphous systems permitting the study of artifacts which are microns in size, for example pore spaces within the clay matrix. They also have a magnetic moment enabling the study of magnetic structures and excitations using spin polarised neutrons.

Neutrons are scattered by the strong nuclear force with a magnitude dependent on the spin state and composition of the scattering nucleus. This is in contrast to the scattering

of X-rays from the electrons, the magnitude of which increases with atomic number. Thus it is very difficult using X-rays to see a low mass atom in a system of heavier ones or to differentiate between atoms with similar mass numbers. In general for neutrons, the light elements such as H, C, N and O, which predominate in pore and interlayer fluids and also form the basis of many clay swelling inhibitor species, scatter neutrons strongly (Table 3.2). The magnitude of the neutron scattering varies between isotopes of the same element[8] enabling the use of the powerful technique of isotopic labeling and allows the separation of individual correlation functions from the average correlation function achieved in a diffraction measurement. This technique is especially sensitive to hydrogen and deuterium and therefore can be used to 'highlight' different aspects of the clay-water-inhibitor system[105]. One can also manipulate the neutron scattering lengths of certain metals to create null-scattering sample containers (Table 3.2). Titanium-zirconium sample cells are used for sample containment as the alloy is chemically unreactive, mechanically strong and invisible to neutrons. This makes neutron diffraction a very powerful tool for structural studies of systems containing hydrogenous fluids and neutron spectroscopy for perturbing the dynamics of water and aqueous solutions.

By far the biggest drawbacks of neutron scattering experiments are those associated with the problem of low neutron flux. This makes experiments performed with neutrons slow and expensive and potentially difficult to study quick, time-dependent processes. However, the information derived from these experiments is second-to-none.

This chapter concentrates on the theory of neutron scattering and the application of diffraction and spectroscopy to the study of clay–drilling fluid systems under *in situ* burial conditions. For a more detailed treatment of the relevant theories behind neutron diffraction and spectroscopy, see *Theory of Neutron Scattering from Condensed Matter*[8]. For an overview of experimental techniques involved see *Experimental Neutron Scattering*[2].

### 3.1.1 Neutron Properties

The neutron is a subatomic nuclear particle; its basic properties are shown in Table 3.1.

The momentum, $\vec{p}$, of a neutron is given by:

$$\vec{p} = \hbar\vec{k} \tag{3.1}$$

where $\vec{k}$ is the wave-vector of the neutron, the magnitude of which is given by $|\vec{k}| = \frac{2\pi}{\lambda}$

| Property | Magnitude |
|---|---|
| Mass | 1.775 x $10^{-27}$ kg |
| Charge | 0 |
| Spin | $\frac{1}{2}$ |
| Magnetic dipole moment | $-1.93\mu_N$ |

Table 3.1: Basic neutron properties.

and $\lambda$ is the de Broglie wavelength of the neutron. The neutron velocity, $\nu$, is given by:

$$\nu = \frac{\hbar k}{m} \tag{3.2}$$

The neutron energy is related to its wavevector by:

$$E = \frac{\hbar^2 k^2}{2m} = \hbar\omega \tag{3.3}$$

where $\omega$ is related to $\vec{k}$ through the dispersion relation, $\omega = \frac{\hbar k^2}{2m}$.

### 3.1.2 Neutron Scattering Geometry

In a neutron scattering experiment, a beam of neutrons with initial wave vector and energy $(\vec{k_0}, E_0)$ interacts with the sample and is scattered with wave vector and energy $(\vec{k_1}, E_1)$. A full description of the scattering process requires information of the momentum transfer between incident and scattered beam, known as the scattering vector, $\vec{Q}$ and the energy transfer, $\Delta E$.

$$\hbar\vec{Q} = \hbar\vec{k_0} - \hbar\vec{k_1} \tag{3.4}$$

and

$$\Delta E = \hbar\omega = E_0 - E_1 \tag{3.5}$$

A visual representation of $\vec{Q}$ can be seen in Figure 3.1.

If the magnitude of $\vec{k_1}$ is less than $\vec{k_0}$, the scattering process is inelastic and some energy must have been transferred to the sample. However in a diffraction experiment, the scattering event is elastic and $|\vec{k_1}| = |\vec{k_0}|$.

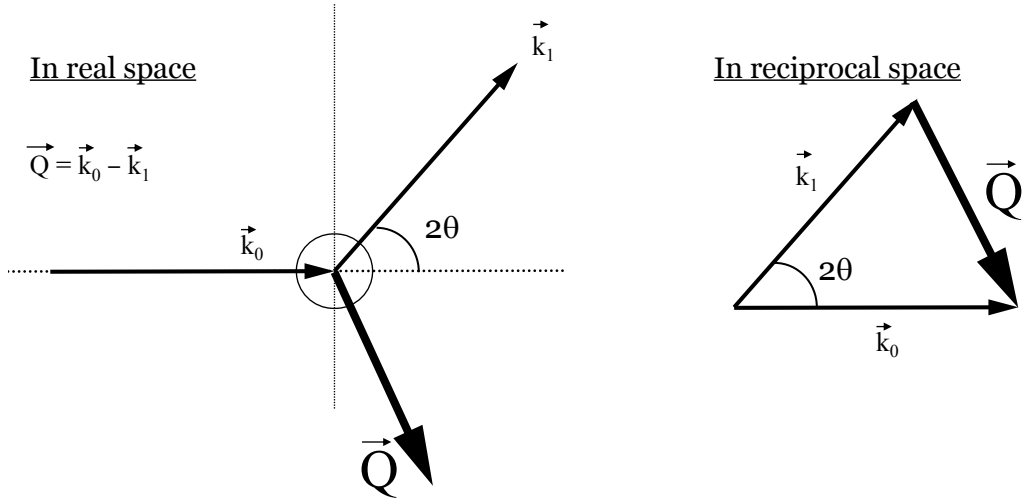


(a) (b)

Figure 3.1: Scattering geometry for single nucleus event in (a) real space and (b) reciprocal space.

In a scattering experiment the origin of the coordinates is at the position of the nucleus and the neutron is scattered to a position $\vec{r}$. The direction of the scattered beam is defined by the azimuthal angel $\phi$ and the angle $2\theta$ between incident and scattered beam. The scattering occurs in a cone of solid angle $\mathrm{d}\Omega$. This geometry can be seen in Figure 3.2 taken from Squires[106], page 5.

### 3.1.3 Scattering Cross-Sections

The measurement made in scattering experiments is the *neutron cross-section*, $\sigma$ of a system and is defined by its ability to scatter neutrons. There are three cross-sections which can be measured: total cross-section, $\sigma_{tot}$, differential cross-section (DCS), $\frac{\mathrm{d}\sigma}{\mathrm{d}\Omega}$, and double-differential cross-section (DDCS), $\frac{\mathrm{d}^2\sigma}{\mathrm{d}\Omega\,\mathrm{d}\omega}$.

The total cross-section, $\sigma_{tot}$, is the total number of scattering events in all directions every second per unit flux, thus the total probability of the scattering.

For purely elastic processes, like in diffraction experiments, where there is no transfer of energy to or from the sample, $\mathrm{d}\omega = 0$, we measure the DCS. Here, we simply evaluate the angular dependance of the incident flux $\Phi_0$ thus giving:

$$\frac{\mathrm{d}\sigma}{\mathrm{d}\Omega} = \frac{\text{no. of neutrons scattered per sec. in } \mathrm{d}\Omega}{\Phi_0\ \mathrm{d}\Omega} \tag{3.6}$$

For *inelastic* or *quasi-elastic* process where there is a transfer of energy between the

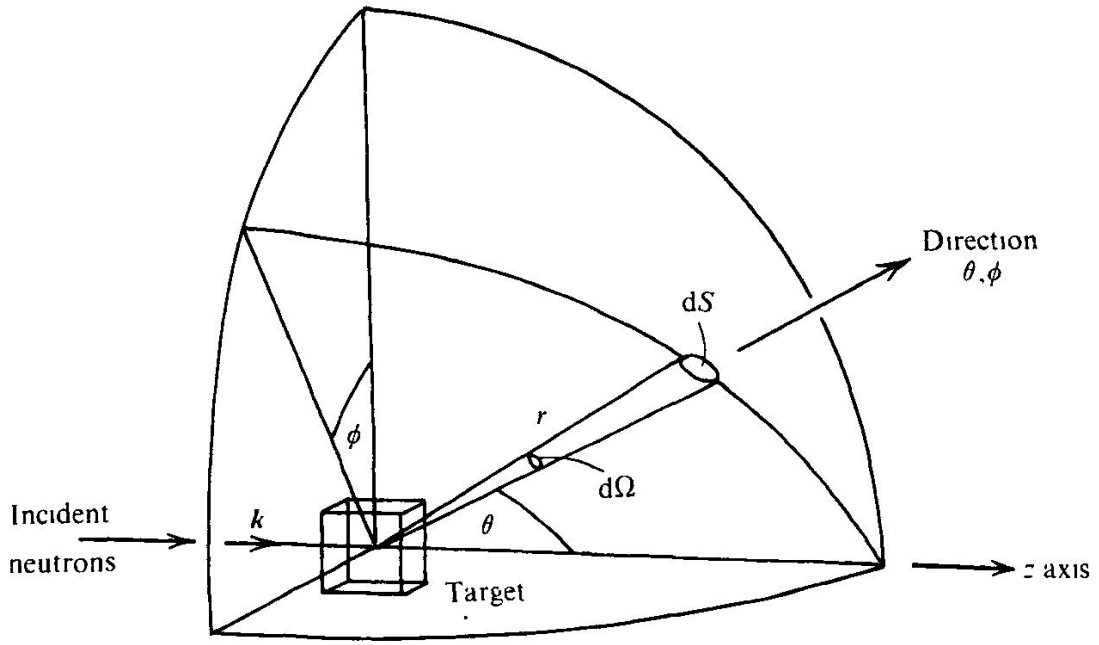


Figure 3.2: The geometry of a neutron scattering experiment[2].

neutrons and the sample, $\mathrm{d}\omega \neq 0$, we measure the DDCS:

$$\frac{\mathrm{d}^2\sigma}{\mathrm{d}\Omega\,\mathrm{d}\omega} = \frac{\text{no. of neutrons scattered per sec. in } \mathrm{d}\Omega \text{ with energies}[\omega;\omega_1 + \mathrm{d}\omega]}{\Phi_0\,\mathrm{d}\Omega\,\mathrm{d}\omega_1} \tag{3.7}$$

The cross-sections are then related by integration over the scattered energy, $\mathrm{d}\omega$:

$$\frac{\mathrm{d}\sigma}{\mathrm{d}\Omega} = \int_0^\infty \frac{\mathrm{d}^2\sigma}{\mathrm{d}\Omega\,\mathrm{d}\omega}\,\mathrm{d}\omega \tag{3.8}$$

$$\sigma_{tot} = \int \mathrm{d}\Omega \int \frac{\mathrm{d}^2\sigma}{\mathrm{d}\Omega\,\mathrm{d}\omega}\,\mathrm{d}\omega \tag{3.9}$$

However, a neutron scattering experiment physically measures the number of neutrons detected per second (intensity of the scattered beam), $I$, which can be expressed in terms of the **double-differential cross-section**:

$$\frac{\mathrm{d}^2\sigma}{\mathrm{d}\Omega\,\mathrm{d}\omega} = \frac{I}{\Phi(E_0)\,\mathrm{d}\omega\,\mathrm{d}\Omega} \tag{3.10}$$

Thus a direct relationship between the intensity of the scattered beam and the incident neutrons is made. Spectrometers measure the DDCS in the above way to obtain the combined elastic and inelastic scattering function, $S(\vec{Q},\omega)$. Diffractometers measure the

integral of the DDCS over all $\omega$ and at a given $2\theta$ to obtain the DCS which is proportional to the elastic scattering function, $S(\vec{Q})$. And finally the integral of the DCS over all $\Omega$ gives the total cross-section, proportional to N: the total number of scatterers present. Relations will be made in the following chapter between the DCS and $S(\vec{Q})$ and the DDCS and $S(\vec{Q},\omega)$.

### 3.1.4 Scattering from a single nucleus

Neutrons can scatter from the nuclei of atoms, either by the interaction via the strong nuclear force or via the interaction of the incident neutron spin and any net magnetic moment the scattering atom may possess. No magnetic studies are being undertaken thus magnetic interactions shall not be developed upon.
Let us first consider scattering from a single nucleus. The incident beam of neutrons traveling in the $x$-direction is a plane wave with wave vector $\vec{k}_0$ (as described previously) and wave function:

$$\psi_0 = \mathrm{e}^{ik_0x} \tag{3.11}$$

where $k_0$ is the magnitude of $\vec{k_0}$. The scattered wave vector is $\vec{k}_1$. The wavelengths of neutrons used in the following experiments are of the order of $10^{-10}$ m, far exceeding the range of nuclear forces and radii probed in these experiments which are of the order $10^{-14}$ – $10^{-15}$ m. The bound nucleus can therefore be considered as a point scatterer by the incident neutron beam and the scattering is isotropic $s$-wave scattering with wave function:

$$\psi_1 = -b\frac{\mathrm{e}^{ik_1r}}{r} \tag{3.12}$$

This scattering geometry is shown in Figure 3.3. $r$ is the distance of the scattered wave at position $\vec{r}$ from the fixed scattering nucleus placed at the origin ($\vec{r} = 0$). $b$ is the scattering length of the nucleus and is an experimentally determined parameter. It is related to the total cross section by:

$$\sigma_{tot} = 4\pi b^2 \tag{3.13}$$

$b$ describes the effective area of the nucleus viewed by the neutron and is called the *neutron*

*scattering length* of an atom species. The role of $b$ is described in more detail in section 3.1.6.

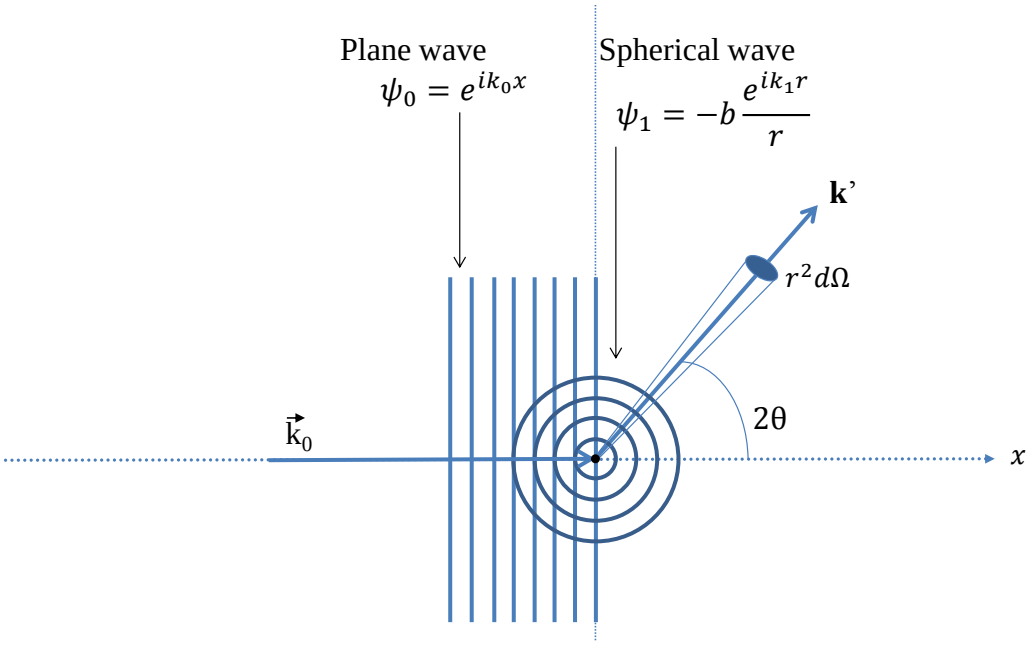


Figure 3.3: A scattering event from a single point scatterer by a plane to spherical wave.

### 3.1.5 Scattering from many atoms

We must now consider the nuclear scattering by a general system of particles, by evaluating an expression for the *double differential cross-section* $\frac{\mathrm{d}^2\sigma}{\mathrm{d}\Omega\,\mathrm{d}E_1}$ describing the transition of the system from one quantum state to another. We know that neutrons can scatter from the nucleus either via the strong nuclear force or via the interaction of the neutron spin with any magnetic moment that the scattering atom may possess. So first we ignore the magnetic interaction of the neutron and thus define its state solely on its momentum, i.e. wave-vector $\vec{k}$.

The differential cross section defined in eqn 3.8 represents the sum of all processes in which the state of the scattering system changes from $\lambda_0 \rightarrow \lambda_1$ and the state of the neutron changes from $\vec{k_0} \rightarrow \vec{k_1}$ and can be expressed as:

$$\left(\frac{\mathrm{d}\sigma}{\mathrm{d}\Omega}\right)_{\lambda_0 \rightarrow \lambda_1} = \frac{1}{\Phi}\frac{1}{\mathrm{d}\Omega}\sum_{\vec{k}_1 in\ \mathrm{d}\Omega} W_{\vec{k}_0,\lambda_0 \rightarrow \vec{k}_1,\lambda_1} \tag{3.14}$$

where $W_{\vec{k}_0,\lambda_0\to\vec{k}_1,\lambda_1}$ is the number of transitions per second from the initial state $\vec{k}_0, \lambda_0$ to the state $\vec{k}_1, \lambda_1$. The incident and scattered neutron has initial and final wave functions $\psi_0$ and $\psi_1$ respectively.

When the neutron enters the material it will experience a potential $V(\vec{r})$ at point $\vec{r}$ in the sample and the transition described in eqn 3.14 has transition probability given by Fermi's golden rule in quantum mechanics:

$$\sum_{\vec{k}_1 in\ \mathrm{d}\Omega} W_{0\to1} = \frac{2\pi}{\hbar}|\langle\vec{k}_1,\lambda_1|V(\vec{r})|\vec{k}_0,\lambda_0\rangle|^2\rho_{k_1}(E_1) \tag{3.15}$$

where $\rho_{k_1}(E_1)$ is the density of the final state or in other words the scattered neutrons that fall onto the detector opening with energy $E_1$. In order to evaluate equation 3.14 the method of *box normalisation* is adopted. This is a regime in which the neutron and scattering system are contained in a large box with sides of length $L$[106], allowing $\rho_{\vec{k_1}}$[106] to be written as:

$$\rho_{\vec{k_1}} = \left(\frac{L}{2\pi}\right)^3 \frac{mk_1}{\hbar^2}\,\mathrm{d}\Omega \tag{3.16}$$

The wave functions of the neutrons become:

$$\psi_{k_0} = \frac{1}{L^{\frac{3}{2}}}\mathrm{e}^{i\vec{k_0}\cdot\vec{r}} \tag{3.17a}$$

$$\psi_{k_1} = \frac{1}{L^{\frac{3}{2}}}\mathrm{e}^{i\vec{k_1}\cdot\vec{r}} \tag{3.17b}$$

The incident neutron flux is given by the product of the neutrons' density and velocity:

$$\Phi = \frac{1}{L^3}\frac{\hbar k}{m} \tag{3.18}$$

Given that $\vec{Q} = \vec{k_0} - \vec{k_1}$, using planar integral and substituting equations 3.15, 3.16, 3.18 into equation 3.14, obtains the following expression:

$$\left(\frac{\mathrm{d}\sigma}{\mathrm{d}\Omega}\right)_{\lambda_0\to\lambda_1} = \frac{k_1}{k_0}\left(\frac{m}{2\pi\hbar^2}\right)^2\left|\int \mathrm{e}^{i\vec{Q}\cdot\vec{r}}V(\vec{r})\,\mathrm{d}\vec{r}\right|^2 \tag{3.19}$$

The range of the scattering potential $V(\vec{r})$ is assumed to be short due to the relatively small size of the nucleus. Thus $V(\vec{r})$ can be expressed as a sum of Fermi pseudo potentials

directly related to the individual scattering centres at positions $\vec{R}_i$ in the material:

$$V(\vec{r}) = \frac{2\pi\hbar^2}{m} \sum_i b_j \delta(\vec{r} - \vec{R}_i) \tag{3.20}$$

where $b_j$ is the scattering length of the $j$th nucleus. If we combine equations 3.19 and 3.20 and since $\int F(x)\delta(x - x_i)\,\mathrm{d}x = F(x_i)$ equation 3.19 becomes:

$$\left(\frac{\mathrm{d}\sigma}{\mathrm{d}\Omega}\right)_{\lambda_0 \to \lambda_1} = \frac{k_1}{k_0} \left| \int b_j \mathrm{e}^{i\vec{Q}\cdot\vec{r_j}}\,\mathrm{d}\vec{r} \right|^2 \tag{3.21}$$

Equation 3.21 describes the scattering process that occurs when there is no change in energy between the initial and final state of the neutron and the system. i.e. the scattering is completely elastic.

We must now define the **double-differential cross-section**. If $E_0$ and $E_1$ are the initial and final energies of the neutron and $E_{\lambda_0}$ and $E_{\lambda_1}$ are the initial and final energies of the scattering system, then via conservation of energy:

$$E_0 + E_{\lambda_0} = E_1 + E_{\lambda_1} \tag{3.22}$$

Mathematically, the energy distribution of the scattered neutrons is a $\delta$-function, $\delta(E_{\lambda_0} - E_{\lambda_1} + E_0 - E_1)$ and therefore integrates to unity. Following from equation 3.8, the expression for the partial differential cross-section is now:

$$\left(\frac{\mathrm{d}^2\sigma}{\mathrm{d}\Omega\,\mathrm{d}E_1}\right)_{\lambda_0 \to \lambda_1} = \frac{k_1}{k_0} \left| \int b_j \mathrm{e}^{i\vec{Q}\cdot\vec{r_j}}\,\mathrm{d}\vec{r} \right|^2 \delta(E_{\lambda_0} - E_{\lambda_1} + E_0 - E_1) \tag{3.23}$$

By expressing the $\delta$-function for energy as in integral with respect to time as follows [106]:

$$\delta(E_{\lambda_0} - E_{\lambda_1} + E_0 - E_1) = \frac{1}{2\pi\hbar} \int_{-\infty}^{\infty} \mathrm{e}^{\frac{i(E_{\lambda_1} - E_{\lambda_0})t}{\hbar}} \mathrm{e}^{-i\omega t}\,\mathrm{d}t \tag{3.24}$$

where the energy change of the neutron is finite and written as:

$$\hbar\omega = E_0 - E_1 \tag{3.25}$$

$\omega$ ia positive for energy loss and negative for energy gain. Substituting equation 3.24 into equation 3.23, the resulting expression for the double-differential cross-section is writ-

ten as:

$$\left(\frac{\mathrm{d}^2\sigma(Q)}{\mathrm{d}\Omega\,\mathrm{d}\omega}\right) = \frac{k_1}{k_0}\frac{1}{2\pi\hbar}\sum_{jj'} b_j b_{j'} \int_{-\infty}^{\infty} \left\langle \mathrm{e}^{-i\vec{Q}\cdot\vec{r_{j'}}(0)} \mathrm{e}^{i\vec{Q}\cdot\vec{r_j}(t)} \right\rangle \mathrm{e}^{-i\omega t}\,\mathrm{d}t \tag{3.26}$$

This is for a system in which the scattering length $b$ varies from one nucleus to another, i.e a poly-atomic system. The angular brackets denote an average over all starting times for observations of the system, equivalent to averaging over all thermodynamic states of the system.

### 3.1.6 Coherent and Incoherent Scattering

The scattering length $b$ varies from one nucleus to another according to their nuclear spin state and are not correlated for neighbouring isotopes. For atoms $j$ and $j'$, we therefore let the value $b_j$ occur with relative frequency $f_j$ such that $\sum_j f_j = 1$. The average value of $b$ for the system is then:

$$\bar{b} = \sum_j f_j b_j \tag{3.27}$$

and the average value of $b^2$ is:

$$\bar{b^2} = \sum_j f_j b_j^2 \tag{3.28}$$

There are two cases to consider, $j = j'$ or $j \neq j'$, referred to as coherent and incoherent respectively. Equation 3.26 can then be rewritten as:

$$\begin{aligned}\left(\frac{\mathrm{d}^2\sigma(\vec{Q})}{\mathrm{d}\Omega\,\mathrm{d}E_1}\right) = {} & \frac{k_1}{k_0}\frac{1}{2\pi\hbar}(\bar{b})^2 \sum_{jj'} \int_{-\infty}^{\infty} \left\langle \mathrm{e}^{-i\vec{Q}\cdot\vec{r_{j'}}(0)} \mathrm{e}^{i\vec{Q}\cdot\vec{r_j}(t)} \right\rangle \mathrm{e}^{-i\omega t}\,\mathrm{d}t \\ & + \frac{k_1}{k_0}\frac{1}{2\pi\hbar}\left(\bar{b^2} - (\bar{b})^2\right) \sum_j \int_{-\infty}^{\infty} \left\langle \mathrm{e}^{-i\vec{Q}\cdot\vec{r_j}(0)} \mathrm{e}^{i\vec{Q}\cdot\vec{r_j}(t)} \right\rangle \mathrm{e}^{-i\omega t}\,\mathrm{d}t\end{aligned} \tag{3.29}$$

The double-differential cross section is thus split into two terms. The first term on the r.h.s, the **coherent scattering** tells us about the correlated motions of all the atoms e.g. phonons and magnons (inelastic coherent) or the sample's average structure (elastic coherent). The contribution to the coherent scattering of $j = j'$ is normally quite small as the total number of nuclei is very large. The second term is due to properties of individual

| Species | H | D | O | $N^{14}$ | C | Ti | Zr | Mg | Si | Al |
|---|---|---|---|---|---|---|---|---|---|---|
| $b$/fm | -3.74 | 6.67 | 5.81 | 9.37 | 6.64 | -3.44 | 7.16 | 5.38 | 4.15 | 3.45 |

Table 3.2: Neutron incoherent scattering lengths $b_{inc}$, for selected species[8]. Note H and D have radically different neutron scattering lengths.

atoms and their motions and is known as **incoherent scattering**. Thus, it provides information on diffusive motions of the atoms: rotation, molecular vibration, translation (inelastic incoherent). It also reveals the isotopic inhomogeneity of the sample as well as the geometry of any confinement effects on the diffusion mechanism (elastic incoherent). In general, due to the isotropy of incoherent scattering, it adds a structureless background to the coherent signal obtained in a diffraction experiment.

The neutron scattering lengths can then be defined in terms of whether they are incoherent/coherent:

$$b_{coh} = \bar{b} \tag{3.30a}$$

$$b_{inc} = \sqrt{\bar{b^2} - (\bar{b})^2} \tag{3.30b}$$

There is no correlation between the scattering lengths of the elements and their atomic number as is the case with X-rays. The neutron scattering lengths are determined experimentally and the vast difference in hydrogen and deuterium scattering lengths can be exploited to great effect. Table 3.2 shows the values for the coherent scattering lengths, $b_{coh}$ for some important elements. Some elements have a negative scattering amplitude which occurs with elements whose nuclei scatter 180° out of phase.

Hydrogen also has a very large incoherent neutron scattering length of 25.27 fm and therefore this must be accounted for during data reduction for diffraction measurements as described in section 4.3.

### 3.1.7 Correlation functions

It is useful to relate the cross-section for neutron scattering to thermal averages of operators belonging to the scattering system because these are the physical measurements made by the spectrometers and diffractometers in an experiment. These thermal averages are known as *correlation functions*.

- the *pair correlation funcion*, $G(\vec{r}, t)$: the probability of finding a nucleus at position

$(\vec{r}, t)$ given that there is another one at a position $(\vec{r}, t) = (0, 0)$ (coherent scattering)

- the *self correlation function*, $G_{self}(\vec{r}, t)$: the probability of finding a nucleus at $(\vec{r}, t)$ if the *same* nucleus was at $(\vec{r}, t) = (0, 0)$ (incoherent scattering)

Be defining $S(\vec{Q}, \omega)$ is the **dynamical structure factor**:

$$S(\vec{Q}, \omega) = \frac{1}{2\pi\hbar} \int \sum_{j,j'} \left\langle \mathrm{e}^{-i\vec{Q}\cdot(\vec{r_{j'}}(0) - \vec{r_j}(t))} \right\rangle \mathrm{e}^{-i\omega t} \, \mathrm{d}t \tag{3.31}$$

we can rewrite the DDCS from equation 3.29 in a more useful way:

$$\left( \frac{\mathrm{d}^2\sigma}{\mathrm{d}\Omega \, \mathrm{d}E_1} \right)_{coh} = \frac{k_1}{k_0} (\bar{b})^2 N S_{coh}(\vec{Q}, \omega) \tag{3.32}$$

$$\left( \frac{\mathrm{d}^2\sigma}{\mathrm{d}\Omega \, \mathrm{d}E_1} \right)_{inc} = \frac{k_1}{k_0} N \left( \bar{b^2} - (\bar{b})^2 \right) S_{inc}(\vec{Q}, \omega) \tag{3.33}$$

where N is the number of nuclei in the scattering system. $S(\vec{Q}, \omega)$ combines contributions from all atoms in the sample and is the measurement made in a scattering experiment. $S_{coh}(\vec{Q}, \omega)$ is the double Fourier Transform in both space and time of the pair correlation function $G(\vec{r}, t)$ and similarly, $S_{inc}(\vec{Q}, \omega)$ is the double Fourier Transform of the self-correlation function $G_{self}(\vec{r}, t)$:

$$S_{coh}(\vec{Q}, \omega) = \frac{1}{2\pi\hbar} \int \int G(\vec{r}, t) \mathrm{e}^{i(\vec{Q}\cdot\vec{r} - \omega t)} \, \mathrm{d}\vec{r} \, \mathrm{d}t \tag{3.34}$$

$$S_{inc}(\vec{Q}, \omega) = \frac{1}{2\pi\hbar} \int \int G_{self}(\vec{r}, t) \mathrm{e}^{i(\vec{Q}\cdot\vec{r} - \omega t)} \, \mathrm{d}\vec{r} \, \mathrm{d}t \tag{3.35}$$

We can see how the scattering functions are thus also the same probabilities as the correlation functions (pair/self) but expressed in the reciprocal space.

## 3.2 Neutron an X-ray Diffraction

### 3.2.1 Diffraction in Clays

Consider an array of point scatterers, arranged in planes a distance $d$ apart (Figure3.4). A neutron wave with wavevector $\vec{k_0}$ and wavelength $\lambda$ is incident at an angle $\theta$ to the planes. For total constructive interference, the path difference between the scattered wave

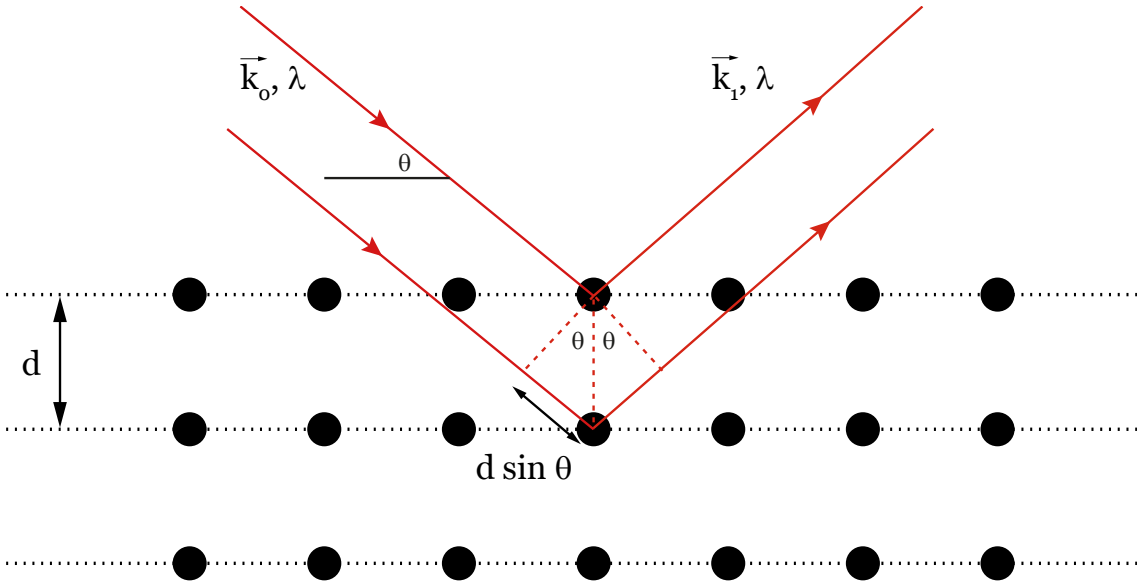


Figure 3.4: Geometry of scattering from two planes of atoms, a distance $d$ apart. The momentum transfer vector $\vec{Q}$ is perpendicular to the planes of atoms. For scattering from clays, each plane can be visualized as a clay layer.

$\vec{k_1}$ must be equal to an integral number of wavelengths. I.e. satisfying Bragg's law:

$$2d\sin(\theta) = n\lambda \tag{3.36}$$

Elastic coherent scattering only occurs at regular intervals in $\vec{Q}$ which correspond in real space to the distance $d$ separating the planes of atoms in real space. I.e.

$$|\vec{Q}| = \frac{4\pi\sin(\theta)}{\lambda} = \frac{2\pi n}{d} \tag{3.37}$$

Now consider a crystalline solid made up of an infinitely repeating pattern of atoms. The group of atoms which make up the repeating unit, or unit cell, of the material is called the basis. The real-space lattice unit vectors are $\vec{a}, \vec{b}$ and $\vec{c}$ which combine to make the real-space vector $\vec{R}$ through:

$$\vec{R} = u\vec{a} + v\vec{b} + w\vec{c} \tag{3.38}$$

where $u, v$ and $w$ are integers. Fourier analysis of this lattice requires that $\vec{R}\cdot\vec{G} = 2\pi n$ and results in its reciprocal with transformation vectors:

$$\vec{G}_{hkl} = h\vec{a}^* + k\vec{b}^* + l\vec{c}^* \tag{3.39}$$

For $\vec{R} \cdot \vec{G} = 2\pi n$ to hold true:

$$|\vec{G}| = n\frac{2\pi}{d_{hkl}} \tag{3.40}$$

where $n$ is any integer and $d_{hkl}$ is the distance between the planes denoted with the given $hkl$ values. The Laue condition is thus that, if the above holds true, we obtain the relationship between the scattering vector $\vec{Q}$ and the reciprocal lattice vector for elastic coherent scattering: $\vec{Q} = \vec{G}_{hkl}$.

These indices give the order with respect to the axis of the unit cell the scattering is occurring from. For example if we consider scattering from a particular Bragg plane with $l = 1, 2, 3, 4(00l)$ it would correspond to the reflections from the planes of atoms perpendicular to the $c$-axis of the unit cell. This direction is important here since the layers of the clay lie perpendicular to the $c$-axis, Figure3.4.

For neutron diffraction of these systems, if we sum the contributions of all the atoms $j$ of scattering length $b_j$ in the plane $hkl$ we get the structure factor which also predicts the position and intensity of the Bragg peak which is an evaluation of eqn.3.21:

$$\left| \sum_j (\bar{b_j})^2 \mathrm{e}^{(\vec{G}_{hkl} \cdot \vec{r_j})} \right|^2 = |S_{hkl}|^2 = I \tag{3.41}$$

In X-Ray scattering the $b_j$ is replaced with $f_j(Q)$ which is the *atomic form factor*.

### 3.2.2 Diffraction in Liquids

For a full description of neutron studies of liquids see Fischer *et al* [107].

Coherent neutron scattering gives information about the relative motions and positions of *different* particles in the liquid. Using the correlation function formalism, and make the 'static approximation': energy of incident neutron is much greater than the energy transferred between the interaction between the neutron and the nucleus. I.e. $\mathrm{E} \gg h\omega$ and $|k_0| = |k_1|$. If we consider the liquid with uniform density, $\rho = \frac{N}{V}$, we write the partial structure factor, $S_{\alpha\beta}(Q)$ containing the information about the correlation between atom of type $\alpha$ and of type $\beta$ in $Q$-space, as:

$$S_{\alpha\beta}(Q) - 1 = \frac{4\pi\rho_0}{Q} \int_0^\infty r[g_{\alpha\beta}(r) - 1] \sin(Qr)\, \mathrm{d}r \tag{3.42}$$

Since this equation only contains information about atoms $\alpha$ and $\beta$, the differential cross-section measured in the neutron scattering experiment containing $N$ atomic species, must be written as a weighted sum of all the individual structure factors arising from the correlations between the different pairs of atoms.

$$\left(\frac{\mathrm{d}\sigma}{\mathrm{d}\Omega}\right) = \sum_{\alpha=1}^{N} c_\alpha \bar{b_\alpha^2} + \sum_{\alpha=1}^{N}\sum_{\beta=1}^{N} c_\alpha c_\beta \bar{b}_\alpha \bar{b}_\beta [S_{\alpha\beta}(Q) - 1] \tag{3.43}$$

where $c_\alpha$ and $c_\beta$ are the atomic fractions of atoms $\alpha$ and $\beta$ respectively. The first term on the r.h.s. is the self-scattering term which the diffraction data is corrected for in the data reduction described in section 4.3. The second term is then defined as the *total structure factor*:

$$F(Q) = \sum_{\alpha}\sum_{\beta} c_\alpha c_\beta b_\alpha b_\beta [S_{\alpha\beta}(Q) - 1] \tag{3.44}$$

$F(Q)$ is the neutron weighted sum of all the individual partial structure factors and the final function extracted from raw diffraction data once the raw data has been corrected for self and incoherent scattering. As $F(Q)$ and $S(Q)$ are in $Q$-space (reciprocal space) we can inverse Fourier transform the individual $S_{\alpha\beta}(Q)$ to directly obtain real space information found in the individual pair distribution functions $g_{\alpha\beta}(r)$ which can be calculated via:

$$g_{\alpha\beta}(r) - 1 = \frac{1}{2\pi^2 r \rho_0} \int_0^\infty [S_{\alpha\beta}(Q) - 1] \sin(Qr)\, \mathrm{d}Q \tag{3.45}$$

Integrating the real-space pair distribution functions along $r$ calculates the average number of atoms (coordination number) of type $\beta$ surrounding atom type $\alpha$ between the distances $r_1$ and $r_2$ as follows:

$$\bar{n_\beta^\alpha} = 4\pi n_0 c_\beta \int_{r_1}^{r_2} r^2 g_{\alpha\beta}(r)\, \mathrm{d}r \tag{3.46}$$

where $n_0$ is the atomic number density of the sample (e.g. in units of atoms$\mathring{A}^{-3}$).

## 3.3 Small-Angle Neutron Scattering

A generalised expression for the small-angle scattering from any sample is

$$\left(\frac{\mathrm{d}\sigma(Q)}{\mathrm{d}\Omega}\right) = N_p V_p^2 \bar{\rho}_p^2 P(Q) S(Q) \tag{3.47}$$

where $N_p$ is the number of identical particles, each of volume $N_p$, in the sample. $P(Q)$ is the *shape factor* and $S(Q)$ is the *inter-particle structure factor* taken from equation 3.42. $\rho_p^{-2}$ is the *scattering length density* of the sample. Suppose we are scattering from a solution of molecules which have a tendency to cluster. The scattering process is governed by the interference between waves scattered by regions of minimum length $l = \frac{2\pi}{Q_{max}}$ of the instrument. The volume of these regions is called the resolution volume, $v$. The distance $l$ is large compared to interatomic distances but small compared to the linear size of the molecular clusters. The local scattering length density, $\rho(\mathbf{r})$ is obtained by summing the coherent scattering lengths of all atoms in the resolution volume $v$, centred on position $\mathbf{r}$, and dividing by the volume. Therefore $\rho(r)$ is given by:

$$\rho(r) = \frac{1}{v}\Sigma_i^n b_i(\mathbf{r}) \tag{3.48}$$

where $b_i(\mathbf{r})$ is the scattering length of the atom $i$ at position $\mathbf{r}$. $\rho(r)$ can be calculated for the solvent $\rho_S$ and also of the molecular cluster of volume V, $\rho_V$. Therefore the average scattering density of the solution (or the scattering length density) is given by:

$$\bar{\rho}_p = \rho_V - \rho_S \tag{3.49}$$

The shape factor term $P(Q)$ describes the influence of the shape of the scattering molecular clusters on the observed cross-section and emerges quite exactly depending on whether the scattered cluster is a sphere, ellipsoid, rod etc. A table of form factors can be found in *Willis & Carlile* p.181 [2]. The inter-particle structure factor $S(Q)$, accounts for the influence on the measured cross-section of local order between the scattering clusters. Here we can use the expression Eqn. 3.42 for a liquid by replacing the atoms by clusters:

$$S(Q) - 1 = \frac{4\pi N}{Q}\int_0^\infty r[g_p(r) - 1]\sin(Qr)\,\mathrm{d}r \tag{3.50}$$

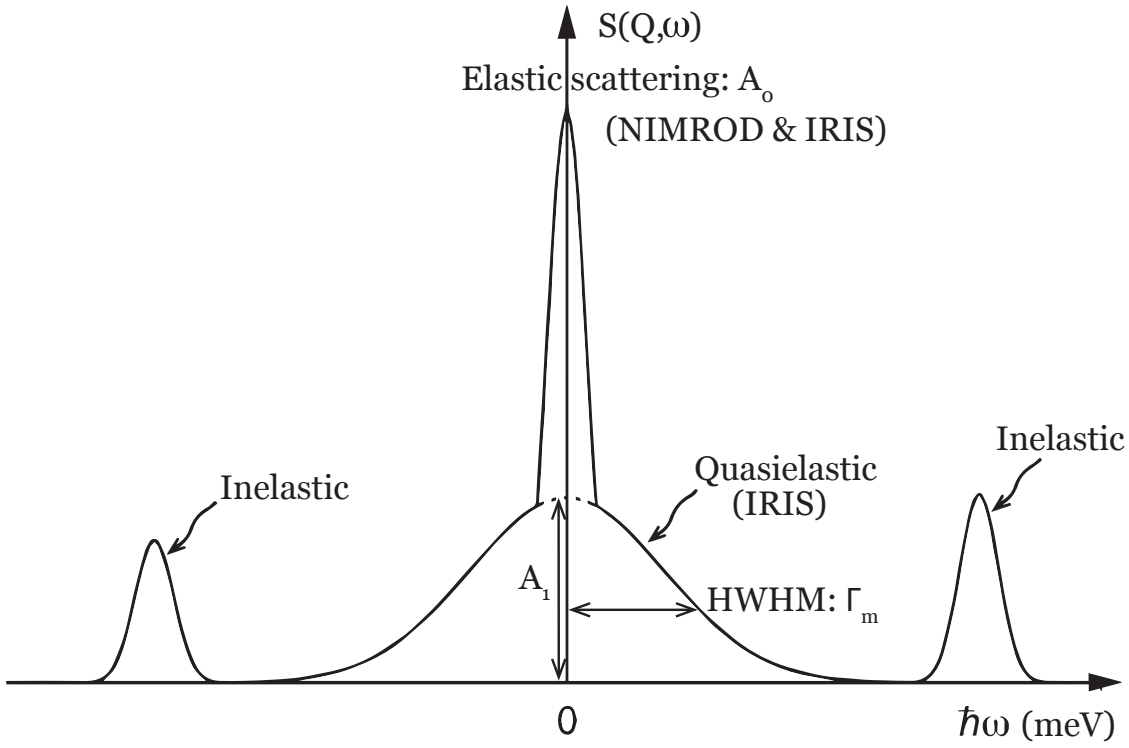


Figure 3.5: Schematic representation of an incoherent neutron scattering spectrum, displaying a single quasi-elastic component, centred at zero, broadening the base of the elastic line having amplitude $A_1$ and half width half-maximum (HWHM) $\Gamma_m$.

where $N$ is the number of clusters per unit volume and $g_p(r)$ is the pair distribution function representing the probability that a pair or clusters is a distance $r$ apart.

## 3.4 Neutron Spectroscopy

### 3.4.1 Quasi-elastic Neutron Scattering (QENS)

In a spectroscopy experiment, the measured quantity is the incoherent scattering function $S_{inc}(\vec{Q},\omega)$, Equation 3.35 gives the temporal and spatial correlations between pairs of atoms in the sample. In the quasi-elastic neutron scattering experiment described here, the intensity is dominated by incoherent scattering from the hydrogen atoms in the sample due to the size of the neutron cross-section. Table 3.3 gives some incoherent cross-section values. The term quasi-elastic describes those process which are *almost* elastic and do not occur as discrete inelastic peaks but as a Doppler broadening to the elastic line. Thus for the systems in the experiment here, the QENS describes the molecular diffusion through translation, rotational and vibrational shifts of hydrogen atoms in the sample. Figure 3.5 shows the region of interest to this study.

| Species | H | D | O | $N^{14}$ | C | Ti | Zr | Mg | Si | Al |
|---|---|---|---|---|---|---|---|---|---|---|
| $\sigma_{inc}$/barn | 80.26 | 2.05 | 0.0008 | 0.5 | 0.001 | 2.87 | 0.02 | 0.08 | 0.004 | 0.008 |

Table 3.3: Incoherent neutron cross-sections $\sigma_{inc}$, for selected species[9]. H has by far the biggest incoherent scattering cross-section, and therefore dominates the quasi-elastic neutron scattering from our systems.

The incoherent intermediate scattering function,$I_{inc}(\vec{(}Q),t)$, obtained by a temporal Fourier transform of the correlation function, correlates all the stochastic motions of a single particle. Both the rotational and translational modes of diffusion result in an exponentially decaying$I_{inc}(\vec{(}Q),t)$, the rate of decay being proportional to the relaxation time of the motion,$\tau$ .

**Self Diffusivites**

In the QENS experiments for this thesis, the incoherent scatterers are primarily the hydrogen in the water but also the hydrogen atoms on the aromatic ring of the terephthalate ion.

Due to the different time-scales of the three motions[108], they are assumed to be uncoupled and the scattering function can be written:

$$S_{inc}(\vec{Q},\omega) = \mathrm{e}^{-\langle u\rangle^2 Q^2}\left[A_0(\vec{Q})\delta(\omega) + \sum_{n=1}^{\inf} A_n^{rot}(\vec{Q})\frac{1}{\pi}\frac{(n(n+1)D_R)}{n(n+1)+\omega^2} + \sum_{n=1}^{\inf} A_m^{trans}(\vec{Q})\frac{1}{\pi}\frac{\Gamma_m(\vec{Q})}{\Gamma_m^2(\vec{Q})+\omega^2}\right] \tag{3.51}$$

where $D_R$ is the rotational diffusion coefficient. The exponential in the front is the Debye-Waller factor which describes the vibrational part i.e the attenuation due to thermal motion. The first term inside the square brackets is the elastic component, the second due to rotational motion and the last term is due to the translation diffusion, i.e. a Lorentzian. The quasi-elastic Lorentzian is seen as a broadening to the original elastic line, the width of which,$\Gamma_m$, depends on the precise *dynamics* of the scatterer.

The elastic component, $\delta(\omega)$, has a $Q$-dependent intensity given by the elastic incoherent structure factor (EISF):

$$EISF = A_0(\vec{Q}) = \lim_{l\to\infty}[I_{inc}(\vec{Q},t)] = \frac{I_{el}}{(I_{el}+I_{ql})} \tag{3.52}$$

where $I_{el}$ is the elastic intensity and $I_{ql}$, the quasi-elastic intensity. It is the intensity attributed to the elastic collisions with scatters and is related to the *static* geometry of the scattering process[109]. The behaviour of the EISF as a function of $Q$ is indicative of the diffusion mechanism i.e. is it continuous, jump, rotational, and also the proportion of rotation to translational motion. When motion is purely translational, the EISF is zero for all $Q > 0$. If diffusion of the hydrogen scatterers is purely rotational, then the EISF is constant with $Q$ indicating that they are localised. If both motions are present, then the EISF falls to a minimum at some specific $Q$-value.

**Jump diffusion**

For times which are long compared to the mean time between atomic collisions, translation is governed by the Brownian diffusion process, and the HWHM of the QE Lorentzian function, has a Fickian form:

$$\Gamma_m(Q) = \hbar \cdot D_{trans} \cdot Q^2 \tag{3.53}$$

However for diffusion at atomistic scales, it is no longer applicable since the diffusion is *restricted* due to confinement, strong interactions, bonding restrictions or diffusion happening in jumps. At very low $Q$, we lose the details of the jump mechanism so the diffusion can be described by Fick's law, Equation 3.53. Otherwise we use one of the several analytical models describing the jump mechanism which are discussed below. They involve fitting of the HWHM describing the translational part of the incoherent scattering function in this restricted regime.

The diffusion models developed by Hall and Ross[110] and Singwi and Sjölander[111], assume that a water molecule oscillates with a particular mean square amplitude $\langle u^2 \rangle$ around an equilibrium position and for an average time ( $\tau$ ), before it jumps a distance $l$ to another equilibrium position, where $l^2 >> \langle u^2 \rangle$.

The Gaussian jump-length distribution model of **Hall and Ross(HR)**[110] gives the broadening of the HWHM as :

$$\Gamma_t(Q) = \frac{\hbar}{\tau_t}\left[1 - \mathrm{e}^{(-Q^2 D_t \tau_t)}\right] \tag{3.54}$$

with mean square of the jump length $l$ in the form: $l^2 = \int_0^\infty r^2 p(r) dr = 3r_0^2$ ; and the

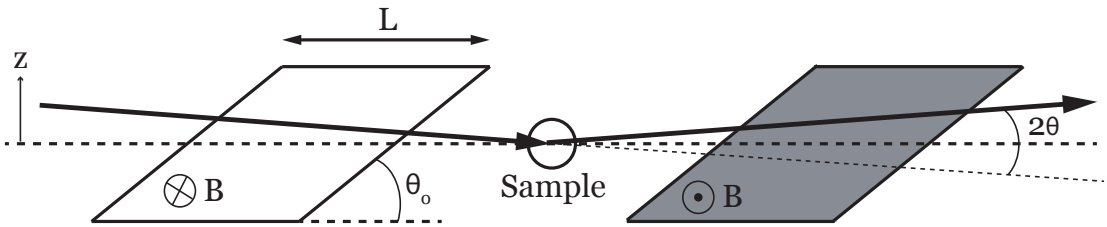


Figure 3.6: Angle labelling using Larmor precession. The external magnetic field $B$, with inclined entrance and exit faces, is applied for a length $L$ before the sample. An equal but opposite field is applied to the beam after the sample so that neutrons that do not scatter from the sample can be eliminated. Scattered neutrons experience different amounts of depolarisation depending on the angle $2\theta$ through which they are scattered.

diffusion coefficient, $D_{trans} = \frac{l^2}{6\tau_t}$. $p(r)$ is the probability of finding the diffusing molecule at a particular jump site position $r$ after jumping. $r_0$ is the position of the site occupied by the diffusing species before jumping. $\tau_t$ is the residence time of the water molecule at a specific position before it rapidly jumps to the next position.

The exponential distribution of jump-lengths of **Singwi and Sjölander (SS)**[111] defines the broadening of the HWHM as:

$$\Gamma_t(Q) = \frac{\hbar \cdot D_t \cdot Q}{1 + D_t \cdot Q^2 \tau_t} \tag{3.55}$$

and the mean square jump length $l^2 = 6r_0^2$.

The **Chudley and Elliot model (CE)**[112] has a constant jump distance $l$ and the HWHM of the QE Lorentzian broadening has the the form:

$$\Gamma_t(Q) = \frac{\hbar}{\tau}(1 - sinc(Q \cdot l)) \tag{3.56}$$

$D_t$ can then be calculated from the parameters observed from fitting the CE equation.

## 3.5 Spin-Echo Small Angle Neutron Scattering: OffSpec

To obtain extremely broad spatial and high energy resolution, the spin-echo technique can be exploited since it eliminates the need to prepare an incoming beam with a wavelength distribution as narrow as the required resolution. Instead the neutron spin wavefunction with an external magnetic field is utilised. For a full mathematical description of the spin-echo technique for small angle scattering, see Mezei[113] and Rekveldt[114].

The principle in the spin-echo case is that a beam of incoming polarised neutrons are

made to Larmor precess according to the externally applied magnetic field $B$. The Larmor precession or 'spin-echo length, $r$', corresponds to the size of the objects that are scattered from and shown diagrammatically in Figure 3.6. It can be tuned using the above setup by changing any of $\lambda$, $B$, $L$ or $\theta_0$ through the following relationship:

$$r = \frac{c\lambda^2 BL \cot\theta_0}{2\pi} \tag{3.57}$$

where $\lambda$ is the wavelength of the incoming polarised neutron beam and $L$ and $\theta_0$ are the length and angles of the $B$-field.

After scattering at the sample, the beam travels through a symmetric setup but with opposite $B$-field which 'cancels out' the original precession. The neutrons which are not scattered by the sample hit the detector with the same polarisation that was applied to the incoming beam and the scattered neutrons will have depolarised according to the angle $2\theta$ that they make when exiting the sample. The polarisation of the beam which hits the detectors is therefore a weighted sum of the polarisation vectors of the scattered and non-scattered neutrons. By ensuring that the initial beam is polarized along the $z$-axis, that all scattered neutrons land in the detector and looking at the neutrons that only scatter with small angles, the measured beam $P_{sample}$ is related to a form of the one-dimensional real-space autocorrelation function $G(r)$ through:

$$\frac{P_{sample}}{P_{emptybeam}} = \mathrm{e}^{\sigma t(G(r)-1)} \tag{3.58}$$

$\sigma$ and $t$ are the attenuation coefficient and thickness of the sample respectively. OffSpec is the low background, polarised, reflectometer optimised for the measurement of off-specular reflection used for the SE-SANS investigation in the following experiment (Sec. 5.3). At its upper limit OffSpec allows the angle $\theta_0$ to be varied continuously from 50° to 90° over the length of the $B$-field thus allowing simultaneous observations of scattering objects from 10 nm to 30 $\mu m$ in diameter.

# Chapter 4

# Aqueous Structure of Hydrophobic Amines using Neutron Diffraction

This chapter presents the *in situ* neutron scattering experiments designed to investigate the structure of the quaternary ammonium salt tetramethylammonium chloride as a 1 molar solution in $D_2O$ subjected to elevated pressures and temperatures. Previous experimental work on aqueous TMA has focused on ambient pressure and temperature conditions[115] and with higher concentrations[116], the effect of which is seen as the intersolvent structure to represent that of bulk at lower temperatures. The new science described in this chapter is the behaviour and structures of hydrophobic salt solutions at elevated pressure and temperature conditions where we find the TMA ion acts to maintain bulk like intersolvent structure at the same p & T conditions. We also observe the formation of solvent separated TMA - Cl ion pairs which persist throughout the application of pressure and temperature. Pre-established geological gradients have been followed, Table 4.1, under controlled conditions for this investigation.

Also presented is a preliminary investigation into the effect of 2 molar hexamethylenediamine (HMDA) in $D_2O$ on the water-water structure. At this concentration, we observe an 'ice-like' intersolvent structure i.e. highly intense water-water structure however slightly lower density which is seen with other hydrophobic molecules[116].

## 4.1 Neutrons at Large-Scale Facilities

**Production: Spallation**

The neutrons at ISIS are produced via spallation, a process where pulsed beams of high energy protons are bombarded into a heavy metal (tantalum) target[2]. Figure 4.1 shows the components of the ISIS pulsed neutron source.

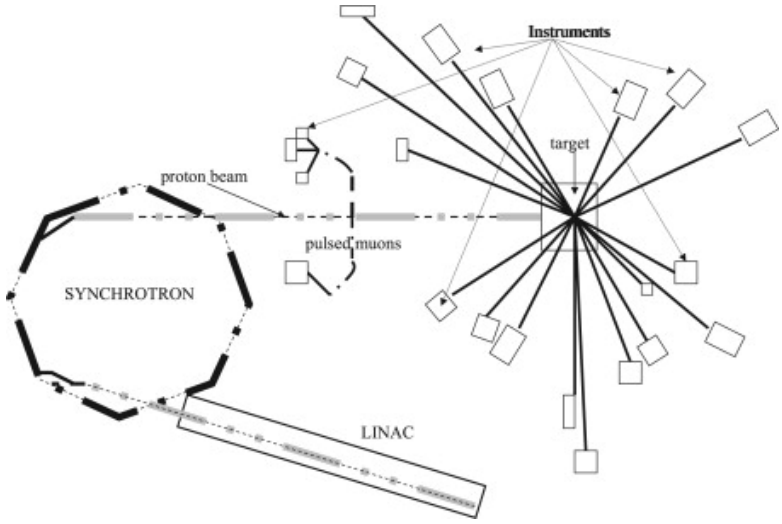


Figure 4.1: Neutron production at the ISIS facility taken from Pietropaolo[3].

Protons start out as $H^-$ ions formed from the ionisation of hydrogen gas and are accelerated by a linear accelerator to 70 MeV. The $H^-$ beam is injected into the synchrotron and is passed through thick aluminium oxide foil to strip the H- of its electrons resulting in a beam of protons. The protons are accelerated to 800 MeV and into 2 bunches via an increasing harmonic radio frequency before being extracted from the synchrotron to the tantalum target either in target station 1 or 2. This knocks out neutrons from the metal target with high energies therefore moderators are used to slow them down to useable speeds. The neutrons are then collimated to produce short pulses of neutrons with a range of energies.

It must be noted that fission sources are also available for the production of neutrons. Fission of the uranium isotope 235 by slow neutron capture releases more neutrons per fission process than are required to initiate the process. The spectral distribution of the

fissioned neutrons is described by a Maxwellian:

$$n(E) = 2\sqrt{\frac{E}{\pi E_T^3}}.e^{\frac{-E}{E_T}} \tag{4.1}$$

with a characteristic energy $E_T = 1.2MeV$. Importantly, fission reactors produce a continuous flux of neutrons unlike spallation sources.

## 4.2 Diffraction on the NIMROD Instrument

The Near and InterMediate Range Order Diffractometer (NIMROD)[4] makes use of the broad spectral range of the second target station, $0.04 < \lambda < 12$ $\mathring{A}$ at ISIS for the investigation of structural studies of disordered materials and liquids allowing continuous resolution from <1 to >300 $\mathring{A}$. It also uses the enhanced long wavelength flux to access low-Q and therefore long range order in these systems. The forward scattering geometry of the instrument minimises inelastic scattering effects[117] and is therefore ideal for the performance of hydrogen-deuterium isotopic substitution experiments.

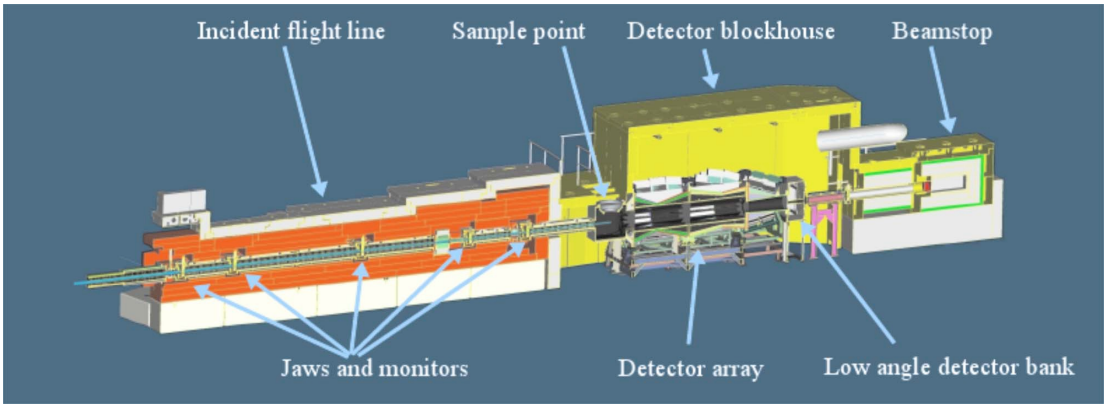


Figure 4.2: Schematic of the NIMROD instrument and beam propagation taken from the review of the NIMROD instrument.[4]

The wider angle array is comprised of 1098 zinc sulphide based scintillating elements, covering scattering angles from 3.5 to 40. The low angle detector bank covers scattering angles from 0.5 to 2.2 in a dartboard style and is comprised from 756 detector elements. These detector banks combined, correspond to a Q-range of 0.02 - 100$\mathring{A}^{-1}$.

| Depth (km) | Temperature (K) | Pressure (bar) | Density (atoms/Å$^3$) |
|---|---|---|---|
| 0 | 22 | 50 | 0.1003 |
| - | 22 | 600 | 0.1019 |
| 2 | 80 | 600 | 0.0999 |
| 4 | 140 | 600 | 0.0961 |

Table 4.1: Pressure and temperature gradients.

**NIMROD Sample Environment**

The sample environment used for this experiment was designed and built through a joint effort between UCL and RAL for the Ph.D project of Dr. A. De Siqueira to simulate the conditions that would be encountered in a well bore. The pressure cell environment had a maximum temperature and pressure of 670 K and 1.7 kbar respectively. These upper limits were sufficient to maintain the pressures and temperatures required for this investigation. Table 4.1 relates burial depth to the these pressures, temperatures and densities of the 1 Molar TMACl-$D_2O$ solution at the corresponding p/T. An extra data point was added at 295 K and 600 bar to isolate the effect of pressure on the system. The number densities for the solutions were calculated using the analytic equation of state for water[118] and incorporating by volume, the density of TMACl in its solid state.

The sample cell was made from titanium-zirconium (TiZr) alloy as described previously so that the alloy became a null scatterer with a flat-plate geometry and wall thickness of 10 mm. This surrounded a 15 mm by 4 mm sample slot which was 50 mm deep. Although the wall thickness or large volume of sample (and therefore distance of the beam travelled within the sample) was not optimal for neutron measurements, it was required for containing the pressures and temperatures used in the experiment. Two belt heaters wrapped around the top and bottom parts of the cell to control the temperature of the sample which was monitored by two Fe thermocouples: one thermocouple measuring the applied heat and the other measuring the sample temperature. The sample can was sealed using a silver hollow o-ring. When the cap of the cell was tightened and hydrostatic pressure applied, the hollow seal collapsed to fill the available space. Each o-ring could therefore only be used once. Figure4.3 shows the high pressure environment and sample can used for the experiment.

Pressure is applied hydro-statically with $D_2O$ via a high-pressure hand pump directly onto the sample. The pump oil is separated from the $D_2O$ by steel pressure bellows and

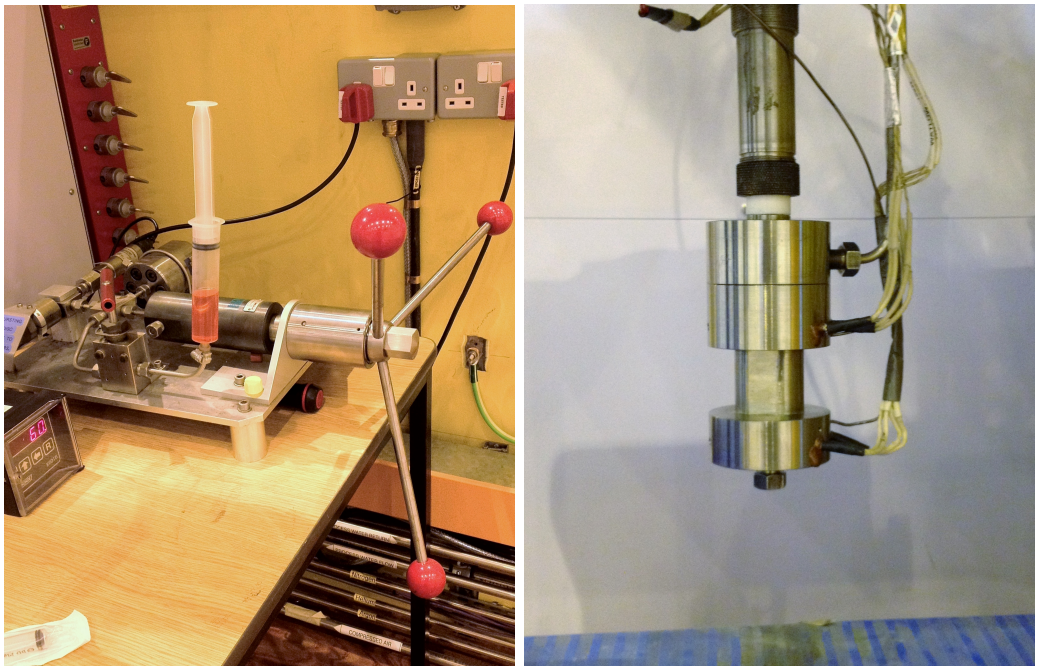

(a) (b)

Figure 4.3: High pressure sample environment allowing hydrostatic pressure exertion of 1.7 kbar and a maximum temperature threshold of 670 K.
**Fig 4.3(a):** High p/T rig.
**Fig 4.3(b):** TiZr null scattering sample can.

the digital gauges measure the applied pressure and the pressure in the sample can.

Most of the technical difficulties were to do with maintaining pressure in the sample can due to failure of the hollow seal. This was due to the expansion of the steel bolts holding the cap of the sample can, however when they were changed to high tensile steel bolts, there was no leaking of pressure indicating that the seal had been maintained.

## 4.3 Data Analysis Procedure for Liquid Diffraction Data

The data obtained from the NIMROD instrument was analysed using two programmes: Gudrun and Empirical Potential Structure Refinement (EPSR).

### Gudrun

Gudrun is a program that analyses diffraction data, be it neutron or X-ray data, from the raw neutron counts to a final differential cross section. It can do this detector by detector, combine the detectors into groups and will also perform the Fourier transform on the differential cross sections to yield real-space information. This step , the routines

used and the theory behind are explained in more detail than given here in the Gudrun manual[119]. To obtain fully corrected $F(Q)$ the following scattering measurements are required:

1. Empty container (sample background)
2. Sample + container
3. Vanadium slab
4. Empty instrument (vanadium background)

The steps in the data reduction are then as follows:

- **Purge bad detectors**

  NIMROD has 1098 detectors, not all of which will be stable for a given experiment. The program 'run purge' outputs a list of unusable detectors which must not be used in the analysis. This is based on the ratio of the number of counts with the sample present and the vanadium. In this work, if there is more than 10% variation in the spectra for an individual detector in a series of runs, the detector is discarded from the analysis.

- **Sample background**

  This is a measure of the naked beam i.e. with nothing in the scattering position.

- **Sample container**

  A measurement must be made with an empty container in the scattering position. (For experiments which involve variations in temperature and pressure, ideally measurements of the empty sample can must also be taken at those specific temperatures and pressure combinations.) Conveniently, for this experiment, the sample can is the null scattering TiZr alloy.

- **Normalisation to the incident spectrum**

  Several files are input into Gudrun containing information on detector dead-time and detector calibration which are used in the data correction. The data is normalised to incoherent scattering via a vanadium measurement. Vanadium is used since the scattering from the element is almost completely incoherent. Normalisation is required to allow for variations in wavelength flux which may arise within the detector.

- **Attenuation and multiple scattering corrections**

  This step removes scattering due to hydrogen in the sample. Hydrogen has a large neutron cross-section and therefore, depending on the sample thickness, will undergo multiple scattering. This will give incorrect detection times which need to be accurate in order to perform T-o-F measurements. Multiple scattering is corrected for by calculating a wavelength dependent absorption cross-section for all the samples and then subtracting them from the data. These are obtained by using the ratio of the transmission data from the sample and background.

Data reduction via Gudrun produces a normalised F(Q) which can then be fit using Empirical Potential Structure Refinement.

#### Empirical Potential Structure Refinement Analysis

Measured diffraction data on disordered materials reveals limited information about the system. The empirical potential structure refinement technique aims to maximise the information that can be extracted from this data[120,121]. EPSR produces a model with a simulated differential scattering cross section ($D_i(Q)$), which fits the experiment results as closely as possible. It also allows us to build 3-dimensional atomistic models of our system which are consistent with the measured diffraction data by using the experimentally observed data as a constraint against which the molecular simulation of the system is refined. The method starts with an equilibrated Monte Carlo representation of the system based on initial seed potentials. Using information already known about the system, such as the electrostatic charges, the Lennard-Jones description of the interatomic potentials and molecular geometry, the simulation iteratively lowers the energy of the system against these potentials. The measured data is then added as another parameter or *empirical potential* to constrain the system. It refines these potentials until the molecular simulation reproduces the experimental diffraction data. Thus, the measured 1-D data (in $r$) is extended into an atomistic box allowing for correlations in 3-D to be extracted. Specific to this work, EPSR allows for a 3-dimensional structural analysis of the environment around the $TMA^+$ to be performed as a function of pressure and temperature.

The molecular distributions resulting from the EPSR simulation are visualised using spherical harmonic expansion for molecular pair correlation functions[120,122]. The spherical harmonic representation is useful because it allows for the system to be perturbed at any time and in various ways without having to recalculate the atom positions each time. This

is done by fixing a chosen molecule and at the origin $(\phi_l, \theta_l)$ of the laboratory coordinates and then using Euler angles to describe a second molecule $(\phi_m \theta_m \chi_m)$. The spherical harmonics coefficients are calculated every 5 iterations and averaged every ∼1000 iterations. These are then used to calculate 3-dimensional spatial density plots around each molecule of interest by defining a set of co-ordinate axes relative to that molecule allowing for the investigation of relative orientations between molecules as a function of their separation. The EPSR analysis was checked by following the changes in: (*i*) Running EPSR without refinement, i.e. just a Monte Carlo simulation, (*ii*) monitoring the internal energy and pressure of the system (*iii*) checking for unphysical distance in the individual pair distribution functions $g_{\alpha\beta}(r)$. This allows us to make a comparison between the refined data and the seeds, thus ascertaining how the refinement has changed the structure of the system.

### 4.3.1 Sample Preparation

| Sample No. | Mass H12-TMA | Mass D12-TMA (g) | Mass $D_2O$ (g) | Molarity (M) |
|---|---|---|---|---|
| 1 | 11.1668 | - | 119.14 | 1.00051 |
| 2 | - | 4.2757 | 38.8835 | 1.00028 |
| 3 | 0.8222 | 0.9130 | 8.3025 | 1.00060 |

Table 4.2: Masses and molarity for each of the isotopically substituted samples: fully H, fully D and H:D 50:50 of the TMA ion.

The experimental work being reported here is focused on studying the structure of 1 Molar tetramethylammonium chloride (TMACl) in $D_2O$ solution. Three samples were prepared: 1M protiated TMACl $(C\mathbf{H}_3)_4N^+Cl^-$, 1M deuterated TMACl$(C\mathbf{D}_3)_4N^+Cl^-$ and a 50:50 mix of protiated to deuterated TMACl$(C\mathbf{H}_3/C\mathbf{D})_{2:2}N^+Cl^-$. These were prepared on site when each sample was required. Table 4.2 shows the masses and molarity of the samples.

## 4.4 Results: Structure 1M $TMACl_{(aq)}$ Under Burial Conditions

A single diffraction measurement on tetramethylammonium chloride dissolved in $D_2O$, after correction yields a total structure factor, F(Q). This is a weighted sum of twenty-

one different partial structure factors arising from the twenty-one partial pair correlation functions due to the six distinct atom species in the system: N, C, $H_{methyl}$, $O_{water}$, $H_{water}$, Cl. The technique of Empirical Potential Structural Refinement (EPSR) analysis fits the total structure factor, allows for a complete extraction of the individual pair distributions functions and also permits 3-dimensional analysis of the system.

Importantly, access to the low $Q$-region was possible to look for evidence of $TMA^+$–$TMA^+$ or $TMA^+$–$Cl^-$ aggregation, also known as 'salting out' due to the hydrophobic nature of the $TMA^+$ [123,124].

The three isotopically distinct samples were measured at four different p/T combinations given in Table 4.1. For a complete data set, it would have been desirable to take measurements on samples made with mixtures of $H_2O$ and $D_2O$ to remove the solvent scattering altogether. However, due to the large volume of sample required to fill the sample can, the solvent used was only $D_2O$. Any protiated water would lead to large amounts of inelastic scattering which would be almost impossible to correct for.

Data was also collected on pure $D_2O$ at the same pressures and temperatures as used for the $TMA_{(aq)}$ so that a comparison in the inter-solvent structure could be made.

### 4.4.1 Aims

In considering the structural implications of the results, the following points will be addressed:

- In what way if at all does the $TMA^+$ order the water molecules in the hydration region?
- Is there any evidence for ion pairing between the $TMA^+$ and $Cl^-$ or for $TMA^+$-$TMA^+$ hydrophobic clustering?
- Do the observations indicate any hydration changes with an increase in pressure and temperature?

### 4.4.2 Simulation Details

EPSR simulations were carried out on each of the four sets of diffraction data (obtained at each combination of temperature and pressure). The simulation box was a cubic box of side ∼38.0Å containing 1650 $D_2O$ molecules, 30 $TMA^+$ cations and 30 $Cl^-$ ions. The

| **Atom Type** | $\sigma$ (Å) | $\epsilon$ (kcal mol$^{-1}$) | **Charge, q** (e) |
|---|---|---|---|
| **C** | 3.7 | 0.8 | −0.18746 |
| **N** | 3.2 | 0.7 | +0.03021 |
| $\mathbf{H}_{methyl}$ | 0 | 0 | +0.1433 |
| $\mathbf{Cl}^-$ | 4.191 | 0.566 | −1 |
| $\mathbf{O}_{water}$ | 3.1 | 0.65 | −0.8476 |
| $\mathbf{H}_{water}$ | 0 | 0 | +0.4238 |

Table 4.3: Potentials used in EPSR analysis of form:
$V_{ij}(r_{ij}) = \frac{q_i q_j}{r_{ij}} + 4\epsilon_{\alpha\beta}\left[\left(\frac{\sigma_{\alpha\beta}}{r_{ij}}\right)^{12} - \left(\frac{\sigma_{\alpha\beta}}{r_{ij}}\right)^{6}\right]$

initial seed potentials are classical Lennard-Jones pairwise potentials, the parameters of which are in Table 4.3 and taken from empirical potential structure refinement carried out by Soper and Weckstrom[125] for $Cl^-$. MOPAC[126] is run on the ions and charges are distributed according to the solution of the AM1 Hamiltonian. SPC/E parameters taken from Berendsen *et al*[127] are used for the D and O in $D_2O$ molecules. Since the pressures and temperatures applied maintained the solvent $D_2O$ in a liquid state, these descriptions of the molecules were taken to be valid.

A representation of the system is shown in a snapshot of the EPSR ensemble in Figure 4.4. This is not a time averaged image however highlights the system under question.

### 4.4.3 Total Structure Factor

Typical fits of the EPSR ensemble ($D_i(Q)$, green lines) to the total structure factors (F(Q), black circles) derived from Gudrun for the three samples at 25°C 50 bar and 140°C 600 bar, the lowest and highest p/T combinations respectively, are shown in Figure 4.5. The full $Q$-range of the data is from 0.02 Å$^{-1}$ to 30 Å$^{-1}$ however only 0.02 Å$^{-1}$ $\leq Q \leq$ 12 Å$^{-1}$ has been plotted in order to see salient features more clearly.

The EPSR fits are exceptionally good at representing the data but there very subtle differences found at very low-$Q$ in the fully hydrogenated (H12-$TMA^+$) sample in particular and can be explained by an imperfect removal of inelastic scattering[124,128]. Otherwise, all other features are very well reproduced. Care must be taken to ensure that the model resulting from the EPSR analysis is realistic alongside the interpretations that are made. Therefore, the chi-square, internal energy and pressure of the system were monitored throughout the analysis to ensure that their values were reasonable. Coupled with this, the individual $g(r)$s and bond lengths of the $TMA^+$ ion were also monitored for any nonphysical short distances.

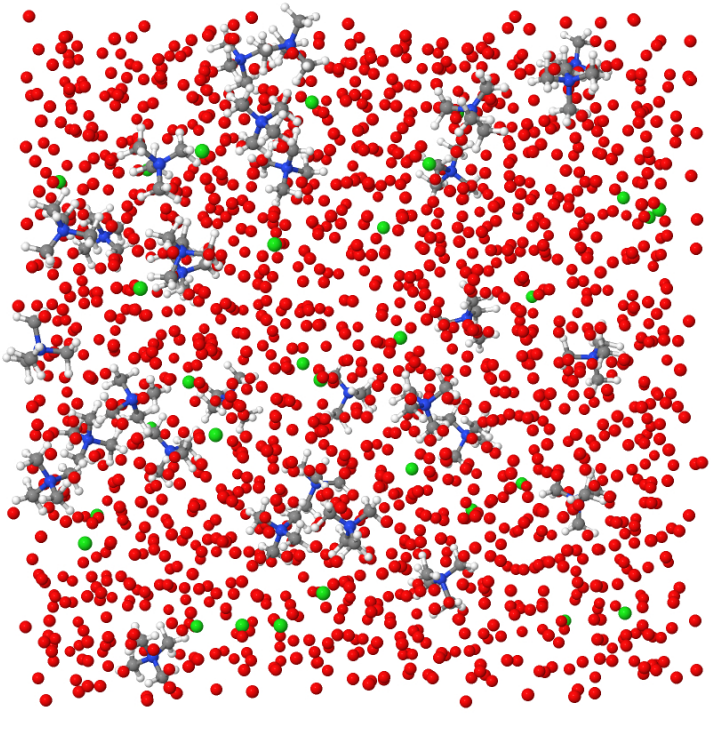


Figure 4.4: Snapshot of ensemble box taken when the EPSR has completed fitting the diffraction data for the measurement at 25°C 50 bar. Key: Nitrogen-blue, Carbon-Grey, Oxygen-red, Chloride-green. Hydrogen atoms on water molecules have not been displayed for clarity.

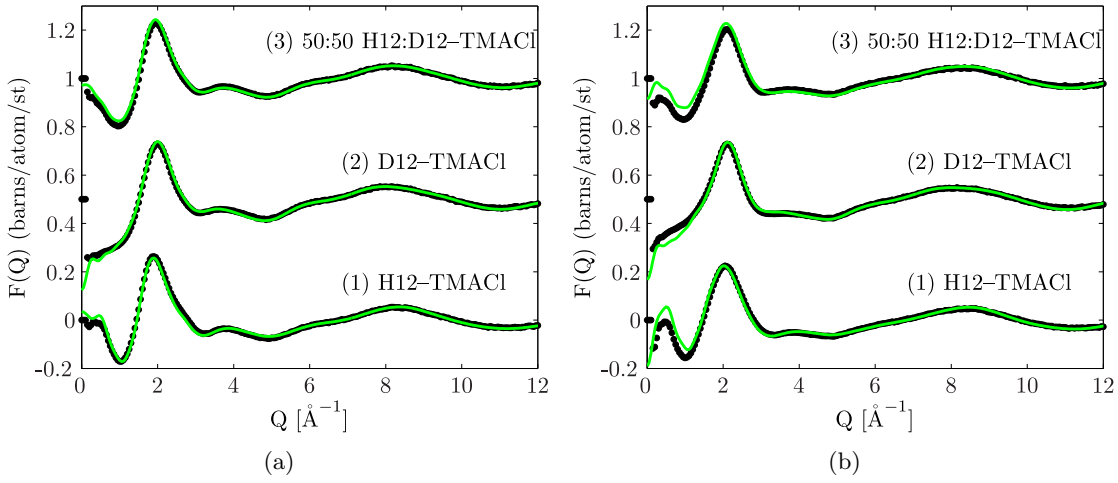


Figure 4.5: The total normalised structure factors F(Q) (black) with extremely good EPSR fits $D_i(Q)$ (green) at **(a)** 25°C 50 bar and **(b)** 140°C 600 bar, (highest and lowest p & T combination) for each of the three solutions, (1) $[N(CH_3)_4]^+Cl^-$ in $D_2O$, (2) $[N(CD_3)_4]^+Cl^-$ in $D_2O$, (3) $[N(CH_3{:}\ CD_3)_4]^+Cl^-$ in $D_2O$. The results have been shifted vertically for clarity.

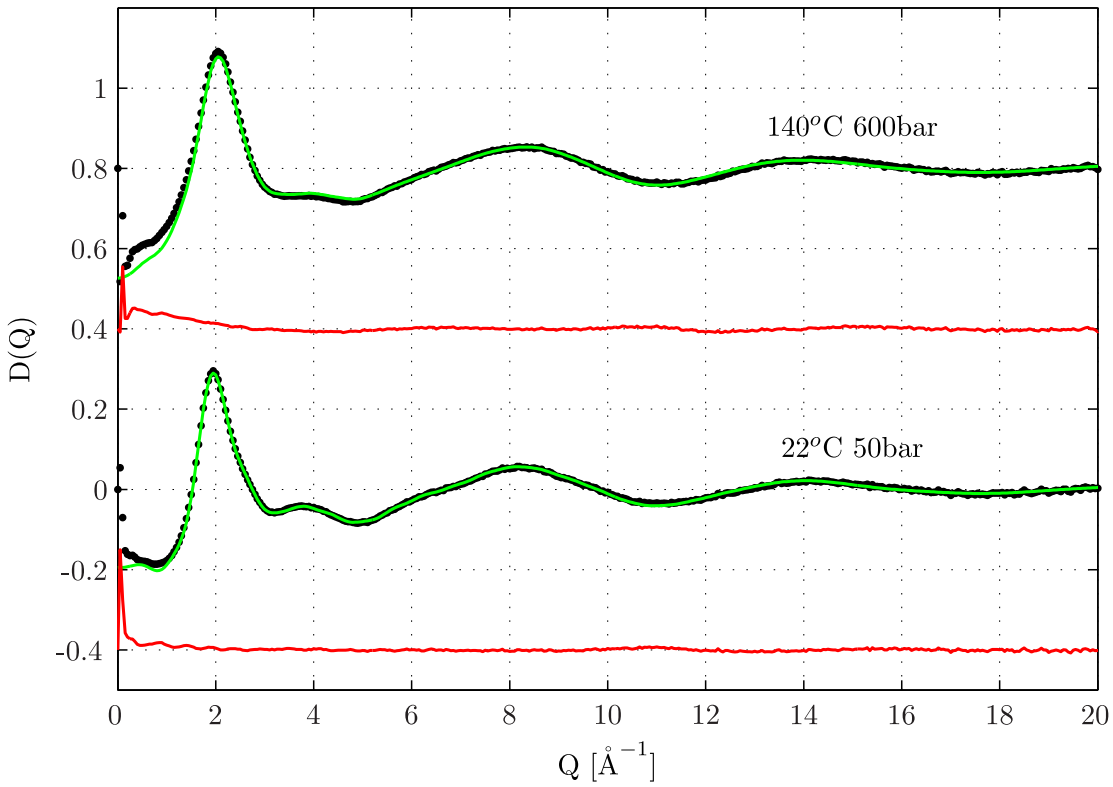


Figure 4.6: $D_i(Q)$ from EPSR simulation (green), F(Q) of the data (black circles), residuals (red) for bulk solvent $D_2O$. See that fit to data is extremely good and supported by minimal residuals which are only significant at very low Q.

### 4.4.4 Pressure and Temperature Effects on Pure $D_2O$

In order to draw conclusions about the effect of TMACl on the structure of the solvent and the effects of an increase in p & T on the structure of the solutions, first we must look at the effect of an increase of pressure and temperature on the bulk solvent, $D_2O$. Figure 4.6 shows the EPSR fit to the reduced data acquired from Gudrun for the pure $D_2O$ solvent. The EPSR shows an extremely good fit to the data as the residuals are only significant at low-Q. This is similar as with the 1M TMACl solutions in Figure 4.5 and is due to imperfect removal of inelastic scattering.

To begin the structural examination, the pairwise distribution between the water molecules in the pure $D_2O$ sample was investigated as a function of pressure and temperature.

At 22°C 50 bar, the hydrogen bond length $g_{OD}(r)$ for bulk $D_2O$ is 1.8 Å. There is a slight discrepancy with measurements made by Soper[129] at ∼1.85 Å but can be explained by the fact that there is 50 bar pressure in the ambient readings in this investigation. This first peak position for all 3 water RDFs shift to slightly smaller values when the pressure is

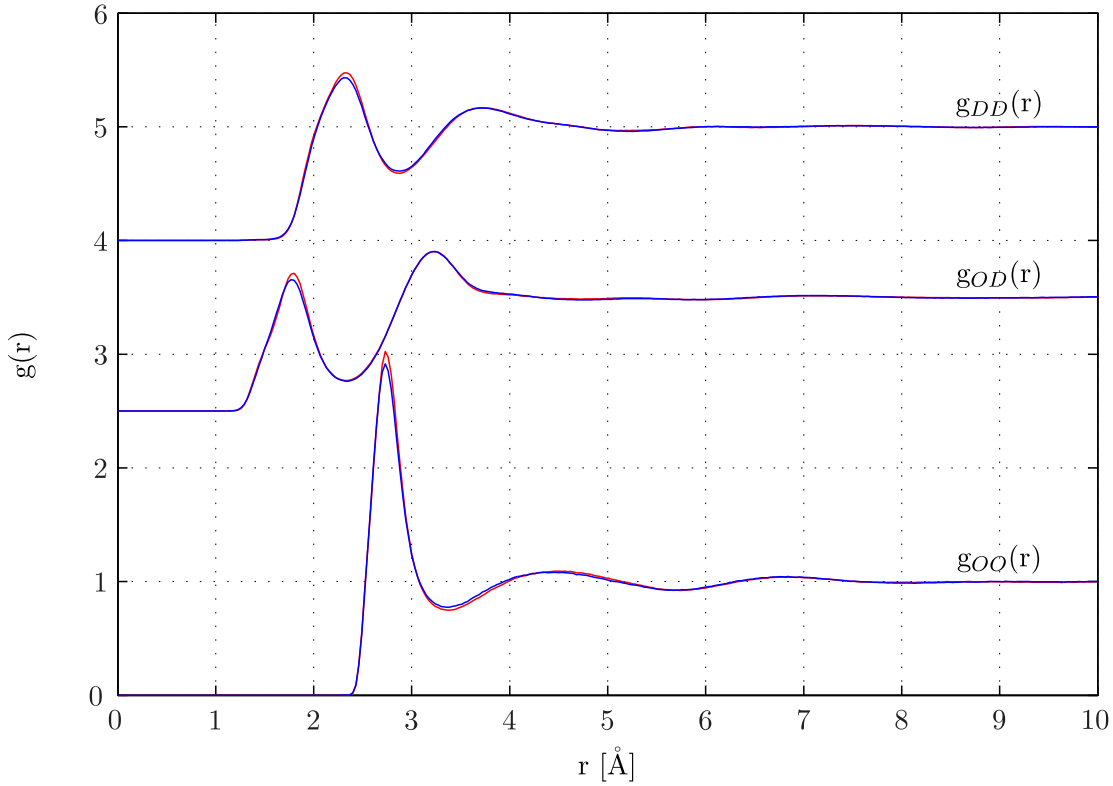


Figure 4.7: Site-site partial RDFs for all atomic pairings of the water molecule in bulk $D_2O$. The RDFs are taken from the EPSR analysis of the neutron diffraction data of bulk $D_2O$ at 22°C 50 bar (red) and 22°C 600 bar (blue) to isolate the effect of pressure. The RDFs are almost indistinguishable other than a small decrease in intensity and shift in the first peak by 2% to smaller $r$.

increased to 600 bar which is to be expected as the system is in a constant volume regime and an external pressure is being applied. The first peak position for the $g_{OD}(r)$ shifts down from 1.8 Å to 1.77 Å (a small change of 2%). This is reasonable as the molecules are squeezed together under the applied hydrostatic pressure, and therefore peaks will shift to smaller $r$ values.

Figure 4.8 isolates the effect of temperature on the system as it is increased from ambient through to 140°C. As the system moves from 22°C to 140°C, it gains thermal energy and the system becomes more disordered. Thus the bonds are weakened and there is a dramatic decrease in the 1st peak intensity and broadening in peak width. The average position in the highest disordered state has shifted back to 1.8 $\mathring{A}$ as for the ambient run indicating that the increase in temperature acts to undo the effect of the applied external pressure.

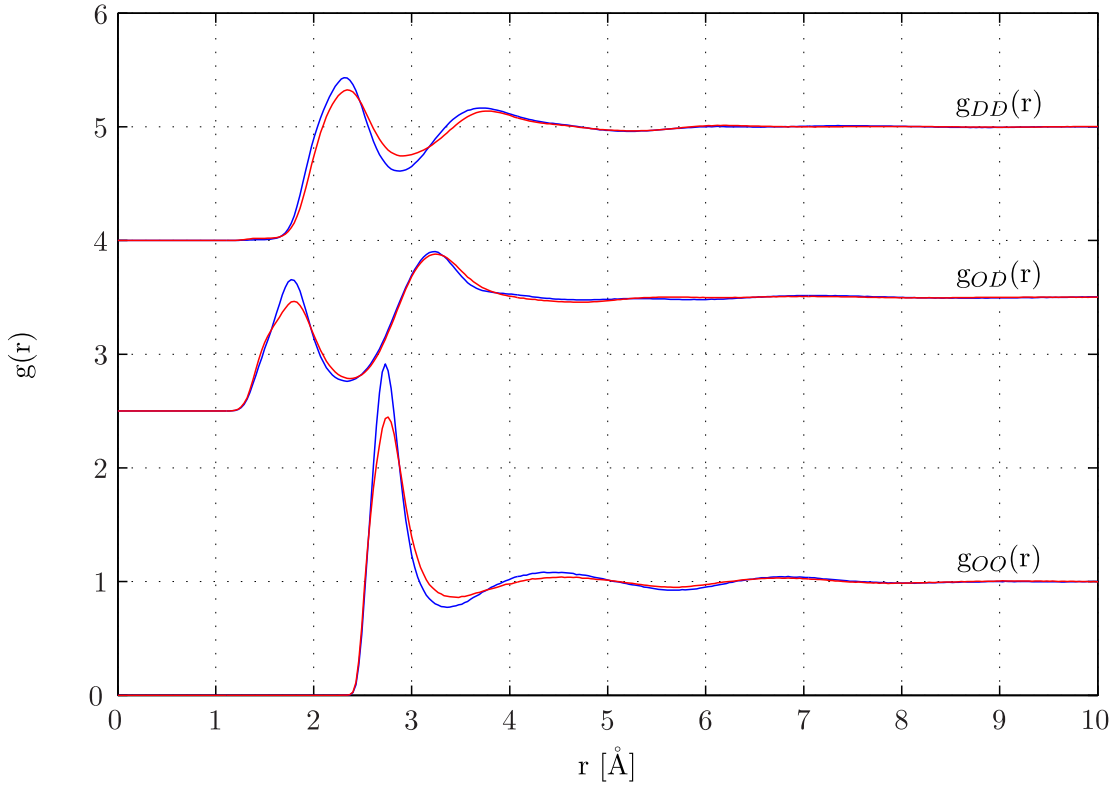


Figure 4.8: Site-site partial RDFs for all atomic pairings of the water molecule in bulk $D_2O$ at constant pressure at 22°C (blue) and 140°C (red). Note here the decrease in intensity and broadening of the first peak indicating greater disorder within the system. Also note the slight shift (2%) of both peaks to higher $r$ values implying an inverse effect of pressure and temperature on the system.

### 4.4.5 Inter-solvent Structure Comparison: 1M TMACl vs Pure $D_2O$

We can now attempt to study the effect of the $TMA^+$ and $Cl^-$ on the inter-solvent structure at these pressures and temperatures. From the resulting EPSR ensemble, the individual site-site radial distribution functions (RDFs), $g_{\alpha\beta}(r)$, for the relative density of atoms of type $\beta$ as a function of their distance $r$ from one atom of type $\alpha$, can be extracted.

The solvent-solvent structure is disseminated in two manners:

1. Investigating the influence of the dissolved TMACl on the solvent structure compared to bulk solvent at specific p/T state points.

2. Investigating the effect of elevated pressures and temperatures on solvent structure within the TMACl solution.

In order to study the evolution in solvent-solvent structure, the analysis focusses on

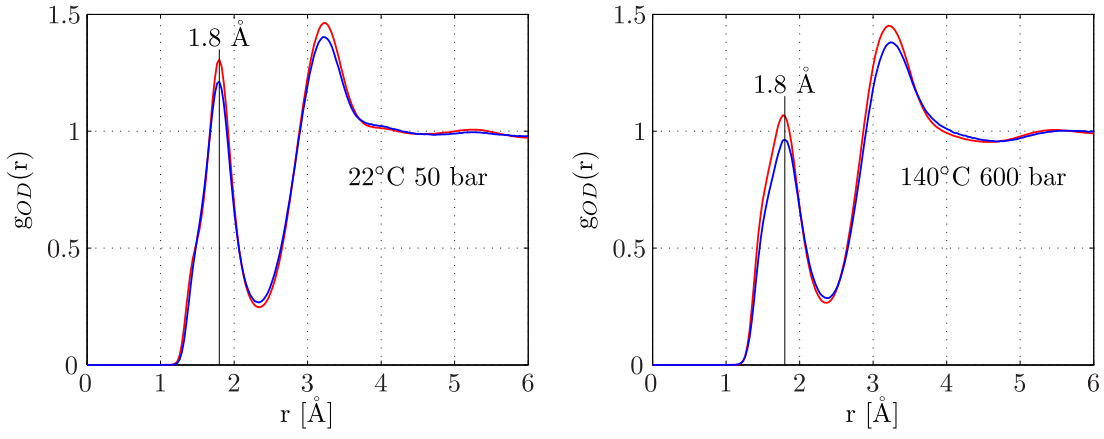


Figure 4.9: $g_{OD}$(r) for pure bulk $D_2O$ (blue) and solvent $D_2O$ in 1M TMACl solution (red) at **(a)** 22°C 50 bar (ambient) and **(b)** 140°C 600 bar. Both peaks are of greater intensity with the addition of TMACl due to the reorganisation of water molecules for the solvation of TMA and Cl ions. There is no change in peak position between bulk and salt solution indicating that although there is increased inter-solvent, the bulk like water structure is preserved.

the changes to the solvent $g_{OD}$(r) RDF (hydrogen-bond).

Figure 4.9 shows the hydrogen bond in the solvent structure in **(a)** pure $D_2O$ and **(b)** in 1M TMACl at the lowest p/T combination, 22°C 50 bar. There is no shift in peak positions from bulk $D_2O$ to 1M TMACl + $D_2O$ solution with the first peak position centered at 1.8 Å. Both peaks of the solvent-solvent $g_{OD}$(r) in the salt solution are slightly more intense with the addition of the $TMA^+$. This can be attributed to a small increase in intensity of the average local solvent structure reorganisation in accommodating the $TMA^+$ and $Cl^-$. The first peak height increases in intensity by 8% and the 2nd peak by 4% indicating that at 1 molar concentration of TMACl in $D_2O$, there is no huge departure of solvent structure from bulk.

When the solvent-solvent RDFs are compared with bulk at the highest p/T conditions, the system follows the same trends as bulk solvent structure. Figure 4.9(b) shows a comparison between the solvent O-D RDF for bulk and salt solution at 140°C 600 bar. The initial peak for the salt solution at both temperature and pressure conditions are more intense than for bulk indicating that despite the increase in energy to the system, the solvent remains more ordered in the presence of TMACl. A broadening in this initial peak is seen at 140°C 600 bar due to the increase in thermal energy to the system, however

interestingly, it is more pronounced in the salt solution. This can be further investigated by comparing the solvent-solvent RDFs for the salt solutions to isolate the effects of pressure and temperature.

Figure 4.10(a) compares the solvent O-D RDF of the salt solution at **(a)** 22°C 50 bar and **(b)** 22°C 600 bar. As with the bulk solvent measurements, there's a slight (2%) shift of the first peak to smaller $r$ from 1.8 Å to 1.77 Å as the pressure is increased from 50 bar to 600 bar at constant temperature. Again, this is expected with an increase in pressure on the system pushing the intermolecular distances to smaller values.

Figure 4.10(b) shows the effect of temperature on the solvent O-D RDF extracted from the salt solution. The first peak position shifts back to higher $r$ to 1.8 Å. It is accompanied with a dramatic drop in intensity and broadening of this peak due to the increase in thermal energy of the system, as seen with pure $D_2O$.

### 4.4.6 $TMA^+$ - X Correlations and Structure in 1M $TMACl_{(aq)}$

The local structure around the $TMA^+$ can also be determined by looking at the solvent-$TMA^+$ pair distribution functions. Here, the nitrogen atom of the $TMA^+$ cation has been taken as its centre and all $TMA^+$ related correlations will be N-X pair distribution functions.

Figure 4.11(a) shows the TMA – $O_w$ RDF at ambient (red) indicating the first solvation shell of the TMA to reside at a distance of 4.41 Å from the TMA centre. As the pressure is increased to 600 bar (blue), this peak shifts to larger $r$ of 4.59 Å and increases intensity. The first solvation shell around the TMA ion is very slightly more structured at 22° 600 bar compared to ambient but pushed further out from the TMA ion whereas the second shell is pulled closer to the ion from 8.07 Å to 7.44 Å. Interestingly, when the temperature is now increased to 140°, Figure 4.10(b), the first shell shifts back to 4.41 Å and the second shell shifted out slightly to 7.59 Å. This is in contrast to the inter-solvent O-D RDF where both neighbouring shells of a central water molecule responded in the same manner: shifted to smaller $r$ with increased pressure and then higher $r$ with an increase in temperature. The coordination number, derived from integrating under the first peak at ambient conditions, is ∼30 water molecules indicating that 55% of the water molecules are being involved in the first solvation shell of the TMA ion.

The location of the chloride ion with respect to the TMA ion can also be determined. Figure 4.12 shows the nitrogen-chloride RDF with the peak also at 4.41$\mathring{A}$ at ambient

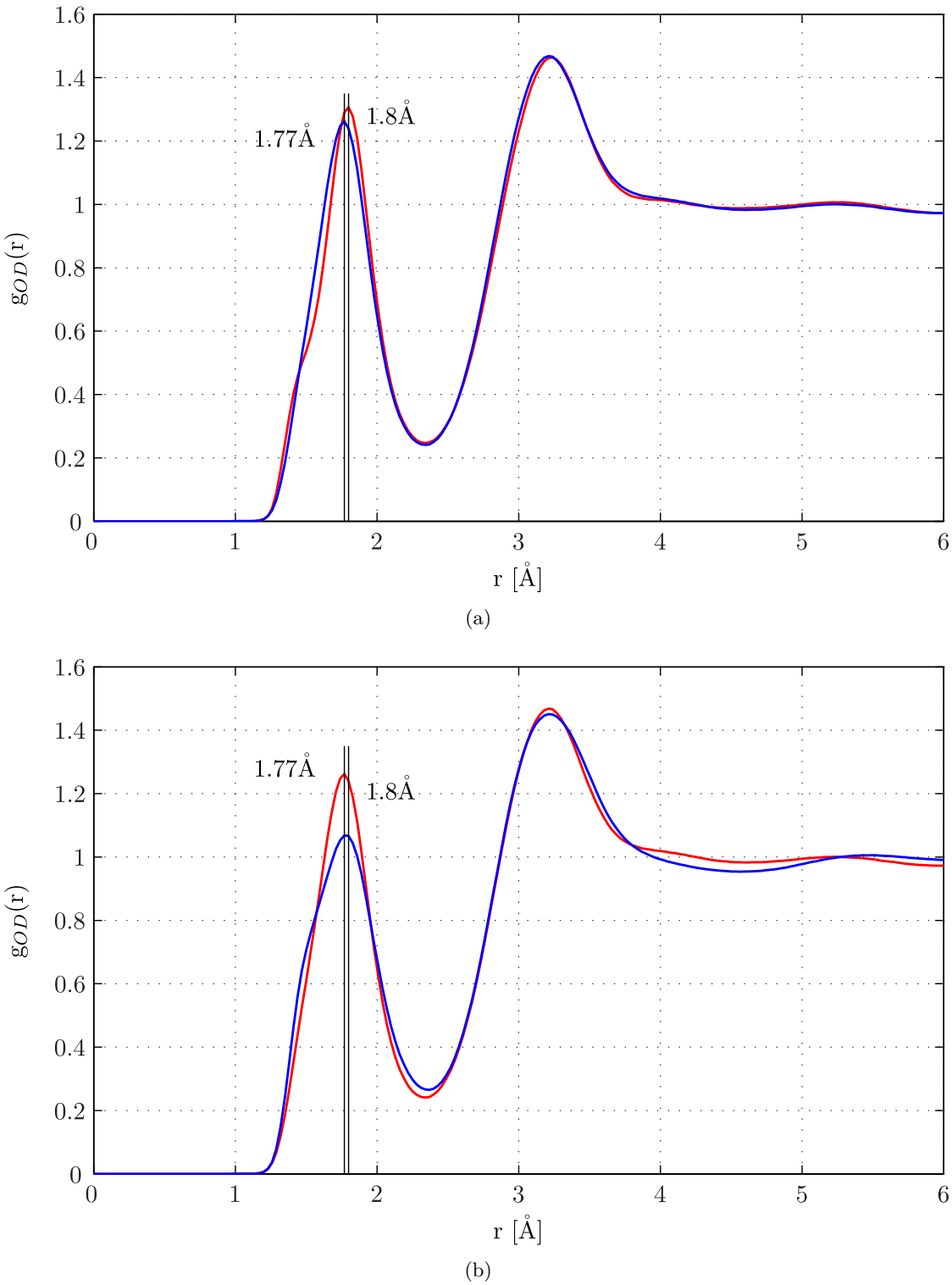


Figure 4.10: $g_{OD}$(r) for solvent $D_2O$ in TMA solution at **(a)** 22°C 50 bar (red) and 22°C 600 bar (blue) and **(b)** 22°C 600 bar (red) and 140°C 600 bar (blue).

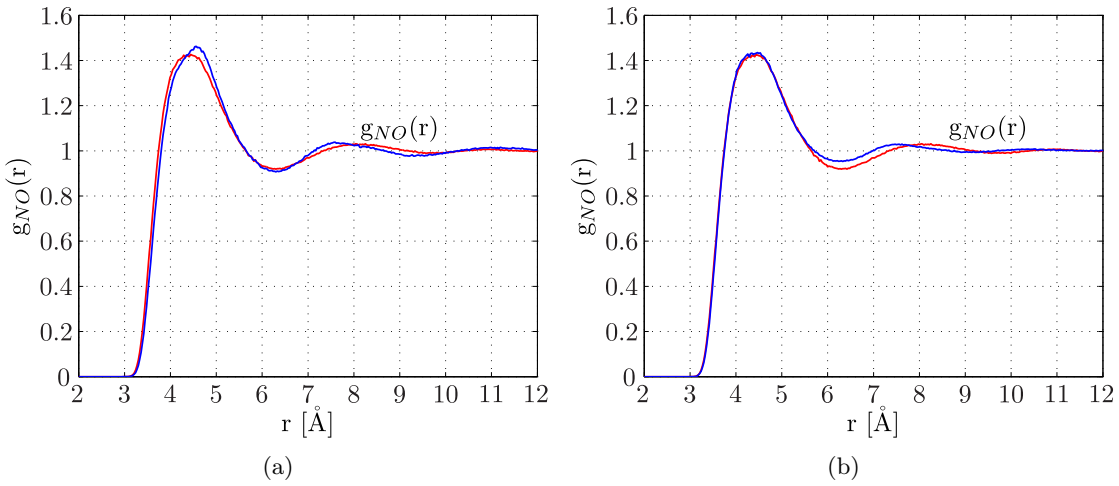


Figure 4.11: $g_{NO}$(r) for TMA solution at **(a)** 22°C 50 bar (red) and 22°C 600 bar (blue) and **(b)** 22°C 50 bar (red) and 140°C 600 bar (blue).

conditions. This indicates that the chloride and TMA ions exist as solvent separated pairs also seen by Soper *et al*[130].

Figure 4.12 also shows the overall change in the N-Cl RDF. Increasing from 22°C 50 bar to 140°C 600 bar does incur a slightly narrower and less intense peak however the chloride stays at the same distance from the TMA centre. This indicates that although the peak at 140°C 600 bar, broadens and is less intense due to increase in thermal energy, the time-averaged structure of the liquid still remains quite robust against the application of the external pressure and temperature. The number of chloride ions found at this distance remains at ∼1 across all p & T thus inferring that the $TMA^+$ and $Cl^-$ stay as solvent separated pairs and do not directly ion-pair. This is also supported by the fact that there is no evidence of small angle scattering in the total structure factors, Figure 4.5.

Figure 4.13 shows the variation in the Cl-Ow RDF with just an increase in pressure to the system at 22°C, from 50 bar (red) to 600 bar (blue), Figure 4.13(a), and with only an increase in temperature at 600 bar, from 22°C (red) to 140°C (blue), Figure 4.13(b). The Cl-Ow peaks at 3.12 Å at ambient and 3.09 Å at 600 bar. The effect of pressure slightly decreases the Cl-O distance which is expected however the increase in temperature incurs an increase in the intensity of the Cl-O RDF indicating the greater solvent structure around the chloride ion. Calculating the coordination numbers, there are ∼6 water molecules in the 1st solvation shell of the chloride ion at 22°C 50 bar. This is in accordance with investigations into halide ion solvation at low salt concentrations[131,132]. The 1st solvation shell of the chloride ion does not alter greatly with increasing p & T with the coordination

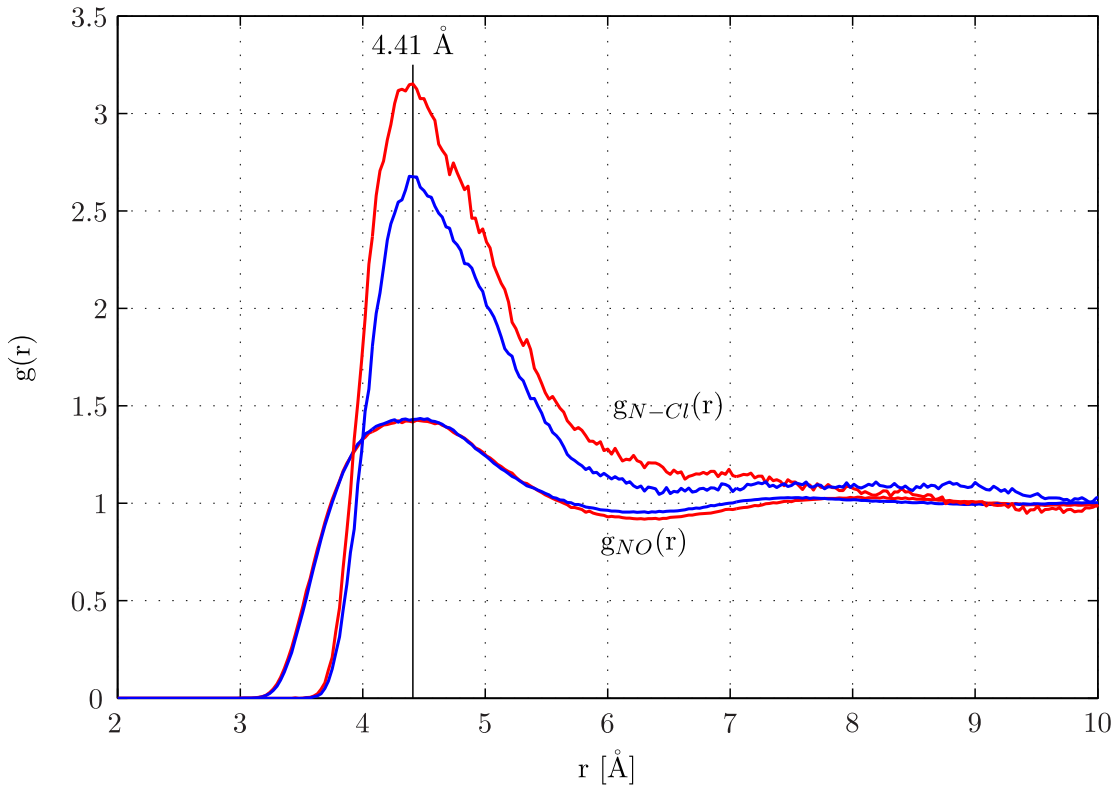


Figure 4.12: Site-site partial RDFs for N-O (TMA-O) and N-Cl ((TMA-Cl)) at 22°C 50 bar (red) and 140°C 600 bar (blue). Notice minor perturbation to $g_{NO}(r)$ as compared to $g_{N-Cl}(r)$ with increasing p & T.

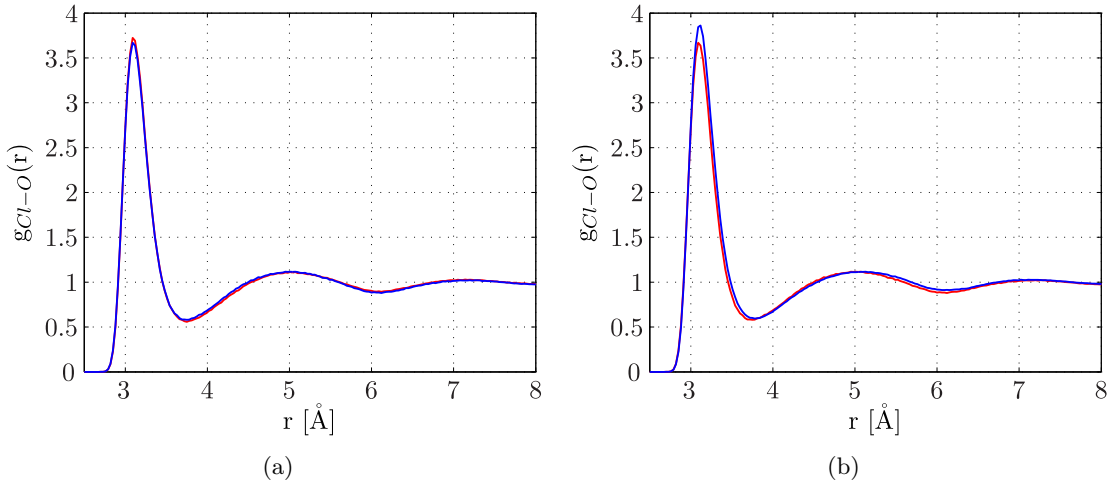


Figure 4.13: $g_{NO}(r)$ for TMA solution at **(a)** 22°C 50 bar (red) and 22°C 600 bar (blue) and **(b)** 22°C 50 bar (red) and 140°C 600 bar (blue).

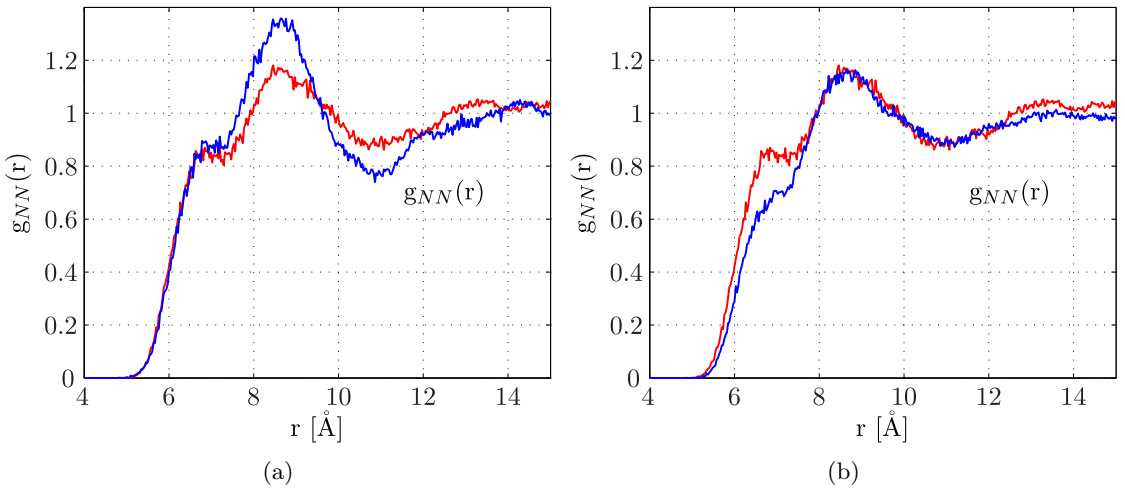


Figure 4.14: **(a)** 22°C and 50 bar (red) and 22°C 600 bar (blue). The first shoulder is maintained with increasing pressure, and the 2nd (main) peak increases in height and narrows. TMA ions are forced closer together with application of pressure. Nitrogen-nitrogen RDFs at **(b)** 22°C and 50 bar (red) and 140°C 600 (blue) bar to show overall effect of combined p & T. The initial shoulder decreases in intensity and TMA ions are pushed into the second preferred orientation and distance.

of water molecules in this shell increasing slightly to ∼6.2 molecules at 140°C 600 bar. This is similar to the remarkable independence of the 1st solvation structure to the increase in salt concentration[115,125,131] which is due to the energetic costs to the system in order for a change in the solvation shell to occur[133]. Overall, the perturbation to the system of the increase in pressure and temperature is relatively small. The application of pressure reduces the inter-molecular, inter-solvent distances, however the thermal energy given to the system with the increase in temperature increases the disorder in the system and causes an overall broadening of the RDFs and small increases to the RDF distances. The hydrogen bonding network of the solvent water molecules remains and resembles that of bulk solvent at the same conditions with the exception of a small increase in the structure in the presence of the salt. This is because the TMA ion has a large surface area over which the ionic charge is distributed therefore there is minimal binding to the water molecules. It is observed that the interactions between the TMA-Ow and the TMA-Cl compensate in order to preserve the hydrogen bonding network of the solvent at higher p & T as this is the lowest energy state of the intersolvent $D_2O$.

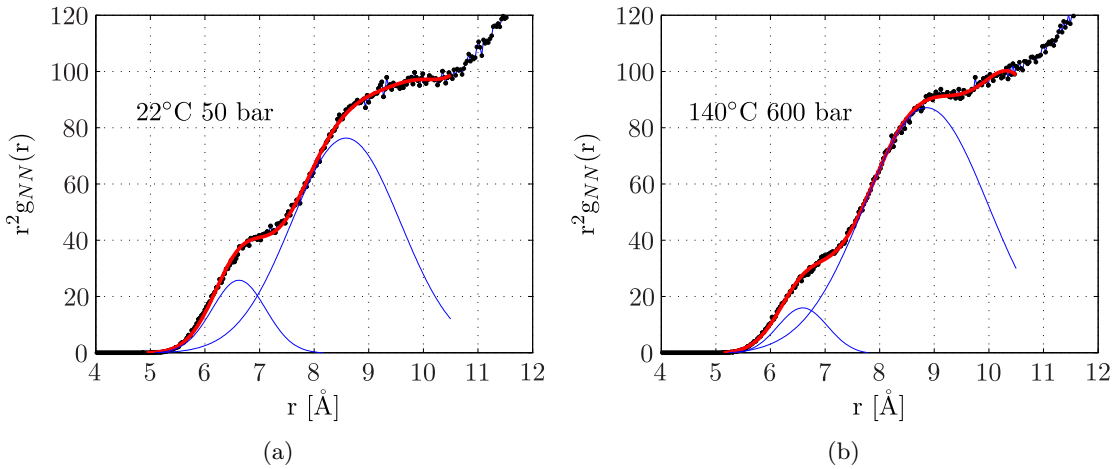


Figure 4.15: Gaussian fits to $r^2g_{NN}$ at **(a)** 22°C 50 bar and **(b)** 140°C 600 bar. The dots show the measured data, the lines show the error bars, the red line the total Gaussian fit and the individual Gaussian peaks in blue.

### 4.4.7 $TMA^+$ – $TMA^+$ Correlations

In order to analyse the $TMA^+$-$TMA^+$ correlations, we must look at the nitrogen-nitrogen pair distribution functions shown in Figure 4.14.

Figure 4.14(a) shows the effect of an increase in pressure from 50 bar to 600 bar on the N-N pair distribution function. Initially at 22°C and 50 bar (red), the main peak is at 8.64 Å and the initial smaller peak is at 6.84 Å with the distance of closest approach at 4.95 Å. This indicates that the Van der Waals radius of the TMA ion as measured by neutron diffraction at 22°C 50 bar is 4.95 Å in agreement with Turner *et al*[116]. The presence of two peaks show that the TMA ion cannot be assumed to be spherical and has two orientations in which closest approach can occur. Since the TMA-$O_w$ distance is 4.41 Å, solvent separated ions should be at a distance of ∼8.82 Å and therefore it can be deduced that the second peak is due to this.

As the pressure is increased, the second peak becomes sharper and more intense indicating that the orientation the $TMA^+$ adopts in the second peak is preferred and the N-N structure increases. However, when the temperature is increased to 140°C, Figure 4.14(b), the first peak diminishes greatly and the second distance, at 8.70 Å, becomes more favourable.

Figure 4.15 shows the calculation of the coordination numbers at 22°C 50 bar (4.15(a)) and 140°C 600 bar (4.15(b)). This is achieved by fitting Gaussians to the $r^2g(r)$[134]. At 22°C 50 bar, the coordination number in the first shell is 0.2 atoms and in the second shell

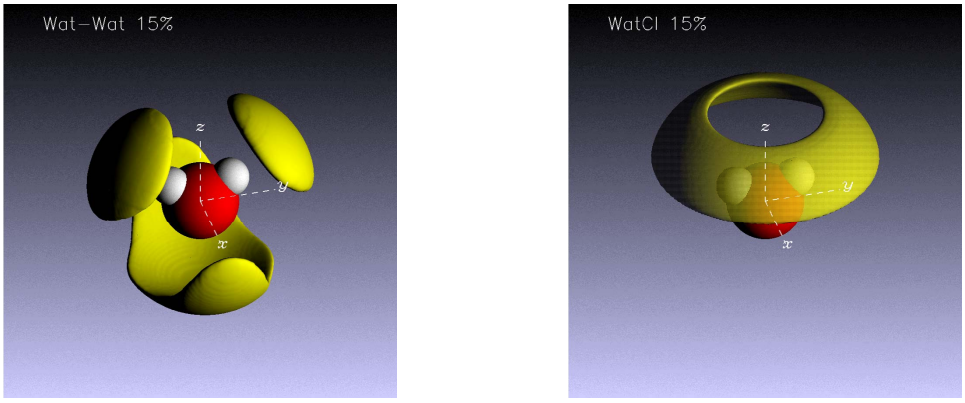


(a) (b)

Figure 4.16: Spatial density functions (SDFs) for **(a)** the 15% most likely positions for solvent $D_2O$ molecules around other solvent molecules and **(b)** the 15% most probable positions for chloride ions correlated around a solvent molecule. SDF for solvent $D_2O$ in 1 M TMACl solution showing the most likely positions for molecules in the 1st coordination shell (0–5 Å) at 22°C 50bar (ambient). Oxygen - red, deuterium - white, probability density of coordinating molecule/atom - green. These are plotted to show that EPSR has extracted reasonable water-water and water-chloride correlations from the data.

is 1.3 atoms indicating that there is a preference of solvent separated pairs. At 140°C 600 bar, the coordination numbers in the first shell and second shell are 0.1 atoms and 1.5 atoms respectively. Thus corroborating the fact that the preference for solvent separated pairs at the elevated conditions remains.

Across all RDFs, it is clear that the application of both temperature and pressure together, act to maintain relatively bulk like solvent structure with the slight increase in overall structure from bulk to salt solution.

### 4.4.8 Spatial Density Functions

Knowing the relative distances atoms are from each other (radial distribution functions extracted from the EPSR simulation above), the 3-dimensional local structure around various molecules can be probed using spherical harmonic representation. The probability density from the RDF is plotted as an iso-surface and fractions of this iso-surface can be chosen to visualise the most likely positions of the probability density. For example if 20% of an iso-surface is plotted, this image describes the 20% most likely positions for any given 3 dimensional correlation.

As a test, the 3-dimensional water correlations (and therefore its structure) at ambient pressure and lowest pressure are shown in Figure 4.16. It is clear that in the first solvation shell of water, the highest probability of finding another water molecule is above

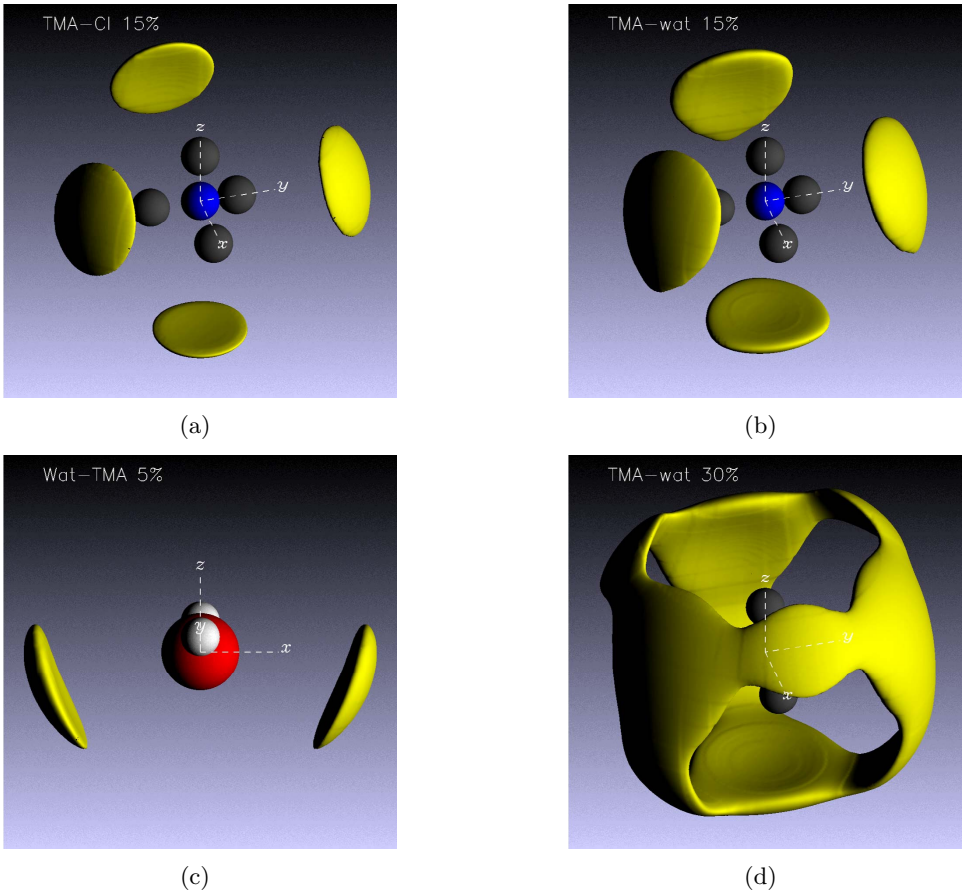


(a) (b)

(c) (d)

Figure 4.17: Spatial density functions from 0 – 5 Å for $TMA^+$ correlations in 1M in salt solution at 22°C 50 bar (ambient). Key: Blue-nitrogen, Black-methyl group, Red-Oxygen, White-deuterium. **(a)** Probability density of 1st solvation shell of $Cl^-$ co-ordinating $TMA^+$. **(b)** Probability density of 1st solvation shell of solvent water molecules co-ordinating $TMA^+$. **(c)** Probability density of 1st solvation shell of $TMA^+$ co-ordinating solvent water molecules. **(d)** Co-ordination of solvent molecules around $TMA^+$ at a fractional iso-surface of 30%.

the hydrogen electron density and the lone-pairs of the oxygen, Figure 4.16(a). For the chloride-water SDF, the negatively charged chloride ion has a probability density that sits above the hydrogen electron density. It is calculated as a ring above the hydrogens as the water molecule can rotate about the $z$-axis and the probability is averaged over $\theta_l$. The first solvation shell of solvent water molecules coordinating a central solvent water molecule is shown in Figure 4.16(a). The probability density is over the deuterium electronic density implying a directionality of the hydrogen bond and over the oxygen at the apex of the molecule. As expected, due to the spherical nature of the chloride ion, the $Cl^-$ probability density forms a circular ring over the deuterium of the water molecule seen in Figure 4.16(b). Both these plots show reasonable inferences of water-water and

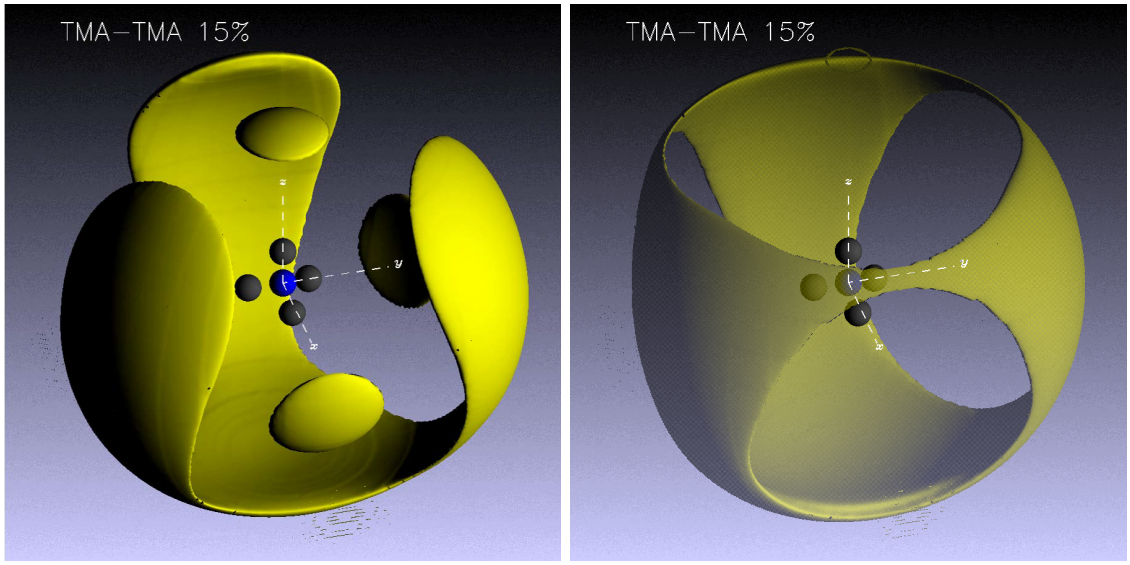


(a) (b)

Figure 4.18: Spatial density functions showing the 15% most likely positions for $TMA^+$ around a central $TMA^+$ ion in 1M TMACl solution in the region of 0 – 10 Å, at **(a)** 22°C 50 bar and **(b)** 140°C 600 bar. At ambient, the SDF clearly shows the 2 positions where the second TMA can be found with respect to a central TMA ion (plotted) as seen in the $g_{NN}(r)$.

water-chloride correlations and we can therefore look toward the SDFs calculated for TMA solvation.

Figure 4.17 shows the 3-dimensional correlations for the TMA ion at 22°C 50 bar (ambient) in a 5$\mathring{A}$ radius from its centre. A tetrahedral coordination around the TMA ion of the chloride ions and the water molecules is seen with their probabilities situated in the faces of the tetrahedron. This corresponds to the first peak in the N-Cl and N-O RDFs at 4.41 Å. If a larger fraction of the probability density for the solvent co-ordinating a central $TMA^+$ is plotted, shown in Figure 4.17(d), it is clear that the secondary position for the solvent molecules is on the edges of the tetrahedron, corresponding to a distance of 8.1 Å thus forming a cage like structure around the TMA ion. Figure 4.17(c) shows the co-ordination of the $TMA^+$ around the water and it is clear that the water molecule orients itself such that the two hydrogens can form two hydrogen-bonds in bulk like tetrahedral arrangement. I.e the TMA ion does not disrupt the hydrogen-bond network of the solvent $D_2O$.

Figure 4.18 shows the 15% mostly likely $TMA^+$ – $TMA^+$ 3-dimensional correlations at 22°C 50 bar and 140°C 600 bar. The inner lobes at 22°C 50 bar in Figure 4.18(a), correspond to the shoulder at 6.84 Å and here the spatial density plot indicates that the

methyl groups point toward the 2nd TMA ion and the outer region lies in the faces of the central TMA ion. Also visible is the 3-fold symmetry of the tetrahedral TMA ion. At 140°C 600 bar, the inner lobes disappear and the probability of the second TMA is more evenly distributed over the faces of the central TMA ion. We can discern the orientation of the 2nd TMA ion with respect to this central ion in both of the regimes by taking 2-dimensional slices of the SDF and fixing the orientation of the 2nd TMA ion.

Figure 4.19 shows the orientation of the TMA ions with respect to each other in the two peaks of the $g_{NN}(r)$ at 22°C 50 bar. If we look along the $x$-axis of the first TMA ion, keep the second fixed with identical Euler angles with respect to the first and make a 2-dimensional plot of the probability as a function of $(r, \Phi_m)$ of the second TMA ion, we see that at closest approach, the TMA ions are corner to face, Figure 4.19**(a)**. Looking through the face of the first TMA ion, and fixing the second TMA ion at $(\phi_m, \theta_m, \chi_m = 180, 0, 0)$ w.r.t the first ion, one can similarly plot the probability as a function of $\Phi_m$, Figure 4.19**(b)**. The axes in the corner denote which projection the TMA ion is pictured in. In this case, the second peak at 8.64 Å is primarily a result of TMA ions being face to face, however other orientations of the second TMA ion do contribute to this peak too indicated by the lack of sharp edges to the probability distribution. This is also the preferred orientation of the TMA ions at closest approach with increasing p & T.

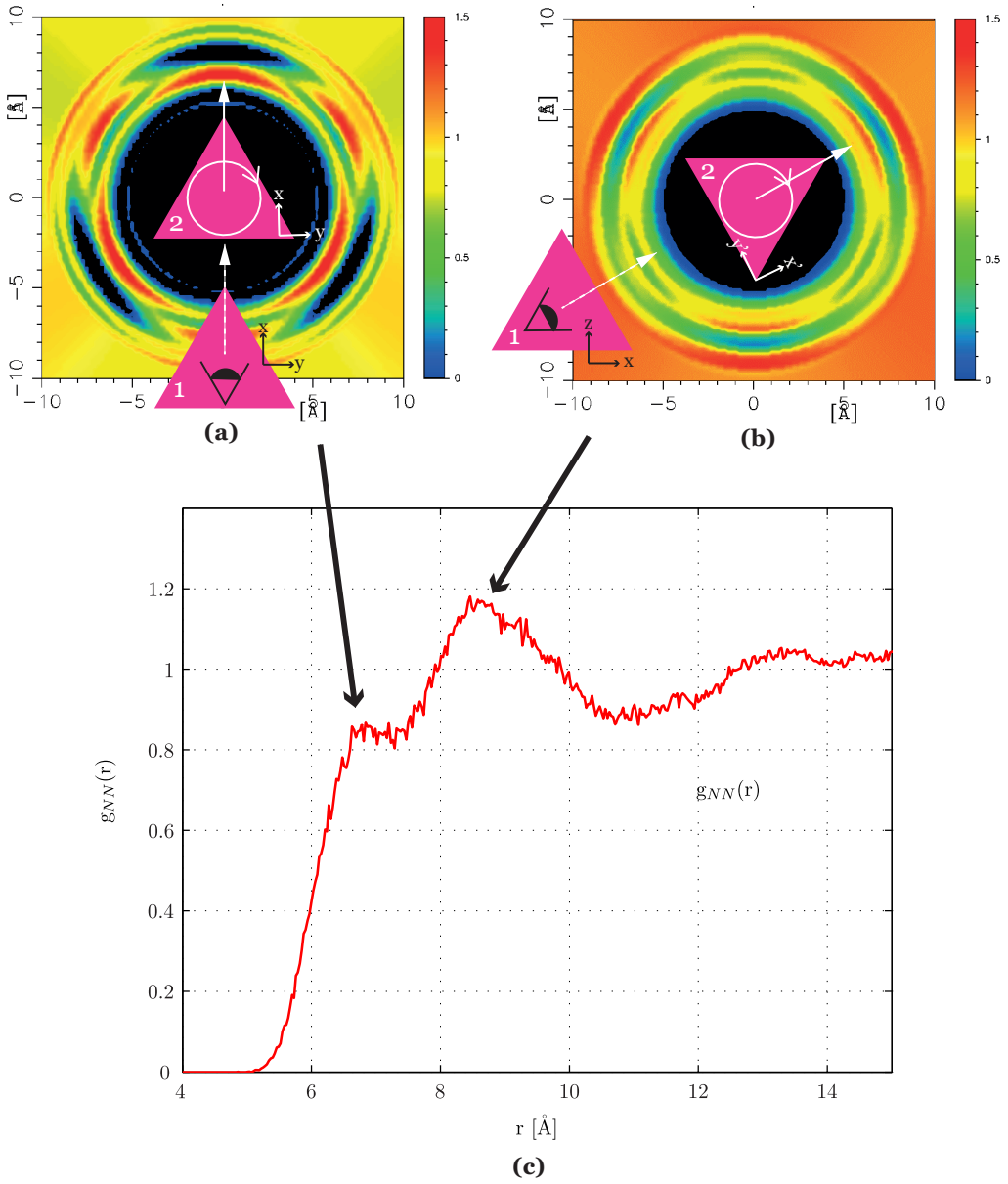


Figure 4.19: 2-dimensional plot in polar coordinates from $r = 0 - 10$ Åof the second TMA ion, denoted '2', for rotation about $\Phi_m$ (white circle) when looking along **(a)** $x$-axis of first TMA ion denoted '1' and **(b)** when looking through the face of first TMA ion and second is at $(\phi_m, \theta_m, \chi_m = 180, 0, 0)$ w.r.t the first ion. The first TMA ion is fixed at the origin of the laboratory coordinates and the second is described using Euler angles with respect to the first. Dotted arrow denotes which direction we are looking along. Solid arrow denotes $\phi_m = 0°$

| Sample No. | $(ND_2)$H-HMDA (g) | H-HMDA (g) | 1,6 $D_4$-HMDA (g) | $D_2O$ (g) | Molarity (M) |
|---|---|---|---|---|---|
| 1 | - | 11.6232 | - | 56.0140 | 1.977 |
| 2 | - | - | 2.3975 | 11.1100 | 1.987 |
| 3 | - | 1.1784 | 1.2215 | 11.2416 | 1.999 |
| 4 | 0.5055 | - | - | 2.2200 | 1.915 |

Table 4.4: Masses and molarity for each of the isotopically substituted samples: fully H, 1,6-$D_4$ and H:$D_4$ 50:50 of the HMDA molecule.

## 4.5 Structure of Hexamethylene diamine at Ambient Conditions

This section presents the data for neutron diffraction taken on the NIMROD beamline at ISIS to probe the structure of 2 molar hexamethylene diamine (HMDA) in $D_2O$ at ambient conditions. Similarly to the quaternary ammonium salt $TMA^+$, HMDA is used as a clay swelling inhibitor but it has two key differences from the TMA ion: it is not ionic but has two polar amine head groups and it has a long hydrophobic chain backbone. In considering the structural implications of the 2 molar HMDA aqueous solution, the following points will therefore be addressed:

**Aims**

- How does the HMDA perturb the water-water (inter-solvent) structure of the solvating $D_2O$?

### 4.5.1 Methodology

Four isotopically distinct samples of 2 molar $HMDA_{(aq)}$ were prepared shown in Table 4.4. Due to the lack of availability of a fully deuterated HMDA molecule, the 1,6$D_4$–hexamethylenediamine isotope Figure 4.20 was used for the deuterated $HMDA_{(aq)}$ measurements. Also synthesized were deuterated amine $ND_2$ end groups on hydrogenated backbones. This was possible by successive washing and drying of the fully hydrogenated HMDA in $D_2O$. Deuterating the amine end groups would ensure that all hydrogen scattering in the data was from the HMDA backbone only.

Since these runs were only to be performed at ambient conditions, a 1mm thick TiZr sample can with a beam size of 30 × 30 mm was used. This allowed for more of the sample to be illuminated in the beam and minimised multiple scattering events compared to data

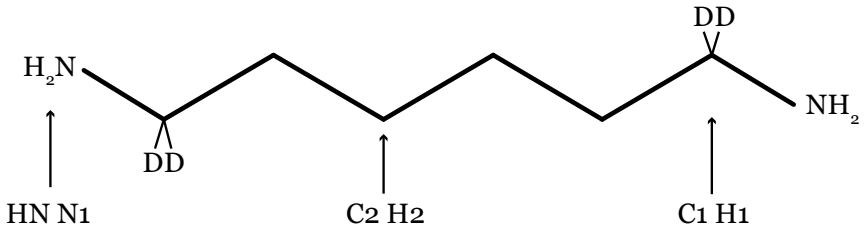


Figure 4.20: Deuterated isotope of HMDA: 1,6 $D_4$–hexamethylene diamine. Notation below arrows describe the labels used for the specific atomic species in the EPSR simulation.

| **Atom Type** | $\sigma$ (Å) | $\epsilon$ (kcal mol$^{-1}$) | **Charge, q** (e) |
|---|---|---|---|
| **C1** | 3.7 | 0.8 | −0.07459 |
| **H1** | 0 | 0 | +0.09083 |
| **C2** | 3.7 | 0.8 | −0.16140 |
| **H2** | 0 | 0 | +0.09083 |
| **N1** | 3.2 | 0.7 | −0.35296 |
| **HN** | 0 | 0 | +0.14256 |
| $\mathbf{O}_{water}$ | 3.1 | 0.65 | −0.8476 |
| $\mathbf{H}_{water}$ | 0 | 0 | +0.4238 |

Table 4.5: Potentials used in EPSR analysis of form:
$V_{ij}(r_{ij}) = \frac{q_i q_j}{r_{ij}} + 4\epsilon_{\alpha\beta}\left[\left(\frac{\sigma_{\alpha\beta}}{r_{ij}}\right)^{12} - \left(\frac{\sigma_{\alpha\beta}}{r_{ij}}\right)^{6}\right]$

taken for the $TMA_{(aq)}$. Data was collected for 3 hours on each sample.

Data reduction was performed in the same manner as described in Section 4.3 and EPSR was used to fit and analyse the data.

#### Simulation Details

EPSR simulations were carried out on each of the four diffraction data sets. The simulation box had sides of length ∼37.8Å containing 1400 $D_2O$ molecules and 50 HMDA molecules, therefore a ratio of HMDA:$D_2O$ of 1:28. MOPAC[126] was run on the HMDA molecule and charges are distributed according to the solution of the AM1 Hamiltonian given in Table 4.5. The labelling of the atoms on the molecule is shown in Figure 4.20. SPC/E parameters taken from Berendsen *et al*[127] are used for the D and O in $D_2O$ molecules and the $\sigma$ and $\epsilon$ for HMDA are given from MOPAC. The density was calculated by incorporating the HMDA molecule by volume in its solid state.

A representation of the system is shown in Figure 4.21.

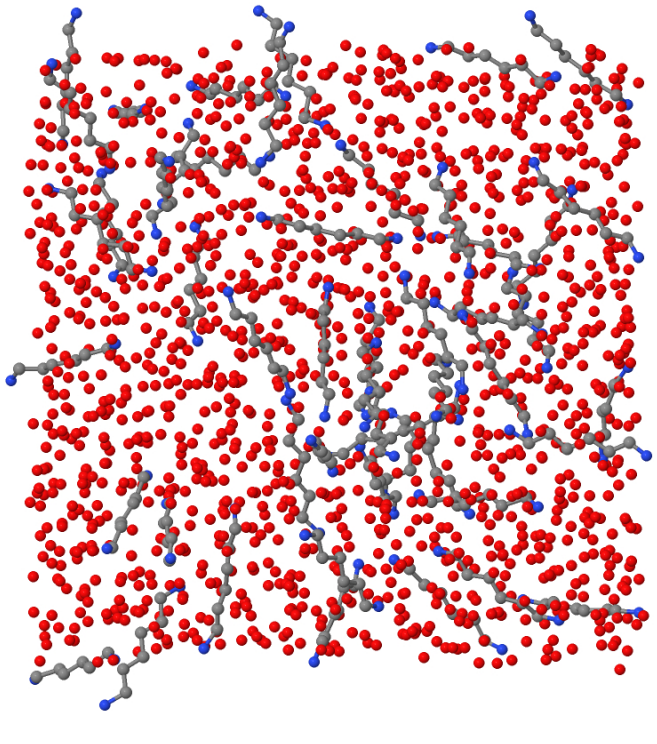


Figure 4.21: Snapshot of ensemble box for 2 molar HMDA solution in $D_2O$ taken when the EPSR has completed fitting the diffraction data for the ambient measurement. Key: Nitrogen-blue, Carbon-Grey, Oxygen-red. All hydrogen atoms have not been displayed for clarity.

### 4.5.2 Total Structure Factor

The fits of the EPSR ensemble ($D_i(Q)$, green lines) to the total structure factors (F(Q), black circles) derived from Gudrun for the four samples at ambient conditions are shown in Figure 4.22. The data for the full $Q$-range from 0.02 $Å^{-1}$ to 30 $Å^{-1}$ has been plotted.

The EPSR fits closely represent the data but at low-$Q$, there are observable discrepancies between the fit and the data. Again, this is due to an imperfect removal of inelastic scattering[124,128] and since the samples are highly concentrated and hydrogen is present in all data sets, the removal of the inelastic is very difficult to perform. Otherwise, all other features are reproduced well enough to comment on.

### 4.5.3 Inter-solvent Structure: $HMDA_{(aq)}$ vs Pure $D_2O$

The inter-solvent RDFs for the 2 molar aqueous HMDA in $D_2O$ solution are shown in Figure 4.23. Alongside the HMDA are the RDFs for bulk $D_2O$.

It is clear from this figure that the inter-solvent correlations are distorted in the HMDA-$D_2O$ solution when compared with correlations for bulk $D_2O$ in the absence of the diamine.

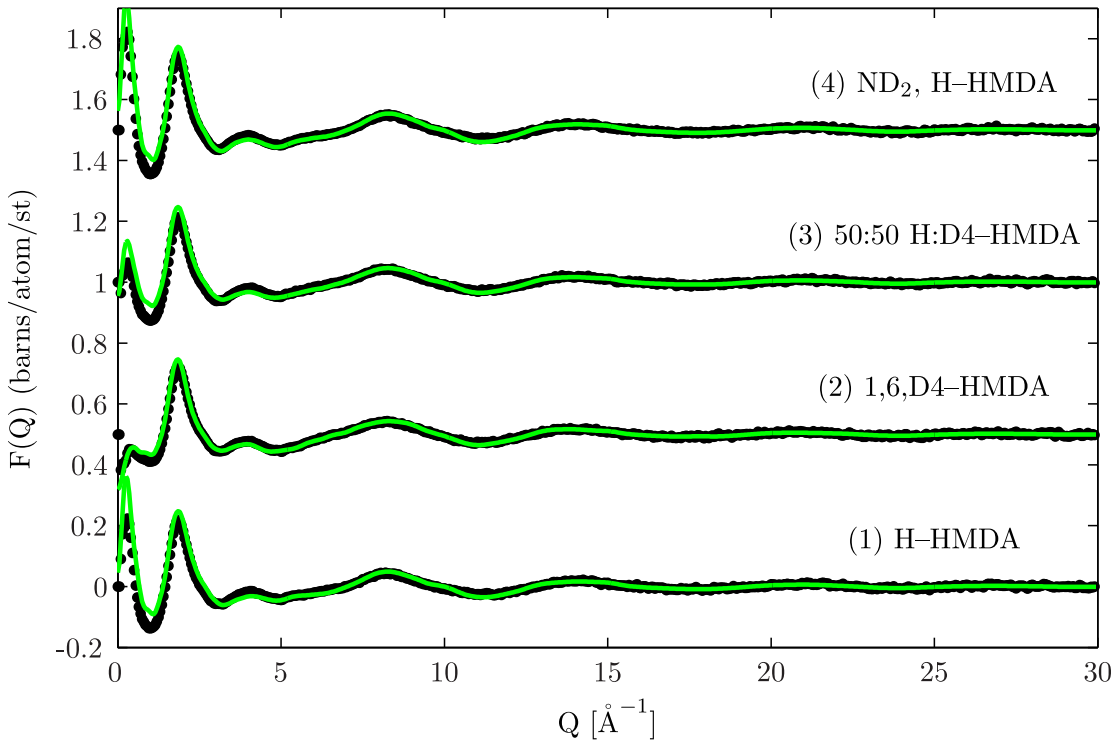


Figure 4.22: The total normalised structure factor F(Q) (black) with relatively good EPSR fits $D_i(Q)$ (green) at ambient conditions for each of the four solutions, (1) $C_6\mathbf{H}_{12}(N\mathbf{H}_2)_2$ in $D_2O$, (2) $C_6H_8\mathbf{D}_4(NH_2)_2$ in $D_2O$, (3) 50:50 $C_6\mathbf{H}_{12}/C_6H_8\mathbf{D}_4(NH_2)_2$ in $D_2O$, (4) $C_6\mathbf{H}_{12}(N\mathbf{D}_2)_2$ in $D_2O$. The results have been shifted vertically for clarity.

The first notable difference between $HMDA_{(aq)}$ to bulk is the dramatic increase in intensity and narrowing of the first peak for both the first and second peak in all three RDFs. This indicates a very highly structured inter-solvent region in the HMDA solution and a significant perturbation to the water structure by the HMDA molecules. This extends out to the third solvation shell since we measure a noticeable third peak in all three RDfs.

If we calculate the coordination numbers in the $1^{st}$ solvation shell for each RDF, Table 4.6, the number of molecules in this shell is slightly smaller in the HMDA solution than it is in bulk. An increased intersolvent structure yet smaller coordination numbers indicates an 'ice-like' structure which has been observed for other ammoniated compounds

| RDF | **bulk $D_2O$** | | **2M $HMDA_{(aq)}$** | |
|---|---|---|---|---|
| | $r_{min}$ [Å] | $n_\alpha^\beta(r)$ | $r_{min}$ [Å] | $n_\alpha^\beta(r)$ |
| $g_{OO}(r)$ | 3.83 | 4.81 | 3.23 | 3.83 |
| $g_{OD}(r)$ | 2.34 | 1.84 | 2.31 | 1.76 |
| $g_{DD}(r)$ | 2.86 | 4.87 | 2.82 | 4.30 |

Table 4.6: Coordination numbers for the water-related RDFs for the 2 molar HMDA solution and Pure $D_2O$ at ambient conditions.

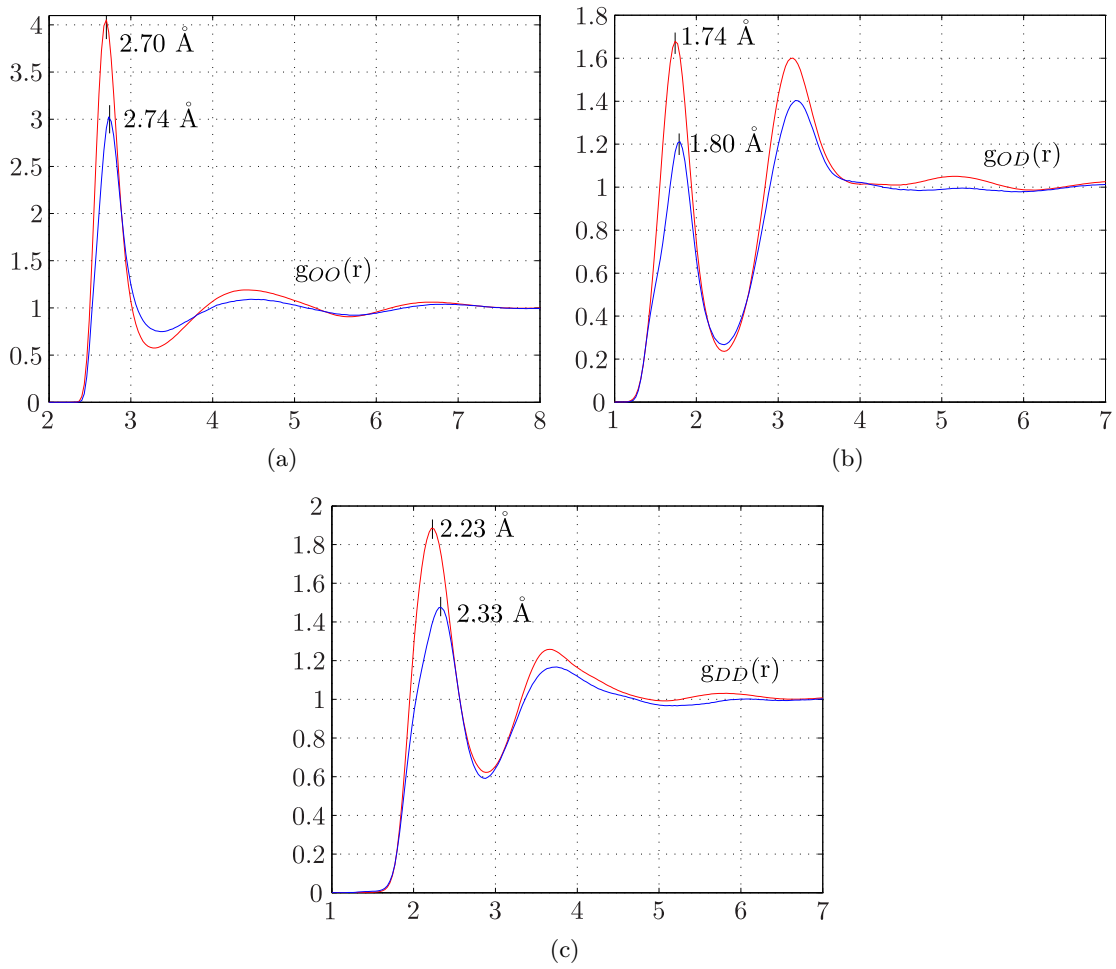


Figure 4.23: All inter-solvent RDFs in 2 molar $HMDA_{(aq)}$ (red) compared to bulk $D_2O$ (blue). **(a)** $g_{OO}(r)$, **(b)** $g_{OD}(r)$, **(c)** $g_{DD}(r)$

at increasing concentration [116]. There is also a small shift of both the first and second peaks to smaller $r$ of the $g_{OD}(r)$ and $g_{OO}(r)$ of $\sim 1.5$ % and can be considered within the error of the analysis. However the shift to smaller $r$ is more noticeable in the $g_{DD}(r)$ of $\sim 4$ %.

## 4.6 Summary

This chapter presents the results from the *in situ* neutron scattering experiment investigating the structure of 1-molar TMACl in $D_2O$ under oil well conditions and the effect of HMDA on the intersolvent structure of a 2 molar solution at ambient conditions. This is the first time hydrophobic salts have been looked at under both elevated pressure and temperature conditions.

We have found that with the addition of the TMA salt, there is an increased intersolvent structure ascribed to the reorientation of the solvent $D_2O$ around the TMA ions.

This behaviour persists with increasing pressure and temperature however follows the same trends as bulk $D_2O$ at the same conditions. The water is observed to orient itself in a cage like structure around the TMA ion such that the the water molecule can still maintain bulk hydrogen bond network. The $TMA^+$ and $Cl^-$ exist as solvent separated pairs throughout increasing p & T conditions and no hydrophobic $TMA^+$ clustering is observed. In terms of its use in the oilfield, the lack of hydrophobic ordering is good since this would hinder cation exchange and the swelling inhibitive effect. Looking at TMA-TMA correlations, the ions have two orientations at closest approach, corner-to-face and face to face however with increasing p & T, a preference for the face to face position is observed indicating that the elevated conditions are pushing the solute molecules apart.

Similarly, we observe a very highly ordered intersolvent structure in the 2 molar HMDA solution. The structure is almost ice-like since the water RDFs occur at slightly small $r$ , are more intense and coordination numbers in the HMDA solution are less than for bulk. The hydrophobicity aspects of the HMDA-water have yet to be probed and simulations determining the spherical density plots are ongoing. This will shed light on any hydrophobic ordering of water molecules around the backbone and HMDA-HMDA correlations.

# Chapter 5

# Interlayer and Pore Structure in Clays - Neutron Study

This chapter presents the results of three neutron scattering experiments:

- The effect of pressure and temperature on TMA exchanged vermiculite - investigating the changes to the interlayer structure with the addition of water.
- The effect of pressure and temperature and 2-molar $HMDA_{(aq)}$ flooding of Li-vermiculite.
- A proof of concept SE-SANS investigation into time resolved changes in pore structure of compacted bentonite with water and brine invasion.

## 5.1 TMA-Intercalated Vermiculite Under Burial Conditions

The results presented here are the first investigation into the effect of combined pressure and temperature on organic-intercalated vermiculite. Neutron diffraction has been performed on TMA-intercalated Eucatex vermiculite from temperatures of 22°C to 200°C combined with pressures of 50 to 800 bar with $D_2O$ flooding. The data has revealed that without the presence of water in the system, the *d*-spacing of the clay is 13.43 Å. With the addition of $D_2O$, this increases to 14.03 Å. This value for the *d*-spacing remains with the application of both pressure and temperature.

The use of amines in wellbore productions and drilling fluids have been exploited for some time[94]. The TMA ion, as described in Section 2.6, has a similar hydration volume to the potassium ion, $K^+$ and has therefore been used in a similar vein to potassium to counteract clay swelling downhole. From the work reported in Chapter 4, we found that there is little perturbation to the inter-solvent structure due to the dissolution of TMACl in $D_2O$ and that there are no prevailing hydrophobic interactions at the higher pressures and temperature. Therefore the following experiment was designed to investigate the extent to which the TMA ion binds the clay sheets against an increase of pressure, temperature and $D_2O$ flooding by monitoring the change of the (001) peak of clay. Previous work on such clay systems have focussed on ambient pressure and temperature conditions in hectorite[135] and vermiculite[136] and non-organic interlayer counter-ions at elevated conditions for vermiculites[25,36].

### 5.1.1 Sample Preparation and Experimental Methods

The NIMROD beamline at ISIS was utilised for the investigation into interlayer structure of TMA-intercalated vermiculite under burial conditions.

The vermiculite sample used for this investigation were from Eucatex, Brazil which naturally occurs as macroscopic single crystals, typically with volume $mm^3$ - $cm^3$, thus making them useful for isolating interlayer behaviour of clay minerals. The vermiculite was pre-prepared with sodium ions in the interlayer region and therefore ion-exchange was carried out by soaking the crystals in 1M hydrogenated-TMACl in $D_2O$ and leaving for 24 hours. It was washed with $D_2O$ and dried at 80°C before each exchange which was performed 6 times. After the final exchange, the clay was washed with $D_2O$ to remove the excess salt and stored fully expanded in $D_2O$. The formula of the TMA-intercalated Eucatex was:

$$Si_{6.30}Mg_{5.44}Al_{1.65}Fe_{0.6}O_{20}(OH)_4 \bullet 1.3(CH_3)_4N^+ \tag{5.1}$$

where the $(CH_3)_4N^+$ is the TMA ion. The TMA-exchanged Eucatex was placed in the vacuum oven for 12 hours at 80°C so that it could be loaded dry into the TiZr null-scattering sample can that was used previously for the $TMA_{(aq)}$ in Chapter 4. The platelets of the clay were loaded such that the *c*-axis of the platelets were in alignment. This allowed for the sample can to be placed in the beam with the *c*-axis perpendicular

| Depth (km) | Temperature (K) | Pressure (bar) |
|---|---|---|
| 0 | 22 | 50 |
| - | 22 | 600 |
| - | 40 | 600 |
| - | 60 | 600 |
| 2 | 80 | 600 |
| 4 | 140 | 600 |
| $\sim 6$ | 200 | 800 |

Table 5.1: Pressure and temperature combinations for each measurement.

to the $Q$-vector of the beam. The contrast in this experiment is between the deuterated clay with all -OH groups exchanged for -OD and the TMA-fully hydrogenated.

Data was first collected on the dry TMA-Eucatex. The system was then flooded with $D_2O$ at 22°C and 50 bar pressure and data collected for 1 hour. This was done at each p & T combination given in Table 5.1. Although it can be argued that 1 hour may not be sufficient due to low neutron flux and therefore higher background and low statistics, since the Bragg peak was quite intense due to presence of hydrogen in the TMA, counting for this long was sufficient.

Data treatment is the same for the liquid diffraction data collected on $TMA_{(aq)}$ described in Section 4.3 however due to the minimal amount of hydrogen in the system, no incoherent scattering corrections were performed. Since the experiment is performed with the $\vec{Q}$-vector perpendicular to the $c$-axis of the clay, the contributions to the final DCS is the interlayer species, small-angle scattering from clay particle size, Bragg peak corresponding to the $d$-spacing of the clay and $D_2O$ for the data sets after the $D_2O$ was added.

### 5.1.2 Results and Discussion

Figure 5.1 shows the DCS against $\vec{Q}$-vector (log $x$-axis) of the baked (dry) TMA-intercalated Eucatex at 22°C and 50 bar pressure. The prominent feature in the DCS is (001) peak of the baked TMA-intercalated Eucatex. This occurs at 13.43 Å which indicates that the $TMA^+$ are in plane within the interlayer region[136]. This is slightly smaller than the measurements made by Vahedi-Faridi[137] and Breu *et al*[135] however this difference is likely since clay in this investigation is deuterated and there are different physico-chemical properties between the two isotopes.

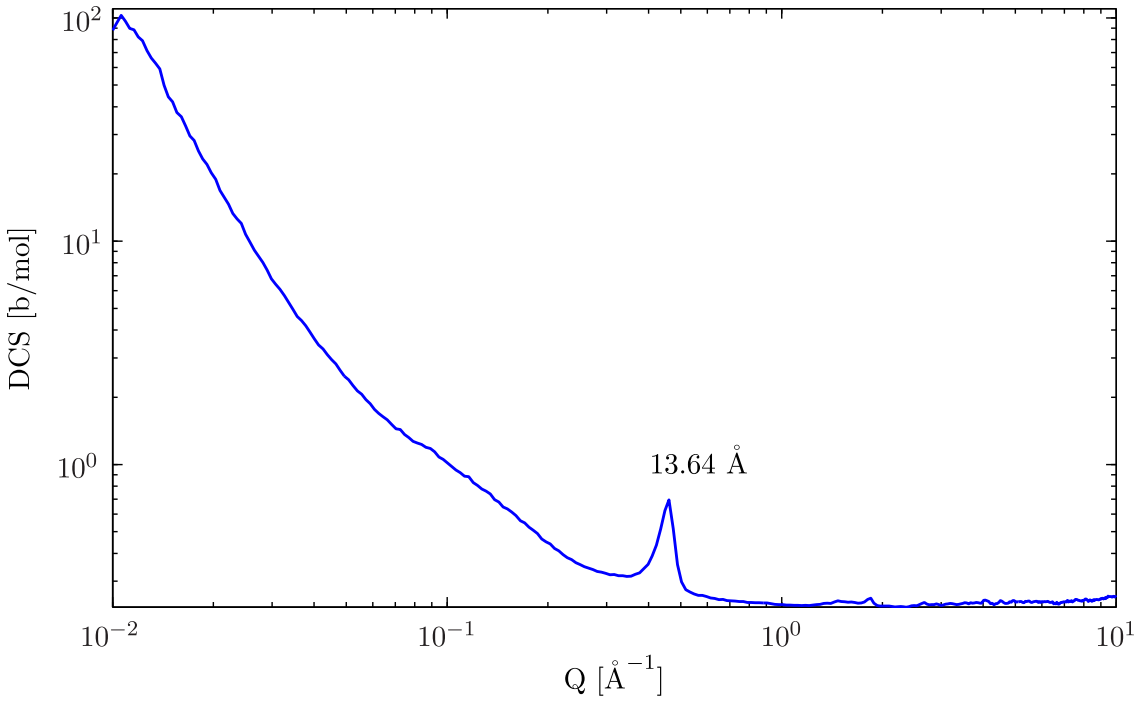


Figure 5.1: Differential cross section as a function of $Q$ for dry TMA-exchanged Eucatex vermiculite at 22°C and 50 bar. (001) peak of clay is easily identified.

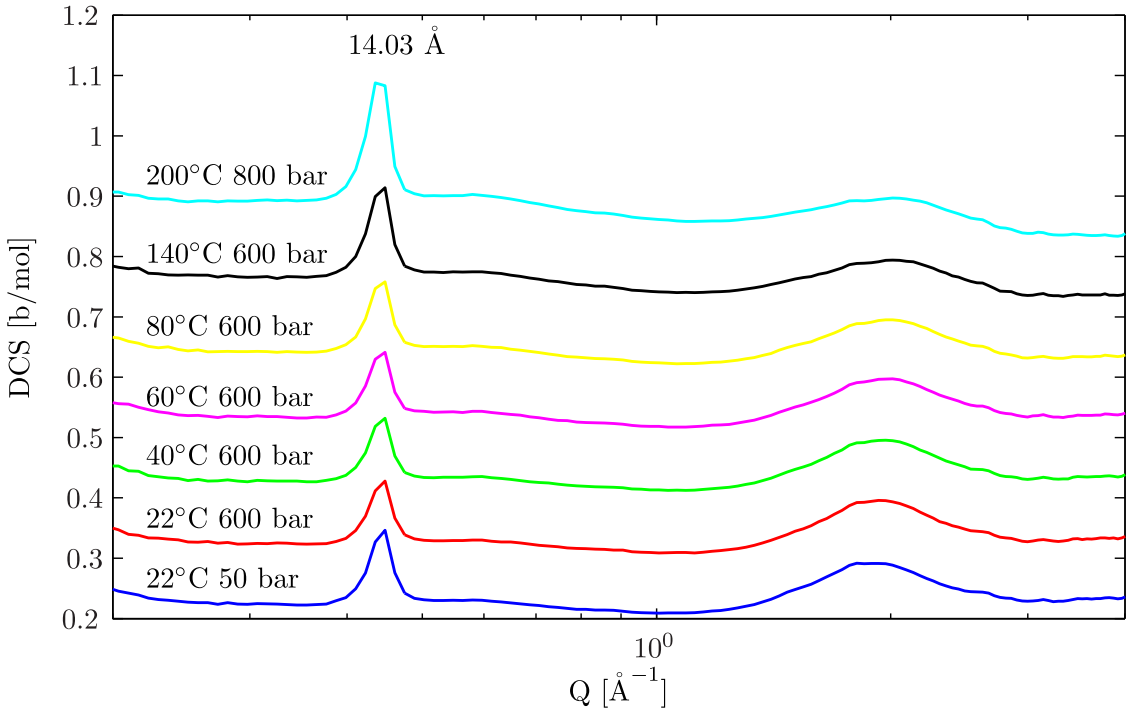


Figure 5.2: Differential cross section as a function of $Q$ for TMA-exchanged vermiculite with $D_2O$ loading and increasing hydrostatic pressure and temperature. Note no change in (001) peak after initial addition of $D_2O$ even with increasing p & T.

Figure 5.2 shows the data for the TMA-Eucatex after flooding with $D_2O$ at increasing pressures and temperatures given in Table 4.1. There is an initial increase in (001) peak distance of the clay from 13.43 Å to 14.03 Å indicating that the clay is absorbing water into the interlayer region indicating a bi-layer water hydrate[43,136] The TMA ions move from an in plane configuration to being offset from the centre to accommodate for the water[43,136] which is drawn into the interlayer as the TMA ion is hygroscopic. There is now also a peak observed at $Q = 1.889\text{Å}^{-1}$ for the presence of $D_2O$ in the system. This is not the interlayer $D_2O$ but the supernatant fluid. As the pressure and temperature is increased, the (001) peak does not move however, the $D_2O$ peak is clearly seen to shift to higher $Q$ and broaden due to the increased thermal energy to the system discussed in Chapter 4. MD simulations of the hydration energies of TMA-smectites with increasing water content[43] have been calculated as similar to bulk SPC water meaning that the clay sheets should continue expanding beyond the observed amount. The explanation for the lack of expansion of the TMA-vermiculite with increasing p & T has therefore attributed to unfavourable hydrophobic interactions with the water molecules[43]. However this seems unlikely since the TMA perturbation to the water structure is minimal (Section4.4.6) and also TMA ion is known to by hygroscopic. We do know that for vermiculites however, the TMA resides closer to the clay sheet than it does for smectites[136] due to its higher layer charge and therefore could contribute to an increase in the hydration energies of the system. Therefore we can conclude that TMA does perform as a clay swelling inhibitor, however this is for pre-exchanged and relatively pure vermiculite clay. In a real situation, the TMA would be pumped downhole and the exchange of the TMA ions with the existing charge-balancing ions needs to be taken into consideration.

## 5.2 $HMDA_{(aq)}$ Flooding of Li–Vermiculite under Burial Conditions

This section presents the results of the first investigation organic diamine in aqueous solution flooding of Li–vermiculite at elevated pressures and temperatures. Neutron diffraction has been performed on lithium-vermiculite from Flexitallic from temperatures of 22°C to 140°C combined with pressures of 1 to 800 bar with 2 molar hexamethylenediamine ($HMDA_{(aq)}$) flooding. The subsequent data has revealed that without the presence of fluid in the system, the $d$-spacing of the clay is 9.87 Å. With the addition of 2 molar HMDA

in $D_2O$, this increases to 10.07 Å signifying *no* intercalation of the HMDA. This value for the *d*-spacing remains with the application of both pressure and temperature.

In real systems, inhibitor compounds are added to the drilling fluid and subjected to subterranean pressures and temperatures. Therefore in contrast to the previous experiment, the as received clay was flooded with a 2 molar solution of the amine inhibitor molecule HMDA. It also has a long hydrophobic backbone which which we believe helps to dispel water in the interlayer region. Therefore, the following experiment was designed to investigate to what extent the HMDA exchanges and to observe the effects of pressure and temperature to the (001) peak of clay.

### 5.2.1 Sample Preparation and Experimental Methods

The NIMROD beamline at ISIS was utilised for the investigation into interlayer structure of Li-vermiculite with $HMDA_{(aq)}$ flooding under burial conditions.

The vermiculite sample used for this investigation was from Flexitallic, which is made via cation exchange in excess LiCl solution. The clay is dried and mixed with talc (a non expanding clay) left to settle before being consolidated into 0.3 mm thick sheets which can be cut to any preferred size. Although the platelets are left to settle before rolling, the particles exhibit alignment akin to that of a powder sample. Figure 5.3(a) is an SEM image of the sample showing random orientation of the platelets i.e. effectively a powder sample. Figure 5.3(b) is a macroscopic picture of the sample in its consolidated form that was put into the beam.

The consolidated vermiculite was cut into 10 x 28 mm pieces in order to fit into the high pressure sample can used in the previous two experiments. The cut clay wafers were deuterated by leaving in a sealed chamber with a pot of $D_2O$. The $D_2O$ was changed daily for 5 days. A full elemental analysis of the vermiculite used in this experiment was attempted but due to the "naturalness" of the clay i.e. not purified, it was not possible to give a perfect atomic composition of the clay. The closest analogue, in terms of the structural elements is the Brazilian Eucatex. We therefore use this as the elemental composition but with lithium as the counterion:

$$Si_{6.30}Mg_{5.44}Al_{1.65}Fe_{0.6}O_{20}(OH)_4 \bullet 1.3Li^+ \bullet 4H_2O \tag{5.2}$$

X-ray diffraction (XRD) was performed at ambient conditions on the consolidated

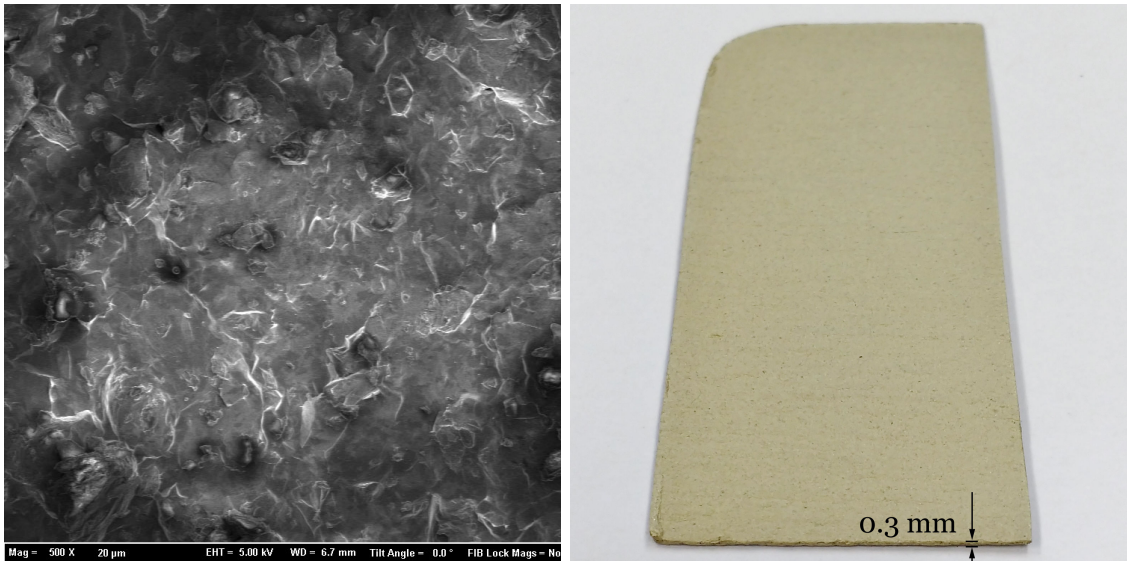


(a) (b)

Figure 5.3: **(a)** SEM of the consolidated vermiculite used in the experiment; Image obtained by Yuji Suzuki. Note the lack of alignment of clay quasi-crystals and powder nature of the sample. **(b)** picture of the consolidated clay put into the beam.

vermiculite samples along with the pure talc XRD shown in Figure 5.4.

The (001) and (003) peaks from the talc and the expandable part of the remaining material i.e the vermiculite *d*-spacing are denoted on the graph. Under ambient conditions and in the presence of air, we measure the *d*-spacing of the vermiculite to be $\sim 11$ Å. The talc peaks are also seen to shift minutely to lower $Q$ in the consolidated mixture. The vermiculite-talc wafers were placed in the vacuum oven for 12 hours at 80°C so that it could be loaded dry into the TiZr null-scattering sample can. The sample can was filled so that the clay had room to expand if needed, which allowed for 10 wafers to fit comfortably inside the can.

The test fluid used was a $\sim 2$ molar HMDA in $D_2O$, therefore a ratio of 1:28 HMDA:$D_2O$. The HMDA at 98% purity, was obtained from Sigma Aldrich. Three distinct isotopes were used to flood the clay according to Table 4.4: (1) fully hydrogenated HMDA, $C_6\mathbf{H}_{12}(N\mathbf{H}_2)_2$ in $D_2O$, (2) D4-HMDA - $C_6H_8\mathbf{D}_4(NH_2)_2$ in $D_2O$, (3) 50:50 mix $C_6\mathbf{H}_{12}/C_6H_8\mathbf{D}_4(NH_2)_2$ in $D_2O$ with the idea in mind that the location of the HMDA would be able to be determined as it intercalated into the clay. However due to the large volume of sample required for the experiment, the inelastic scattering from the fully hydrogenated and 50:50 mix samples was very large and swamped the low-$Q$ data which we were interested in and therefore are not considered in the rest of the analysis. The focus is therefore on the deuterated isotope

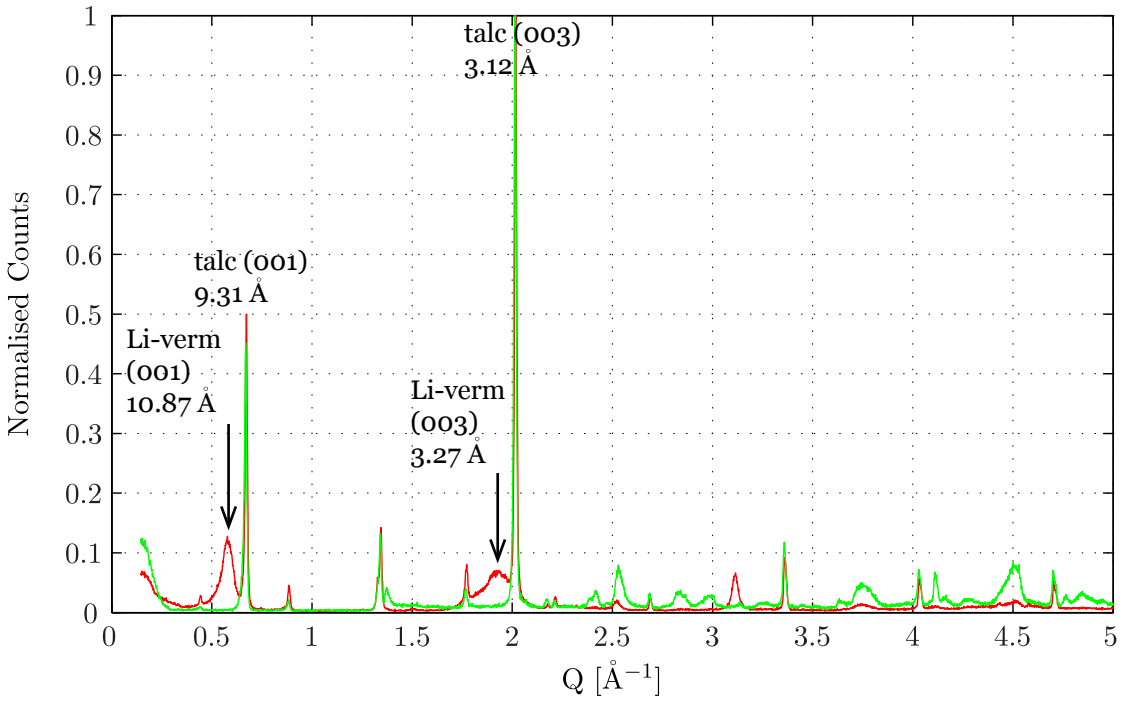


Figure 5.4: X-ray diffraction pattern of powder sample at ambient pressures and temperatures of — talc and the — Li-vermiculite, talc mixture (Li-verm) from Flexitallic.

| Depth (km) | Temperature (K) | Pressure (bar) |
|---|---|---|
| 0 | 22 | 1 |
| 2 | 80 | 300 |
| 4 | 140 | 600 |

Table 5.2: Pressure and temperature combinations for each measurement for HMDA $_{(aq)}$ of Li-vermiculite.

of the HMDA.

Data was first collected on the dry sample. The system was then flooded with with 2 molar D4-$HMDA_{(aq)}$ at 140°C and 600 bar pressure and data collected for 3 hours. The pressure and temperature was successively decreased to each p & T combination given in Table 5.2 and data collected for 3 hours at each point.

Data treatment is the same for the liquid diffraction data collected on $TMA_{(aq)}$ described in Section 4.3. For the clay-fluid data at ambient, since we have neutron data for the same fluid composition also at ambient (from Section 4.5), a direct subtraction of the HMDA solution from the clay-fluid system can be performed such that the only clay data remains. For the subsequent clay-fluid data at higher pressures and temperatures, a comparison between the differenctial cross section (DCS) will need to be made.

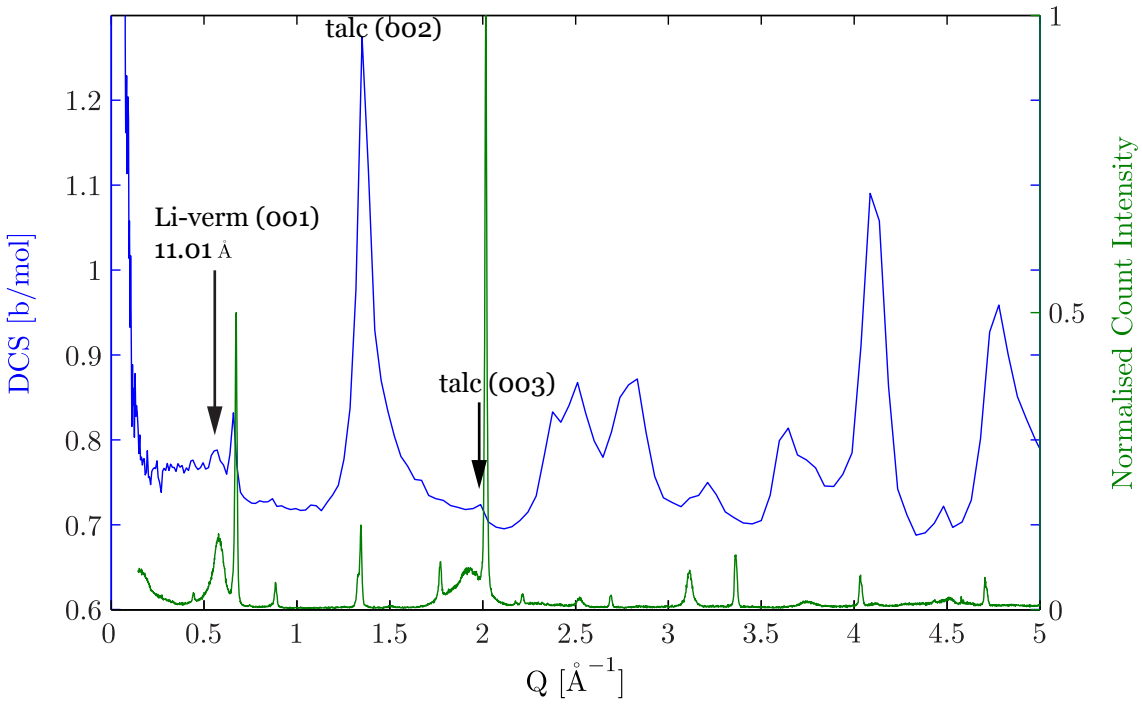


Figure 5.5: Neutron differential cross-section for the dry deuterated consolidated Li-vermiculite before flooding with inhibitor solution alongside the normalised count XRD intensity of the hydrogenated analogue. Arrows denote peaks in the neutron data. — neutron, — X-ray.

### 5.2.2 Results and Discussion

#### Dry Li-vermiculite

Figure 5.5 shows the neutron differential cross section for the dry deuterated consolidated Li-vermiculite before flooding with inhibitor solution alongside the normalised count XRD intensity of the hydrogenated analogue. Since the sample at the microscopic scale, is a powder, the $c$-axis cannot be aligned with the beam and therefore we observe scattering from the clay sheets as well as from the (001).

The intensities of the peaks from neutron to X-ray vary according to the scattering cross section of the element and the electronic density respectively for each technique. Therefore, we do not expect the same intensities. However since we are looking for the Bragg scattering from the (001) peak of the clay, the Bragg peak positions should match from neutron to X-ray diffraction pattern. Using the talc (00$l$) peaks as a marker, we do see these peaks line up however there is a small shift of 0.015 Å$^{-1}$ to higher $Q$ of the XRD pattern. Since this shift is seen across all the peaks, it is accepted to be due to the sample being very slightly misaligned in the beam when taking the XRD data. The value of the

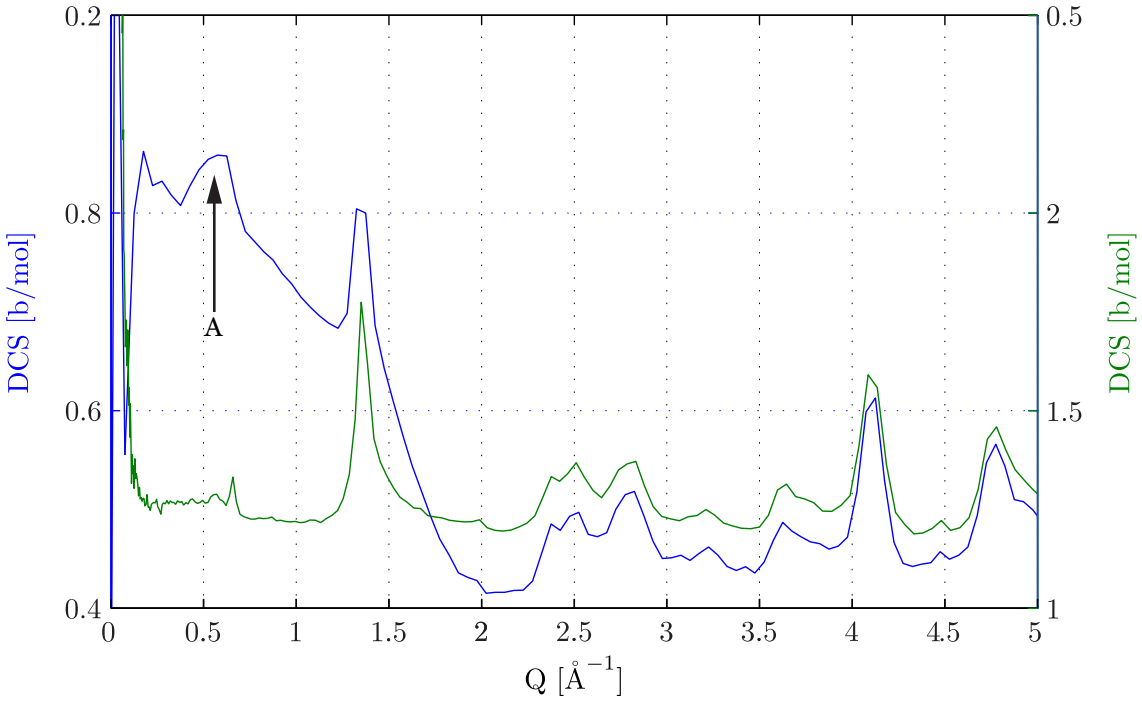


Figure 5.6: Neutron differential cross-section for the dry deuterated consolidated Li-vermiculite before and after flooding with deuterated inhibitor solution. — dry Li-vermiculite, — D4-HMDA flooded vermiculite with the D4-HMDA fluid removed from the data. Note broad clay (001) at A.

*d*-spacing measured by neutron diffraction is $\sim$ 11 Å.

#### 2M D4-$HMDA_{(aq)}$ Flooding of Li-Vermiculite

Figure 5.6 shows the neutron DCS from the dry Li-vermiculite and the subsequent DCS after flooding with 2M D4-HMDA in $D_2O$. The data for the clay-fluid system has the supernatant D4-HMDA solution subtracted as a background leaving just the contribution from the clay and any interlayer fluid. The talc peaks remain unshifted, however we can see a broad peak at 'A' which combines the clay (001) and the talc (001). The lack of scattering from the interlayer could be due to there being little intercalation of the HMDA in this region or the inelastic scattering overwhelming the small clay (001) and (003).

Figure 5.7 shows the neutron DCS for the clay-HMDA fluid system with increasing pressure and temperature. It combines the scattering from the supernatant D4-$HMDA_{(aq)}$ and the Li-vermiculite. Looking at 'B' we observe a decrease in the $D_2O$ peak, possibly due to the broadening of distances between molecules as temperature is increased. Looking at 'A', the (001) of the clay is not discernable from the data.

We therefore performed XRD on the sample, post experiment with the data for this

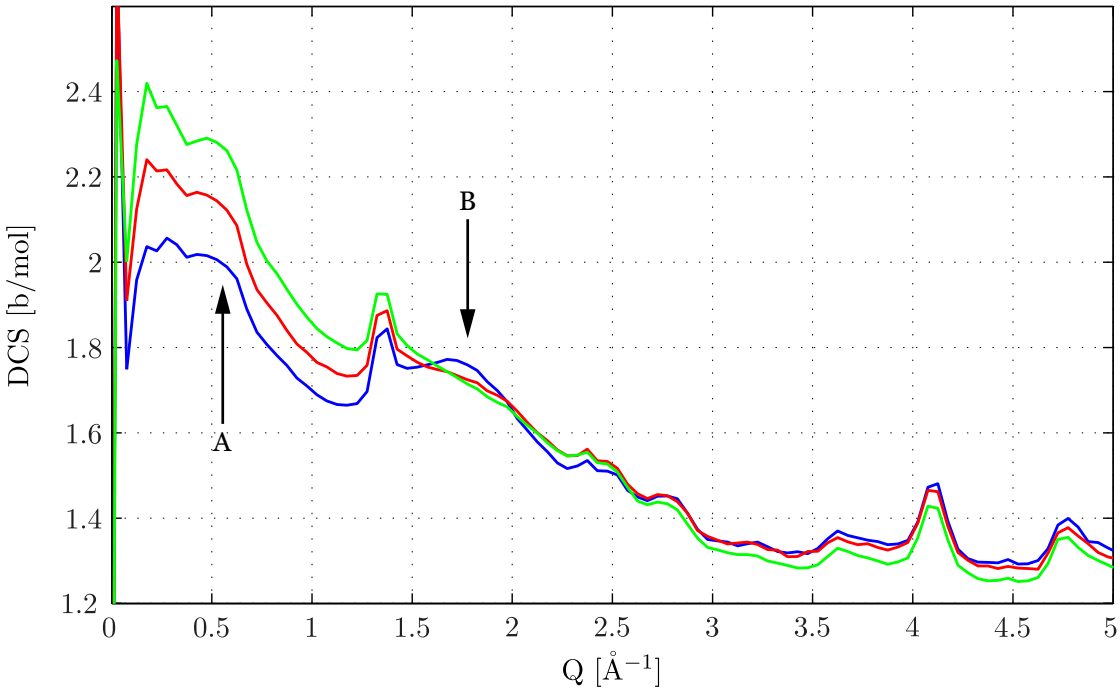


Figure 5.7: Neutron differential cross-section of the clay-fluid system at — 22°C 1 bar, — 80°C 300 bar and — 140°C 600 bar.

shown in Figure 5.8.

The (001) peak for the vermiculite is very much suppressed. The analysis of the XRD is therefore focussed on the (003) peak variation.

Figure 5.9(a) shows the change to the talc (003) peak before and after the experiment. From pure talc to consolidated in the vermiculite/talc mixture, the peak shifts to higher $Q$ by 0.3% and again by another 0.3% from as received to post experiment. This is a systematic shift across all the talc peaks and therefore attributed to misalignment of the sample in the beam and can be considered the error on the values measured for the $d$-spacing of the clay.

Figure 5.9(b) shows the (003) reflection for the pre and post experiment Li-vermiculite/talc mixture. A broad peak with maximum at $Q \approx 1.91\text{Å}^{-1}$ is measured for the as received clay. The XRD data set for the vermiculite post neutron experiment shows a more intense and sharper (003) with a shift to lower $Q \approx 1.87\text{Å}^{-1}$ indicating an expansion of the $d$-spacing of the clay form 9.87 Å to 10.08 Å. This can be attributed to the inclusion of a layer of water in the interlayer since cation exchange of the lithium for HMDA should incur a larger increase in the (003). We can also infer that there is no intercalation of HMDA into the clay since MD simulations by Suter *et al*[43] which show that there the

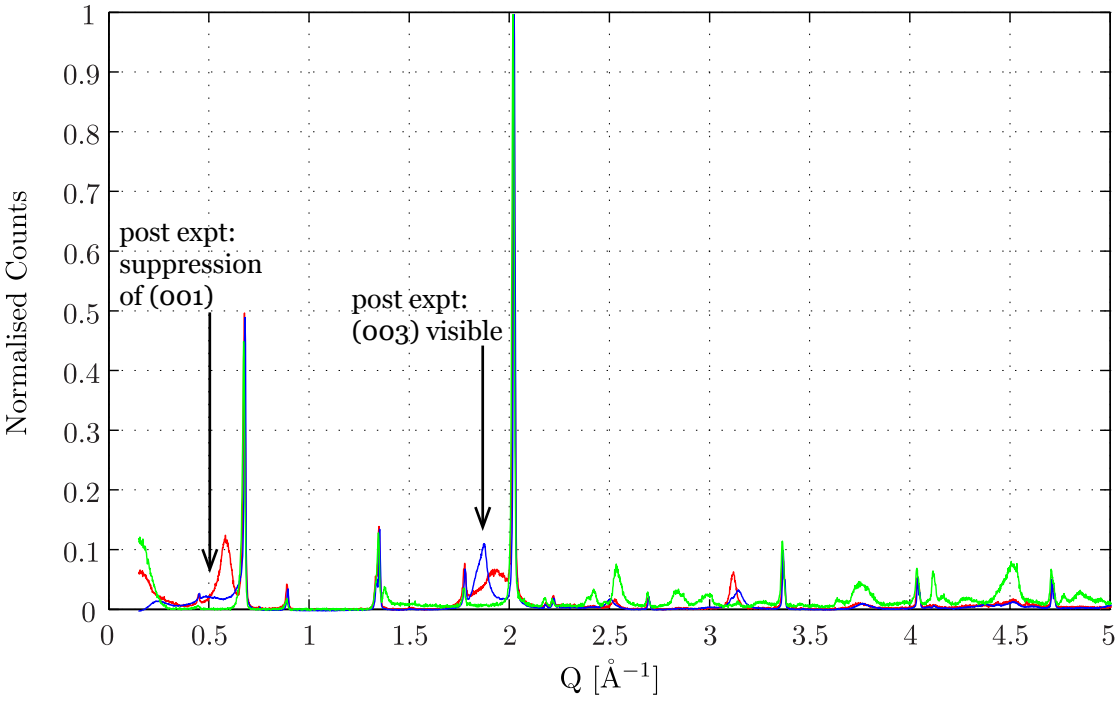


Figure 5.8: X-ray diffraction pattern of powder sample at ambient pressures and temperatures of — talc, — as received Li-vermiculite & talc mixture, — Li-vermiculite post HMDA flooding and application of pressure and temperature. Shift of (003) to lower $Q$ indicating expansion of interlayer region and suppression of (001).

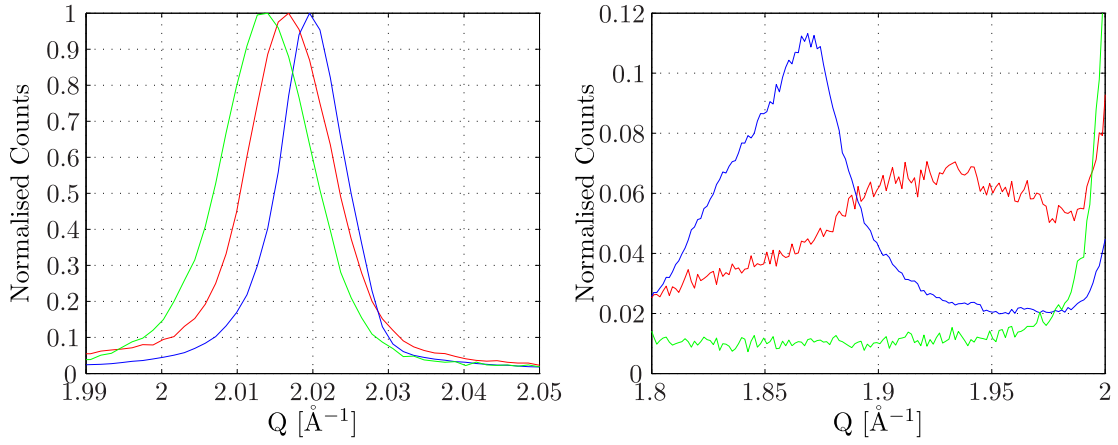


Figure 5.9: XRD of — as received Li-vermiculite & talc mixture, — Li-vermiculite post HMDA flooding and application of pressure and temperature and — pure talc, for **(a)** talc and **(b)** (003) the vermiculite (003) peak .

$d$-spacing of dehydrated HMDA intercalated smectite is 13.0 Å and with addition of water, should increase to 15.2 Å.

However, when the sample was removed from the sample can, post experiment there was no exfoliation of the clay sheets and it was entirely intact and firm. Previously, in the presence of water, we had observed full exfoliation of the sheets within minutes. This indicates that there is no excessive intercalation of water into the interlayer region. We therefore postulate that the HMDA is on the surfaces of the clay. Any further intercalation of water into the interlayer would mean unfavourable interactions of the water molecules with the hydrophobic backbone[43] thereby hindering access of water to the interlayer region. This is also supported by the sharpening of the (003) peak. The lack of pore spaces for the HMDA to travel through due to the consolidation of the vermiculite wafers, may also contribute to the lack of exchange observed.

We therefore conclude that rather than stopping clay swelling via exchange of HMDA with interlayer cations, flooding of 2M $HMDA_{(aq)}$ acts to hinder the swelling process by sealing the interlayer regions from water and that this is robust against the application of pressure and temperature.

## 5.3 Porosity of Compacted Bentonite – A SE-SANS Investigation

This section presents the results of the first spin-echo small angle neutron scattering experiment designed to investigate the change to the porosity of compacted bentonite samples with the addition of water and brine at seawater concentration ($\sim$ 2.02 molar $NaCl_{(aq)}$). The overall outcome of the experiment was the observation that the larger pores of the compacted bentonite filled before the smaller ones.

Up to this point, we have investigated the behaviour of the interlayer in the presence of clay swelling inhibitors. We have observed that there is no bulk expansion of the interlayer in the presence of the inhibitors TMA and HMDA. However the oilfield standard test of inhibitor success is not to measure the interlayer expansion but the uniaxial expansion of compacted clay samples in the presence of varying swelling inhibitor solutions. As will be described in Chapter 7, we observe uniaxial expansion of compacted clay samples in the presence of clay swelling inhibitors. However, when the $d$-spacing of these samples was monitored with fluid invasion under pressure and temperature, Sec 5.1 & 5.2, no

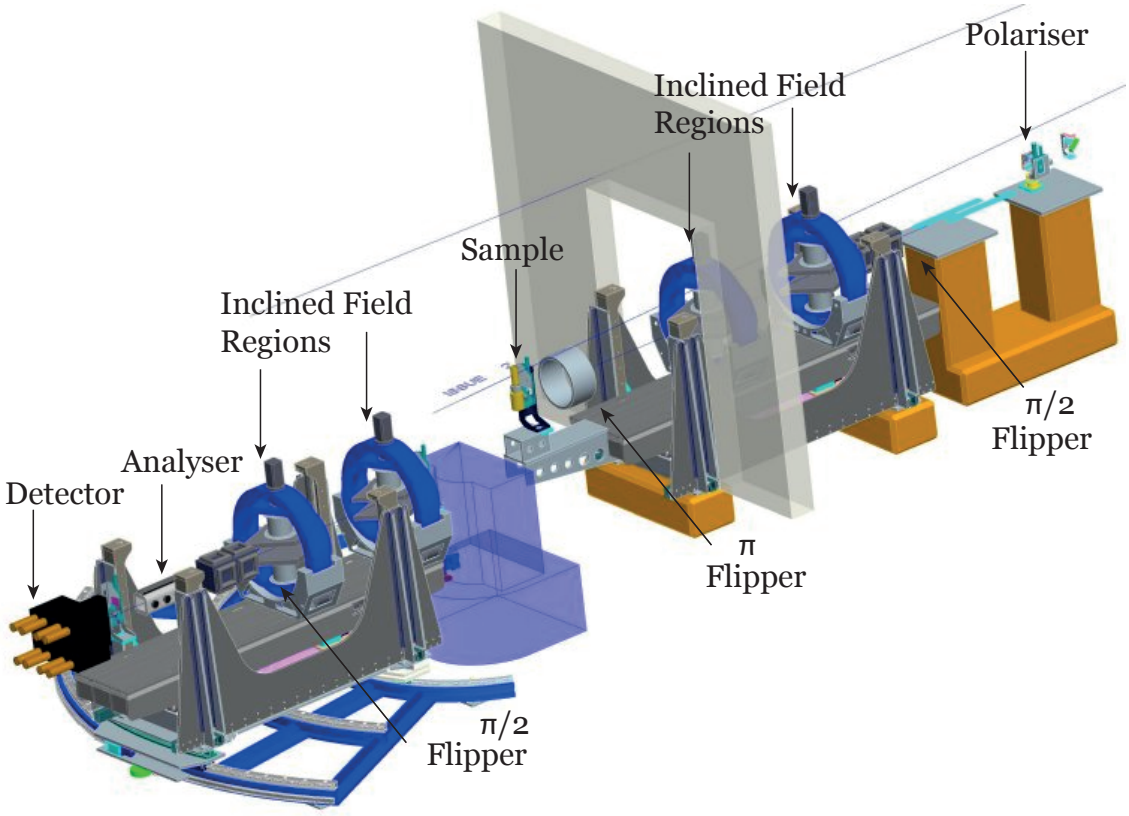


Figure 5.10: Sketch of the OffSpec[5] instrument detailing the important features of the beam line.

expansion of the *d*-spacing was observed. The expansion in the compacted samples was thus attributed to the capillary forces present due to the introduction of air into macro and meso-pores within the sample during compaction. Despite these points, the method of measuring the uniaxial swelling of compacted, naturally occurring clay is still used as an oil-industry standard for testing the swelling response of the clay. It is clear that the compaction method alone cannot provide the whole story of the swelling clays. We therefore proposed a SE-SANS study to obtain time resolved observations of the variation to the pore distribution of compacted clay samples within the first hour of submersion in various test fluids, to determine the route of the fluid into these oil-field standard materials. Since this investigation was the first time compacted clays had been studied using the SE-SANS method, it must be pointed out that this is very much a proof of concept study.

### 5.3.1 Methodology

#### OffSpec Instrument

The OffSpec[138] instrument at ISIS was used for this spin-echo investigation. It utilises the neutron spin at low incident angles to allow for a continuous length scale from 0.01 – 30 $\mu m$ to be probed, as well as being able to exploit the difference in total neutron scattering length of hydrogen and deuterium in the experiment. It also allows for a higher flux beam since the neutrons do not require a specific $\lambda$. Alongside these advantages, the measured parameter is the polarisation of the scattered beam which is directly related to the real-space autocorrelation function ($G$) as opposed to ($S$), the reciprocal space correlation function. I.e. the data received is output as a function of the real-space distance of the scattered objects. A sketch of the instrument is shown in Figure 5.10 with the key features labelled.

#### Sample Preparation

The investigation here was performed on compacted bentonite. The bentonite used is the SWy-1 from CMS with general formula:

$$(Ca_{0.12}Na_{0.32}K_{0.05})[Al_{3.01}Fe^{(III)}_{0.41}Mn_{0.01}Mg_{0.54}Ti_{0.02}][Si_{7.98}Al_{0.02}]O_{20}(OH)_4 \quad (5.3)$$

0.75 g of bentonite clay was used for making the compacted disks in a die and hydraulic press with the application of 20,00psi ($\sim$ 10 Tonnes) pressure. Since the clay scattered very strongly, the amount of clay in the beam had to be kept to a minimum and 0.75 g was the lower limit on the amount of clay that would still hold together when taken out of the die. To minimise scattering from clay due to large incoherent scattering length of hydrogen, samples were deuterated by placing the compacted clay disks in a sealed 100% $D_2O$ humidity atmosphere with the $D_2O$ source changed daily for 5 days. Prior to loading in the beam, the clay disks were baked in a vacuum oven at 80°C for 6 hours and the mass and thickness recorded.

The final experimental procedure was as follows:

The clay disks were placed in sealed Hellma cans and aligned such that the flat face of the disk was normal to the incident beam direction. A scan of the baked deuterated clay was taken. 0.5 g of $D_2O$ was added to the bottom of the Hellma sample can and left to equilibrate overnight, Figure 5.11(a). 5 minute long scans were taken during this

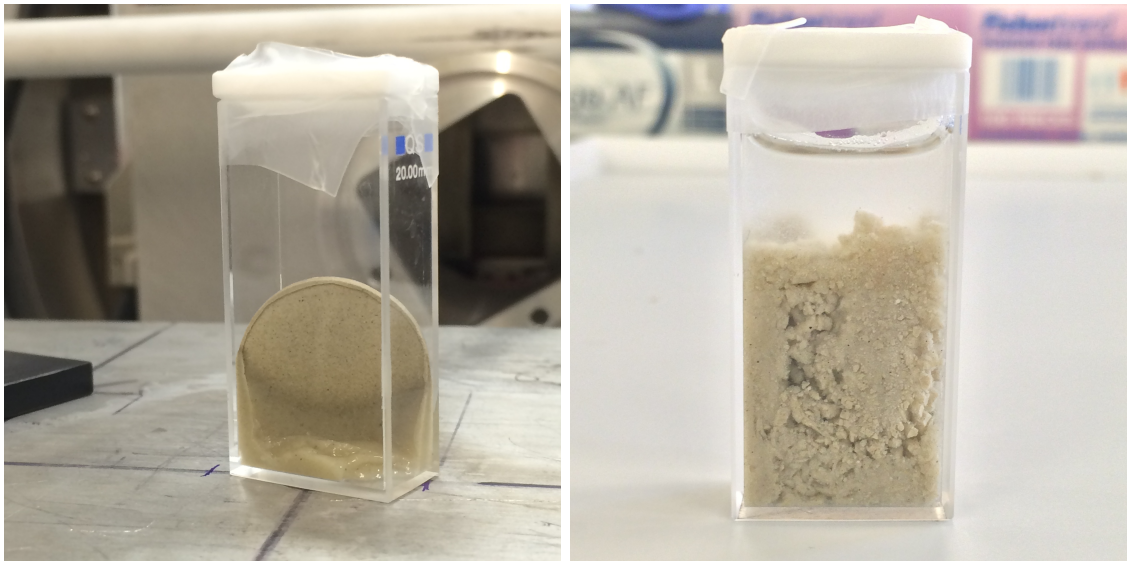

(a) (b)

Figure 5.11: Sample environment including the **(a)**Hellma can containing sample equilibrated with $D_2O$. **(b)** Sample fully dispersed in brine at the end of the experiment. Contrast in **(a)** is between the air in the pores and the deuterated clay. Contrast in **(b)** is between the air in the pores and the deuterated solution as the liquid fills the pores and finally system becomes a dispersion.

time so that the equilibration of the sample and fluid could be monitored. The sample was then fully immersed in brine and again, 5 minute long scans were taken for 2 hours to capture the initial hydration of the material. The final state of the system is shown in Figure 5.11(b).

**Data Treatment**

The measured polarisation of the sample $P_{sample}$ is a function of the spin-echo length $r$ and therefore becomes $P(r)$. A measurement of the empty beam $P_0$ is taken and then the normalised polarisation ($P_{sample}/P_{emptybeam}$) is related to a form of the one-dimensional real-space autocorrelation function ($G$) through:

$$\frac{P(r)}{P_0} = \mathrm{e}^{\sigma t(G(r)-1)} \tag{5.4}$$

$\sigma$ and $t$ are the attenuation coefficient and thickness of the sample respectively. We can therefore plot $\frac{P(r)}{P_0}$ against $r$ and look at the variation in $r$ with time.

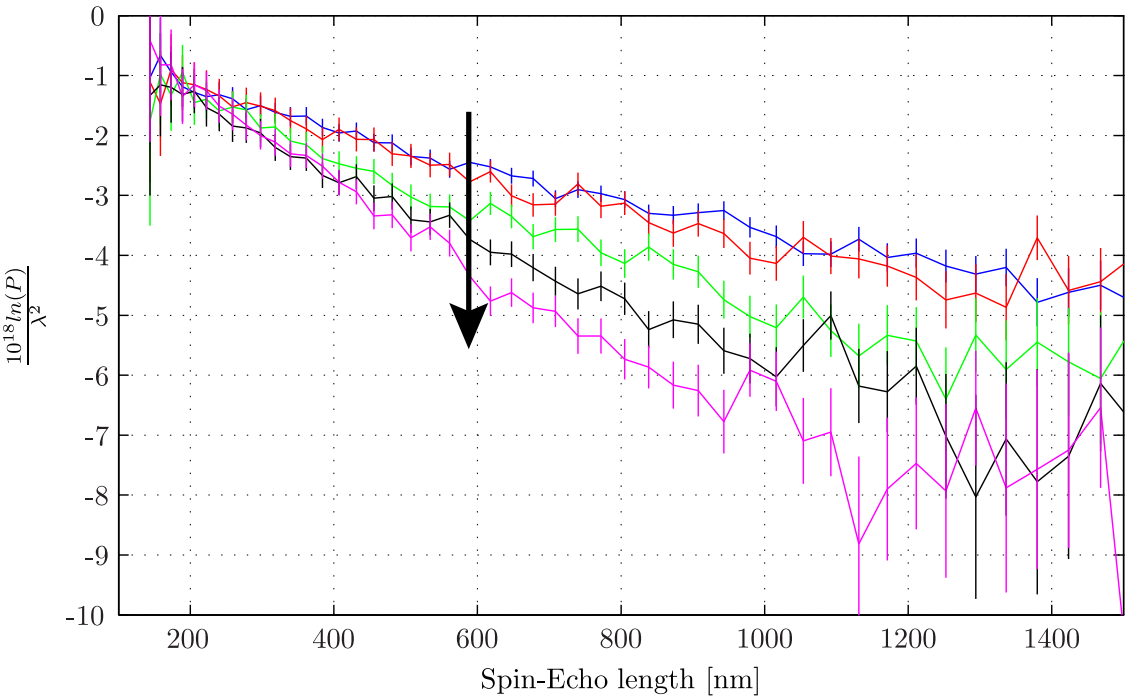


Figure 5.12: Spin-echo micrograph showing depolarisation according to 0.5 g $D_2O$ absorbtion into compacted bentonite disk. Each set of data points is taken at a time after $D_2O$ loading and the arrow denotes the direction of time. Vertical lines denote error bars. — dry deuterium exchanged compacted bentonite, — 10 mins, — 30 mins, — 60 mins, — 4 hrs.

### 5.3.2 Results and Discussion

Although the range of the instrument allows investigations to probe length scales from 10 nm to 30 $\mu m$, since the sample scattered very strongly in the beam, we were not able to obtain data below $\sim$ 150 nm or above $\sim$ 1.5 $\mu$m.

Figure 5.12 is a spin-echo micrograph showing the depolarisation of the beam as a function of spin-echo length (size of scattering object) as the sample is equilibrating to the 0.5 g $D_2O$ at the bottom of the sample can. Each set of data points is taken at some time after the addition of the $D_2O$ denoted in the caption. The depolarisation of the incoming beam is a function of the normalised beam $\frac{P_r}{P_0} = P$. The arrows on the plot show the direction of time after adding the drop.

For the dry clay run, there are no discontinuities in the data implying a continuous distribution of scattering objects which are not of any particular shape, i.e. spherical, rod etc. When a drop of $D_2O$ is added to the base of the sample cell, the clay absorbs the water into the pore spaces. There is now a higher contrast in these pore spaces since they are filled with $D_2O$ instead of air and the beam depolarises in these regions. This is

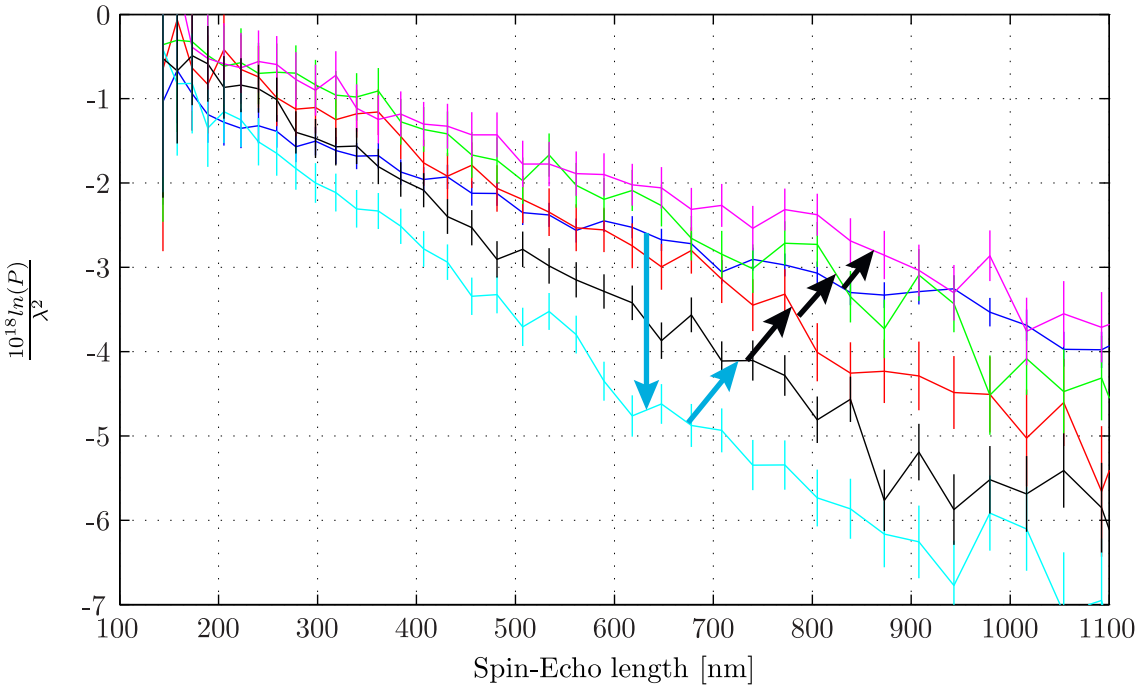


Figure 5.13: Spin-echo micrograph showing depolarisation for $D_2O$ equilibrated compacted bentonite disk, fully immersed in brine. Blue arrows represent direction of time as clay equilibrates with the initial 0.5 g $D_2O$ addition. Black arrows represent direction of time after adding brine. Vertical lines denote error bars. — dry deuterium exchanged compacted bentonite, — 4 hrs after $D_2O$, — 8 hrs after $D_2O$, — 5 mins after brine immersion, — 10 mins after brine, — 1 hr after brine

observed in Figure 5.12 to occur for spin-echo lengths of >300 nm, i.e. the larger pores are filling. This behaviour is continuous across the resolution window up to 1500 $\mu m$, however at very low $r$ ≤200 nm, we see that scattering objects of this size are relatively unaffected in the 1st hour of equilibrating with the $D_2O$. We also observe that as we go from a fairly uniform sample (dry) to having equilibrated in $D_2O$, the error on the data also increases as the pores become less well defined.

After full equilibration with the initial $D_2O$, the sample is immersed in brine of seawater concentration (2.02 molar $NaCl_{(aq)}$) and again, measurements are taken every 5 mins thereafter. Figure 5.13 shows the data for the initial equilibration with the $D_2O$ at 4 hours and 8 hours after having added the $D_2O$ and also the full response of the clay to the brine solution. The direction of time after having added the $D_2O$ is shown with blue arrows. The direction of time after having added the brine is shown with black arrows. Brine is then flooded into the system and the beam depolarisation very quickly decreases at large $r$ (shown by black arrows). This is believed to be due to the pore matrix filling with brine and therefore the clay platelets are no longer held together with a definite pore

distribution. There is also a loss of contrast as the air from the clay leaves the system and the clay forms a suspension in the brine.

## 5.4 Summary

This chapter presents the results for the investigations into the crystalline swelling of TMA-vermiculite and Li-vermiculite in the presence of $D_2O$ and 2 molar HMDA solution at increasing pressures and temperatures. For both the clays we saw an initial expansion of the *d*-spacing with introduction of water into the system to a probable 2-water layers however no further swelling was observed. For the TMA-vermiculite, this is attributed to the enthalpy of hydration of the ion. For the Li-vermiculite, we do not observe exchange of lithium with HMDA since we do not observe a large enough *d*-spacing increase but argue that the HMDA sits on the surfaces of the clay sheets. The hydrophobic backbone renders interaction with the water unfavourable and therefore acts as a barrier for the water entering the clay.

Also presented in this chapter are the results of a "proof of concept" spin-echo small angle neutron scattering experiment designed to investigate the change to the porosity of compacted bentonite samples with the addition of water and brine at seawater concentration ($\sim$ 2.02 molar $NaCl_{(aq)}$). The overall outcome of the experiment was the observation that during the initial stages of hydration, the larger pores, $\sim$1 $\mu$m, of the compacted bentonite filled before the smaller pores, <300 nm.

# Chapter 6

# Diffusive Motion of Water in Terephthalate-LDH using QENS

This study focuses on diffusive motion of water molecules in terephthalate (TA) intercalated into $\frac{Mg}{Al} = 5.7$ layered double hydroxides (LDHs). LDHs have a layered structure similar to that of 1 : 1 clays. The difference here with other clay minerals is that the overall interlayer charge is positive and thus negative charge-balancing compounds exist within the interlayer region. The TA ion is most often used as a pillar compound, facilitating the insertion of bulkier anions however it has a comparative size to many mid-length chain amines which are used downhole as swelling inhibitors making it a useful system to study.

Two LDH-TA with varying amounts of water in the interlayer were investigated and the temperature range analysed was between 5 to 320 K. The first sample had a ratio of 1:16.24 TA:$H_2O$ and the second sample had 1:7.88 TA:$H_2O$. It was not possible to resolve the motion of the TA which we believe to be because it was outside of the resolution of the instrument however the motion of the water was observed. Two different jump diffusion models were used to describe the translational motion of the water: the Singwi-Sjölander (exponential jump length distribution), the Hall-Ross(Gaussian jump length distribution) and Fickian diffusion has been calculated for each sample exhibiting translational diffusion. The motion of the water was found to be heavily dependent on ratio of TA:$H_2O$ in the interlayer since the amount of water governed the interlayer expansion and therefore the mobility of the water molecules. Consequently, translational motion was only observed

for the 1:16.24 TA:$H_2O$. From 0 to 260 K no motion was observed; at 260 K only rotation of the water molecules and full translation according to the Singwi-Sjölander model with $D_{trans}$ and $\tau_t$ of $3.4\times10^{-9}$ $m^2s^{-1}$ and 6.60 ps at 280 K and $6.0\times10^{-9}$ $m^2s^{-1}$ and 3.15 ps respectively at 320 K.

Previous diffusion studies of LDH-TA compounds have focussed on the motion of the water within the $\frac{Mg}{Al} = 2$ compound[139], therefore a TA:$H_2O$ ratio of 1:4. This was in the temperature range of 323 to 423 K (0 to 150°) using neutron spectroscopy. $D_{eff}$ at these temperature limits was calculated to be 2.47 and 4.60 $\times10^{-7}$ $m^2s^{-1}$ respectively, increasing with temperature. This is two orders of magnitude higher than that observed for bulk water[10]: 2.5 $\times10^{-9}$ $m^2s^{-1}$ and therefore unsure of the reliability of the values.

## 6.1 Spectroscopy on the IRIS Instrument

Spectroscopy measurements were made using the high-resolution spectrometer, IRIS, the important features of which are shown in Figure 6.1. The dynamic scattering function $S(Q,\omega)$ was measured using the 002 reflection of pyrolytic graphite within an inverted geometry (back-scattering) regime. With this analyser and an incident neutron wavelength of 6.6 Å, IRIS has a FWHM energy resolution of 17.5 $\mu$eV, with a total energy window of $\pm$ 0.5 meV[140]. The time resolution of IRIS is $10^{-10} - 10^{-12}$ ps and it also has long diffraction capabilities allowing for simultaneous measurement of $d$-spacing of samples. IRIS also allows for insertion devices, in this case a closed cycle cryo-cooler (CCR) to be used for cooling of samples.

#### Time-of-Flight

IRIS uses back-scattering, time-of-flight (TOF) method to measure the change in energy of the scattered neutrons. The TOF design uses short flight paths to determine the velocity, and therefore the energy of the thermal neutrons. TOF refers to the time taken for the neutron to travel from entering the flight path of the instrument to arriving at one of its detectors and can be achieved by fixing either the incident wave-vector, $\vec{k}_0$ (direct) or scattered wave-vector, $\vec{k}_1$ (indirect or back-scatter).

The back-scatter IRIS spectrometer, measures $\vec{k}_0$ and fixes $\vec{k}_1$. This regime allows for a single crystal analyser with Bragg angles close to $\frac{\pi}{2}$, in this case pyrolytic graphite, to be used to monochromate the incident beam and thus reflecting specific $\vec{k}_1$ onto the

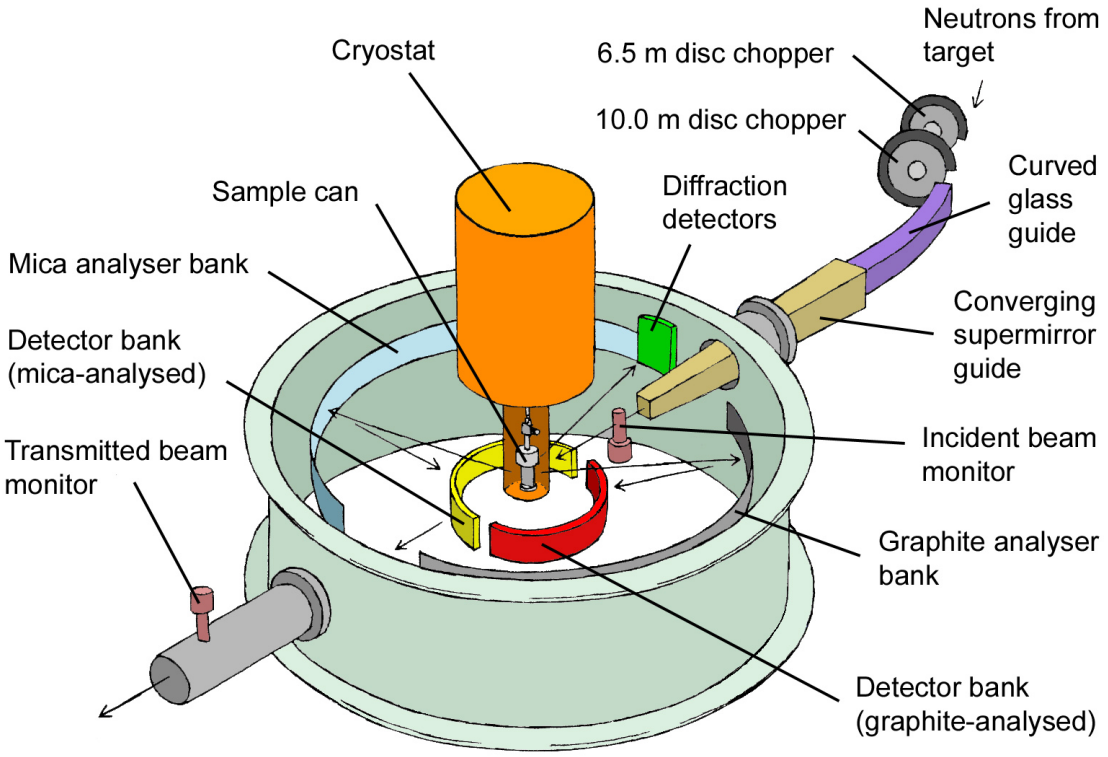


Figure 6.1: Schematic representation of the IRIS back-scattering TOF spectrometer at RAL[6].

detectors. The back-scattering geometry is preferable since high resolution ($\sim 1\mu$eV) is attainable and the neutron energy-loss region of $S(\vec{Q},\omega)$ for cold samples is accessible in this configuration.

## 6.2 IRIS Sample Environment and Experimental Methods

Similarly to the vermiculites exchanged with the TMA ion, here, terephthalate ions have been exchanged with the pre-existing carbonate anions of the LDHs which have been prepared with varying proportions of Mg and Al substitutions. They were synthesized via the technique of co-precipitation by Greenwell[141] *et al.* The product of the synthesis placed the Mg/Al ratio = 5.7 for the materials used in this investigation and the interlayer water content at laboratory humidity at 8.4%. This was verified by TGA measurements, Figure 6.2, performed at UCL on the same sample after drying in the oven at 80°C for 24 hrs and then leaving to re-hydrate in air for 24 hrs at room temperature and humidity. The measured mass loss was $\sim$ 9.4% and therefore in good agreement with the quoted

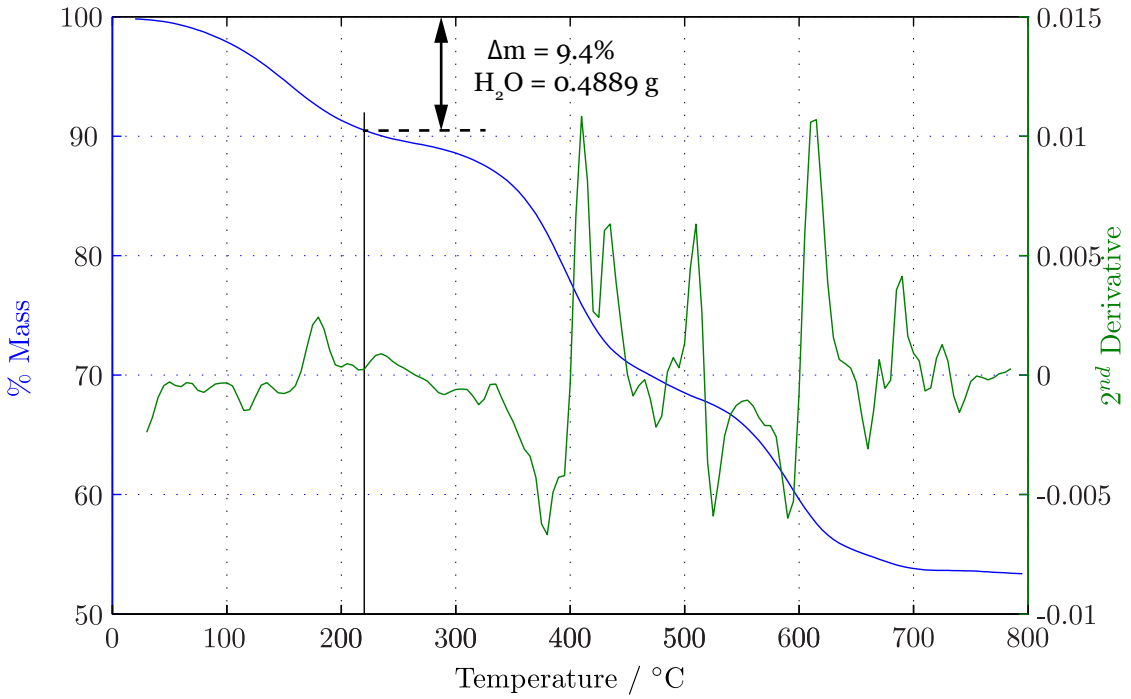


Figure 6.2: TGA curve and its $2^{nd}$ order derivative of LDH-TA with $\frac{Mg}{Al} = 5.7$. The initial mass loss is associated with the loss of interlayer water. Applied heating rate was 10°C/min.

amount.

At laboratory humidity, and therefore a water content of 8.4% by mass, the sample has atomic formula:

$$[Mg_{5.7}Al(OH)_{13.3}]^{1+}[(C_6H_4(CO_2)_2)_{0.5} \bullet 2.4H_2O]^{1-} \tag{6.1}$$

where the TA is: $[C_6H_4(CO_2)_2]^{2-}$ and the number of water molecules per TA is 4.2. A $d$-spacing of 3.46 Å for the LDH at laboratory humidities implies that the TA are lying horizontal in the interlayer. These samples were deuterated by successive drying in a vacuum oven at 100°C for 12 hours and then placing in 100% $D_2O$ humidity for 24 hours in order to exchange the $H_2O$ in the LDH with $D_2O$. The process was repeated 3 times. Since no observable scattering from the hydrogenated TA was measured within the deuterated LDH, we switched to using hydrogenated LDH samples with $H_2O$ to increase the scattering from the system. Additionally, we believed that with an interlayer of 3.6 Å, there may not be enough room for motion of the water and TA to occur, so we inserted additional $H_2O$ molecules to the hydrogenated LDH.

Thus, two samples were prepared: (a) hydrogenated-LDH-TA + 20% $H_2O$ (b) hydrogenated-

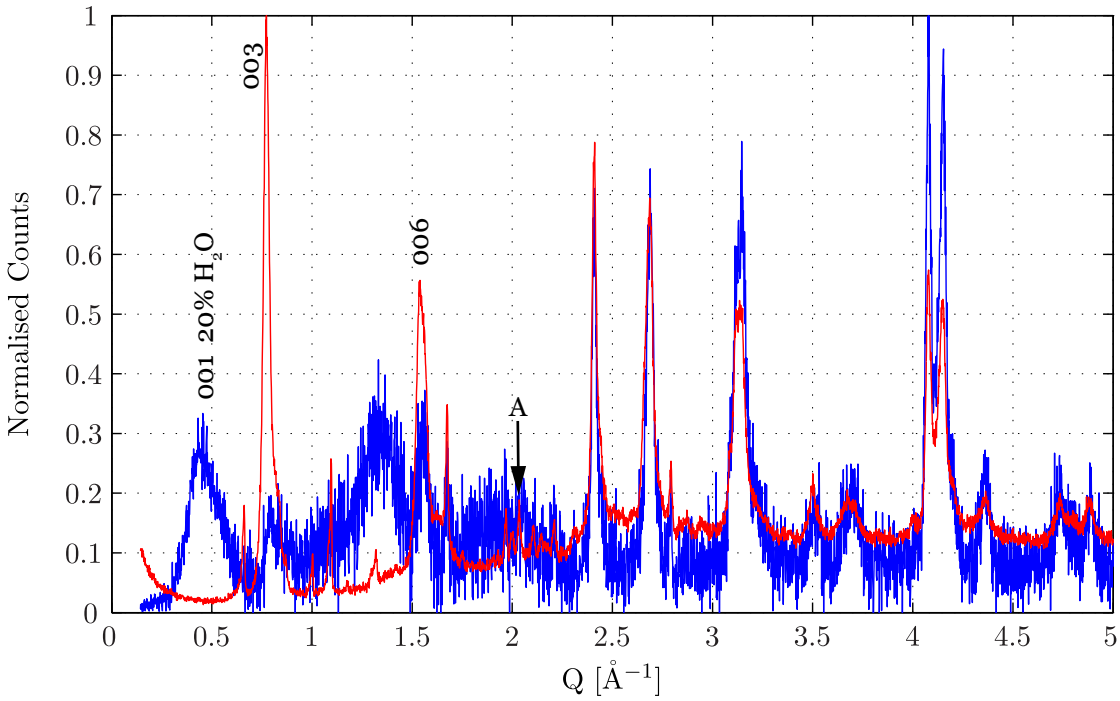


Figure 6.3: XRD of the hydrogenated LDH-TA at — lab humidity and — 20% added $H_2O$. Note shift of the (003) to form a broad peak at 0.45 Å$^{-1}$ in the 20% added $H_2O$ sample. The $a$-axis = 3.08Å is denoted with 'A' and the (003) and (006) peaks of the LDH-TA at lab humidity have been indicated.

LDH-TA + 5% $H_2O$. XRD of the 20% added $H_2O$ and of the LDH at lab humidity is shown in Figure 6.3. The data for the XRD taken on the LDH with added water was taken by sealing the LDH with Kapton tape and then removing the background due to the Kapton post measurement. The data for the 20% added $H_2O$ LDH-TA is therefore more noisy. The (003) peak is reproduced according to Greenwell[141] for the sample at lab humidity. We therefore infer that the broad peak at $\sim$ 0.45 Å is from the (001) i.e.$d$-spacing of the expanded clay of 13.96 Å and that the gallery spacing is therefore $\sim$ 9.2 Å following subtraction of the hydroxide layer thickness of 4.8 Å. This corresponds to the gallery spacings observed for expanded and collapsed interlayer spacings from previous measurements[141,142]. The samples parameters for the experiment are shown in Table 6.1 along with the total number of water molecules per TA.

The final analysis is directed towards the motion of the water in the interlayer and the terephthalate anion.

The sample environment used for this experiment was a standard CCR using liquid helium as a cooling agent to lower sample temperature to 5K. The sample can used for the experiment was an annular high-pressure aluminium cell with 1$mm$ thickness. This

| Sample | Gallery height [Å] | Added $H_2O$ [% by mass] | $H_2O$ per TA |
|---|---|---|---|
| Lab RH | 3.46 | - | 4.80 |
| a | $\sim 9.2$ | 20 | 16.24 |
| b | - | 5 | 7.88 |

Table 6.1: $\frac{Mg}{Al} = 5.7$ LDH-TA parameters at laboratory relative humidity, 5% and 20% additionally hydrated samples.

geometry reduces the probability of multiple scattering events and also minimises beam attenuation thus was chosen over using a purely cylindrical or flat plate sample cell. The can was sealed using an indium O-ring and was tested in a vacuum oven for any leaks prior to loading onto the beamline. The sample can had top and bottom heaters and a temperature sensor which was accurate to within 2 K.

The 20% added $H_2O$ LDH-TA, was cooled to 5K and quasi-elastic and elastic measurements were performed in order to obtain background readings. The sample was then heated up successively to 150K, 210K, 240K, 260K, 280K and 320K. The 5% added $H_2O$ LDH-TA was cooled to 5K and heated to 220K and 320K. After equilibration at each temperature, quasi-elastic data was collected for 6 hours to optimise the statistics.

## 6.3 Data Analysis Procedure for QENS Data

The 49 functional detectors of IRIS were grouped into 17 spectral groups spanning a $Q$-range of 0.421 - 1.17 $Å^{-1}$. The QENS data was analysed using the programme MODES, v3.0[143] which corrected for multiple scattering, absorption and detailed balance for each measurement, detector efficiency and sample container. The resulting data was normalised to the elastic window intensity at 5K. The lowest temperature data set (at 5K) could be fit using a delta function and had similar FWHM to the resolution of the instrument making it viable to be used as the resolution function with which each proceeding data set was deconvolved with. This allowed isolation of the terephthalate + water motion from the clay. After deconvolution, a constant background correction was applied to all data sets and at each temperature, data were fit to the model of an elastic line or both the elastic and just one quasi-elastic peak. The fit parameters for the elastic and quasi-elastic peaks were then imported into Matlab and fit using a least-squared fit for the rotational and translational diffusion models considered in Section 3.4.1.

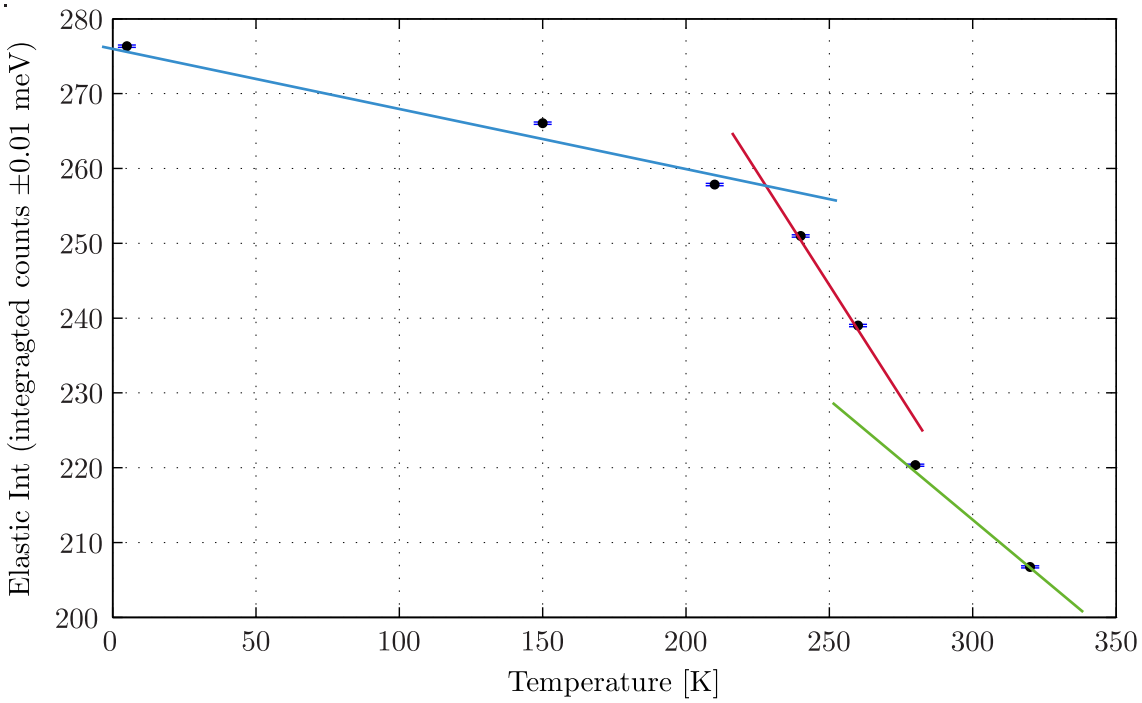


Figure 6.4: Elastic intensity calculated by integrating the counts from ± 0.01 meV of the fully grouped quasi-elastic data for the 20% $H_2O$–LDH-TA at each temperature. Blue, red and green lines indicate the three regions of interest (they are not fits to data).

## 6.4 QENS Results

**Aims**

- Study the dynamics of the terephthalate and relate directly the diffusion of the anion to its orientation as controlled by layer charge.
- Observe the expected freezing out of both rotational and translational motion of the $H_2O$.

## 6.5 QENS Results 20% $H_2O$ LDH-TA

### 6.5.1 Neutron Scattering intensity

The first sample to be looked at is the LDH with an added 20% by weight of $H_2O$ which means a total of 16.24 $H_2O$ molecules per TA. The first method for checking where motion of the interlayer components freezes out is to plot the variation of total elastic intensity (dependent on total neutron cross section) with temperature and compare with the intensity at the lowest temperature, 5K. At 5K, we know that the interlayer $H_2O$ and the TA

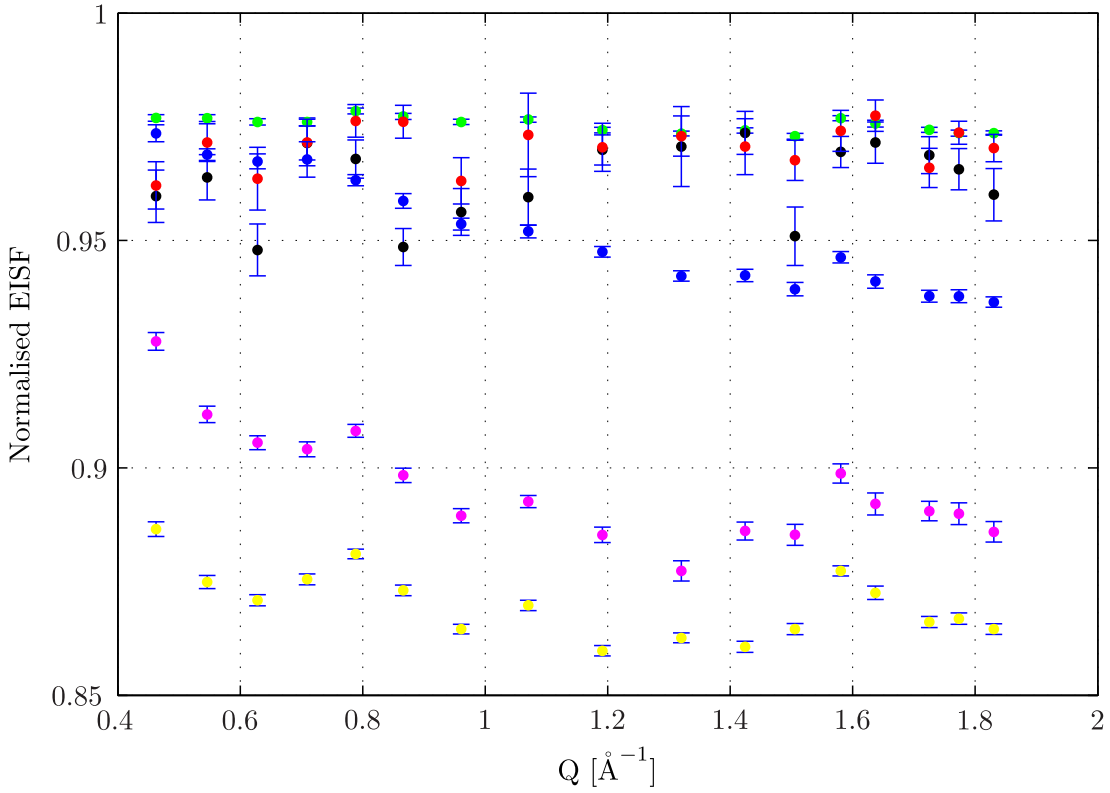


Figure 6.5: Normalised elastic incoherent structure factor across the 17 groups in $Q$ of the 20%-LDH-TA. ● 150 K, ● 210 K, ● 240 K, ● 260 K, ● 280 K, ● 320 K. Note relatively flat EISF for 150, 210 and 240 K. First marked drop in EISF at 260 K and again at 280 K.

are not mobile and therefore can take this to be the resolution function for the remaining temperatures. Any drop in the intensity indicates there is and introduction of $H_2O$ or TA motion since the elastic intensity refers to 'immobile' material. Figure 6.4 shows the elastic intensity calculated by integrating the counts between $\pm$ 0.01 meV of the energy window and grouping all the data in $Q$ for the 20%-LDH-TA at each measured temperature. This highlights three regions in the data which may be of interest.

As described in Section 3.4.1, any drop in the intensity of the elastic portion of the scattering as a function of $Q$ indicates that motion is introduced into the system. Therefore in Figure 6.5 the normalised elastic incoherent structure factors across the 17 grouped detector banks in $Q$ of the 20%-LDH-TA is plotted for each of the temperatures having fit 1 QE peak and the elastic line to the data. The large error bars on the EISF for the lower temperatures: 150 K, 210 K and 240 K indicate that 1 QE peak is an over-fit of the data and that the elastic is sufficient at these temperatures. Also, a relatively $Q$-independent EISF $\approx$ 1 is observed at these temperatures implying that there is no translational or rotational motion observed. The first marked decrease in the EISF is seen at 260 K

with a definite $Q$ dependence indicating the first introduction of motion into the system. There is another marked decrease in the EISF from 260 to 280 K. There are a few quite prominent features in the EISF. Firstly, it is clear that at $Q = 0$, the EISF is not tending to one. This is because there cannot be completely immobile interlayer material at any given temperature, and the discrepancy from 1 is attributed to the vibrational part of the molecular motion. With this in mind, the fits for 150, 210 and 240 K are fit with only the elastic line.

The number of Lorentzians for the QE component are chosen, not only by looking at the residuals but also looking at the difference in the normalised $\chi^2$ of the fit to the data for just the elastic line fit to 1 QE peak and the elastic peak. A dramatic drop in the $\chi^2$ from 0 to 1 QE peak indicates that there is likely to be QE in the data. The fits across a range of $Q$-values are shown for the lowest 150 K data and highest 320 K data in Figures 6.6 and 6.8 respectively. Figure 6.7 shows the fits, QE peak and residuals at $Q = 0.96\text{Å}^{-1}$ for the temperature data sets from 210 to 280 K. This is to show the quality of the fit for the chosen number of QE peaks and using the 5K data as the resolution function. We see excellent fits for all the data sets and can therefore conclude that for 150 to 240 K, there is no quasi-elastic scattering observed and the rotation and translational motion of the water and TA are restricted. However for $\geqslant$260 K, a single QE peak is required to fit the data indicating the the water and TA can now move. Further investigations into the $Q^2$-dependency of the QE Lorentzian HWHM is required to ascertain the type of motion occurring.

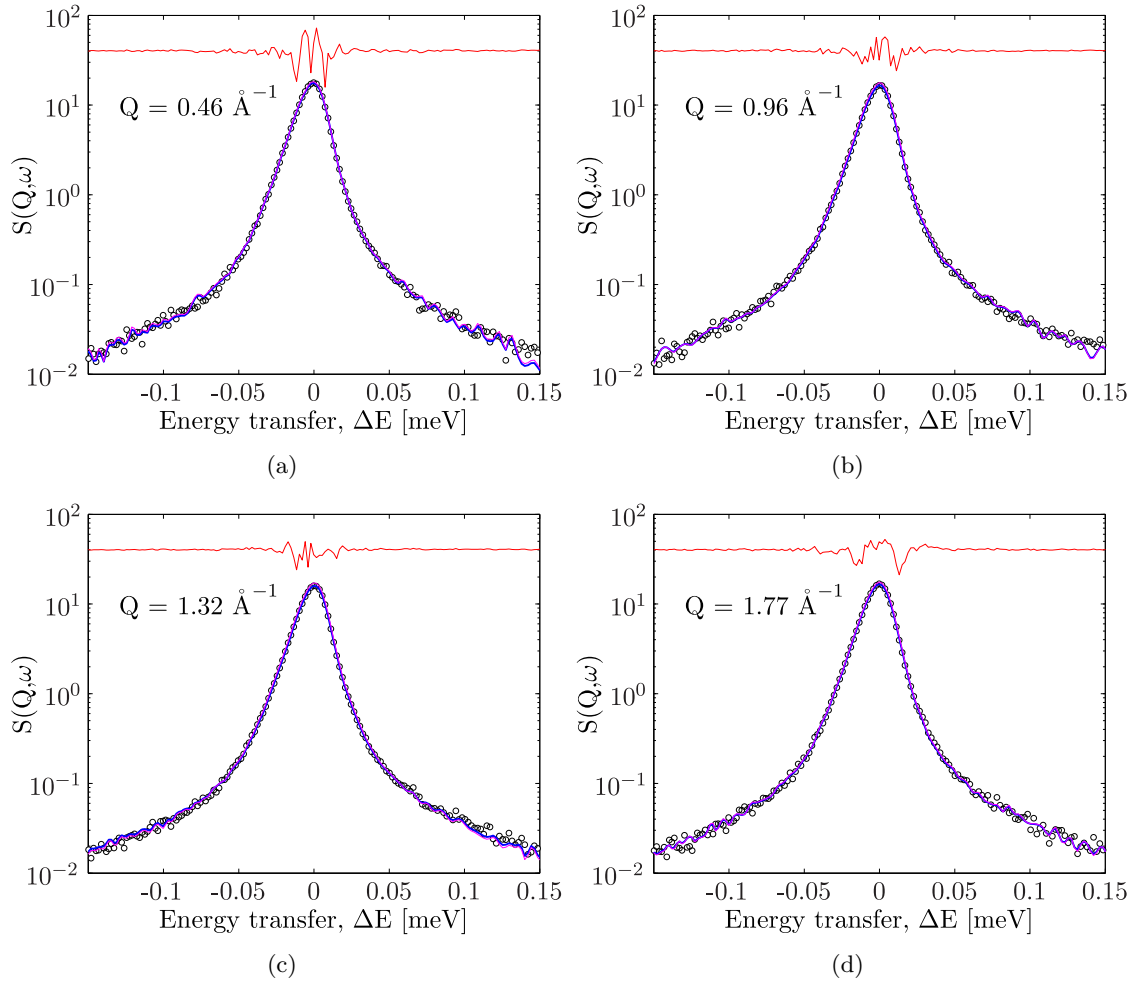


Figure 6.6: The QENS fits to a range of spectral groups for the data collected on the 20%-LDH-TA at 150 K fitting only an elastic line and the resolution function (5K data) to the o data; — fit; — elastic line and the resolution function (5K data); — residuals are also plotted: the difference between the data and the fit. Note the $y$-axis is a log-scale for the data and fit, however the residual is shifted up by 40 and plotted on a linear scale from $\pm 0.01$ meV.

**What is moving?**

Since the water and the terephthalate ions are hydrogenated, the motion of the two are coupled together. It is possible to ascertain which portion of the TA – water interlayer is actually contributing to the translational and rotational motion by comparing the ratio of elastic intensity ($A_0$) at 5K to the the elastic intensity at 320 K.

At 5K all ions and water molecules are immobile therefore all atoms contribute to the elastic intensity. At 320 K, diffusion is clearly observed. Atoms which are diffusing are not immobile and therefore do not contribute to the elastic intensity. Since the incoherent scattering is used to measure the diffusion of molecules, we can assume that at 5K, the

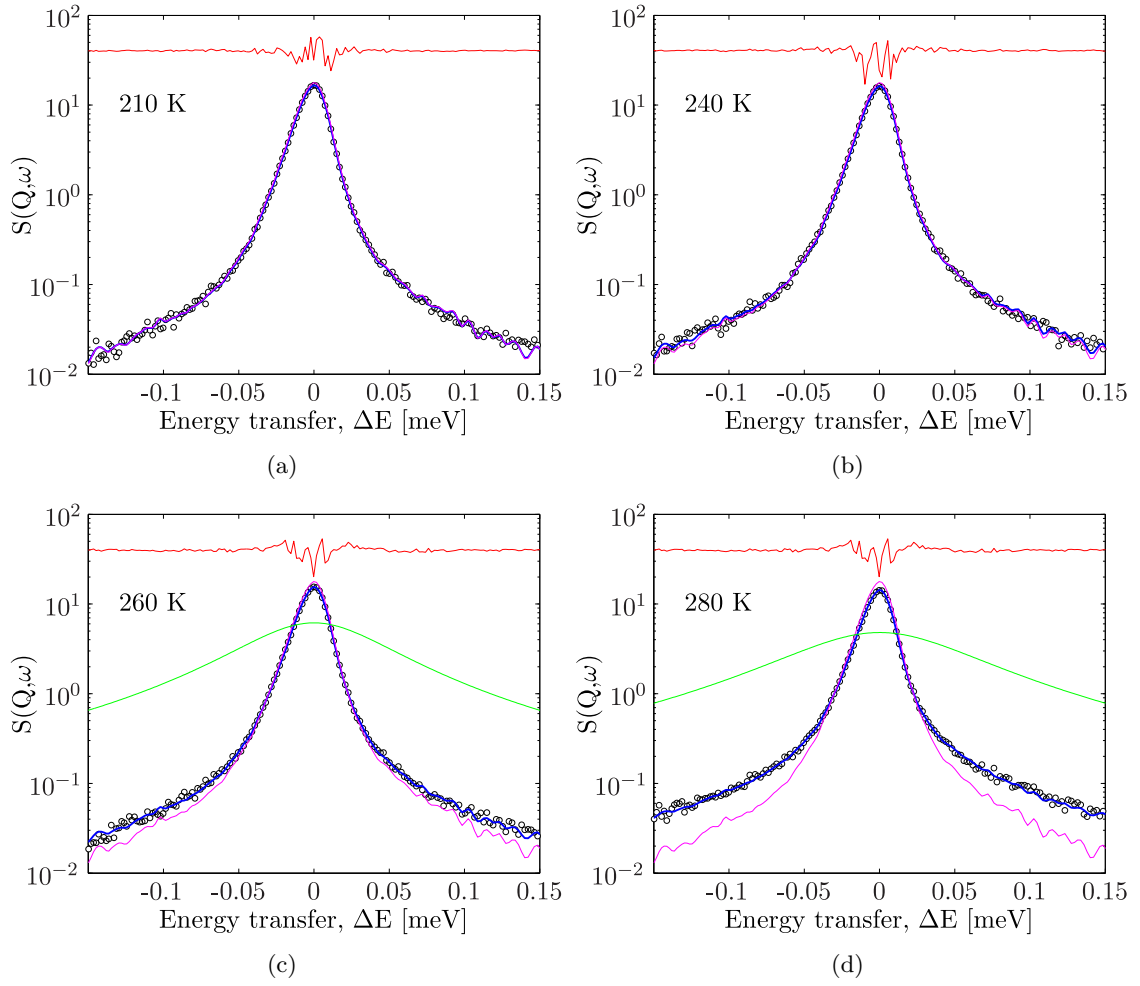


Figure 6.7: The QENS fits to the data collected on the 20%-LDH-TA for $Q = 0.96\text{Å}^{-1}$ at **(a)** 210 K, **(b)**240 K, **(c)** 260 K and **(d)** 280 K. o data; — fit; — elastic line and the resolution function (5K data); — residuals; — QE Lorentzian. Note the $y$-axis is a log-scale for the data and fit, however the residual is shifted up by 40 and plotted on normal scale from ±0.01 meV.

incoherent scattering is at a maximum and all atoms contribute. At 320 K, incoherent scattering of the diffusing atoms is seen as a QE peak and therefore the incoherent scattering will drop according to the type and proportion of diffusing atoms. We can therefore equate the ratios of the two:

$$\frac{A_0(5K)}{A_0(320K)} = \frac{\mathbf{b}_{Inc}(allatoms)}{\mathbf{b}_{Inc}(non-diffusingatoms)} \tag{6.2}$$

From Figure 6.4, the ratio of $\frac{A_0(5K)}{A_0(320K)} = 0.748$. If we consider only the interlayer water to contribute to the motion at 320 K of the 20%-LDH-TA (TA:water 1:16.24), using the Table 3.3 of incoherent neutron cross-sections, we obtain $\frac{\mathbf{b}_{Inc}(allatoms)}{\mathbf{b}_{Inc}(non-diffusingatoms)} = 0.761$.

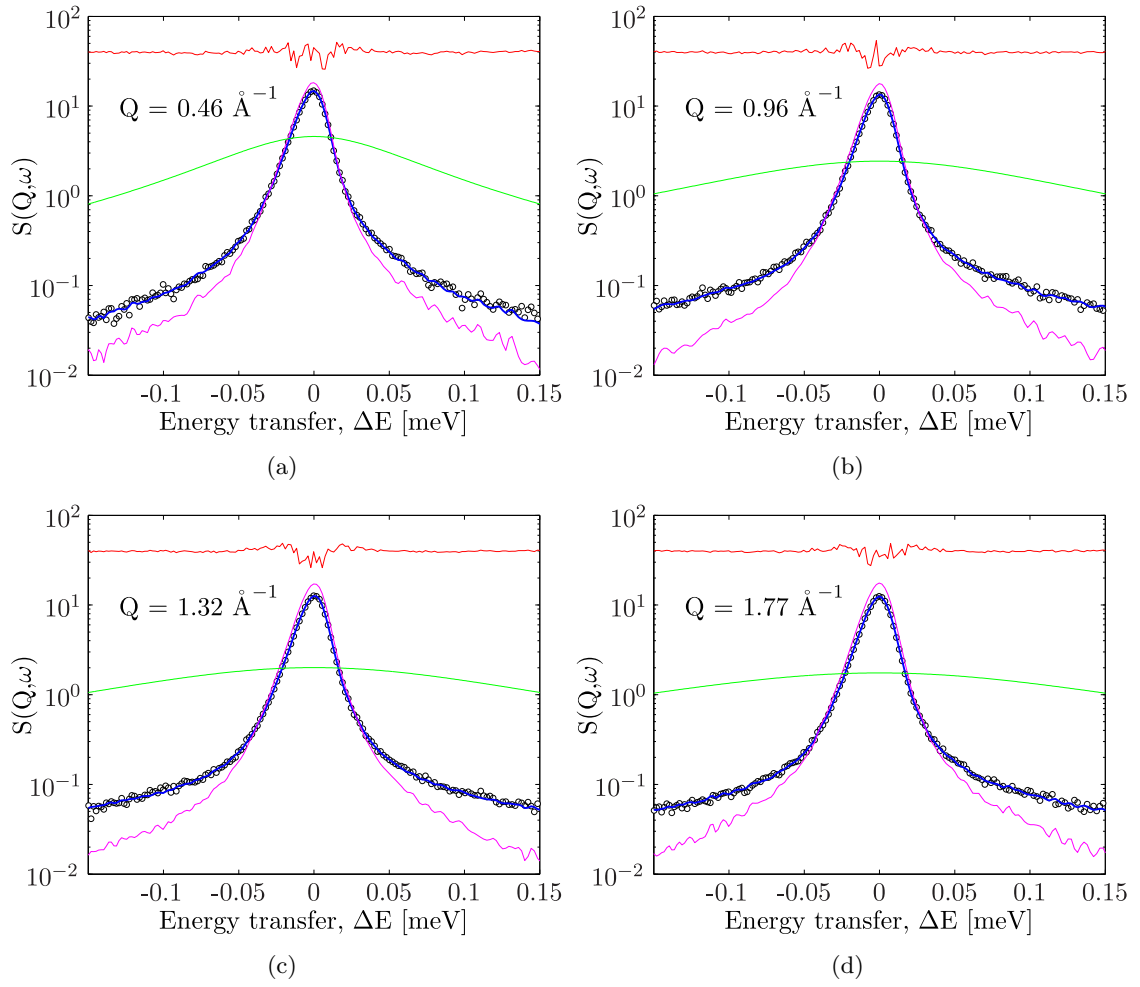


Figure 6.8: The QENS fits to a range of spectral groups for the data collected on the 20%-LDH-TA at 320 K fitting only 1 QE Lorentzian. o data; —fit; — QE Lorentzian; —elastic line and the resolution function (5K data); —residual. Note the $y$-axis is a log-scale for the data, fit, resolution function and QE peak; the residual is shifted up by 40 and plotted on normal scale from ±0.01 meV.

These two values are in excellent agreement and therefore we can conclude that the motion at 320 K is primarily related to the water molecules. If we consider only terephthalate to be moving this ratio is 0.900 and if we consider both the water and the terephthalate to exhibit translational diffusion, the ratio is 0.662.

Since maximum diffusion occurs at the max T i.e. 320 K, we can assume that any translational diffusion below this temperature will only be associated with the water molecules.

### 6.5.2 Freezing Out of Rotation

The normalised EISF and HWHM, having fit 1 QE peak to the data at 240 and 260 K, is plotted: Figure 6.9(a) and Figure 6.14(b) respectively. Looking at the data obtained

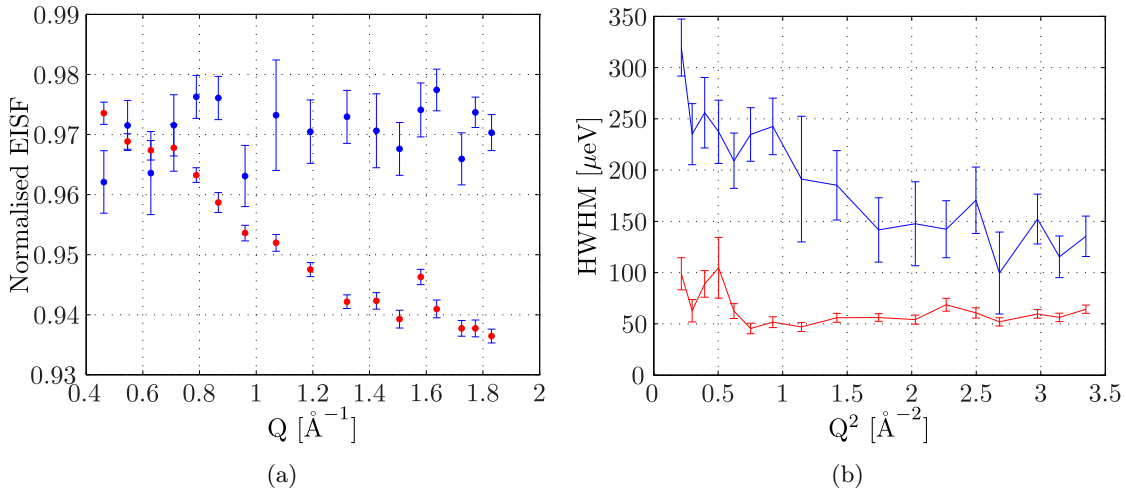


Figure 6.9: **(a)**Normalised EISF and **(b)**HWHM data having fit 1 QE peak to the 20% added $H_2O$ LDH-TA — 260 K, — 240 K. The lines between the points in **(b)** are not fits but used to emphasise the variation from one point to the next.

at 240 K, the EISF and HWHM data points have extremely large error bars and show a completely random scatter as a function of $Q$. This implies that a 1 QE peak is an over-fit of the data and we can fit 240 K with just the elastic line. The EISF at 260 K however, shows very little $Q$-dependence (a 0.04% variation between max and min) implying that the motion of the water is restricted to rotation only. The HWHM shows no $Q^2$ variation either to further support this.

In principle, the EISF can be fitted for the $Q$-independent rotation to determine the exact type of rotation that the water exhibits, however due to the presence of Bragg peaks in the data, this is not possible for the present data. A straight line can be fit to the HWHM of the 260 K data, Figure 6.10. The first 4 data points have been plotted on the graph but are left out of the fitting routine due to the very large error bars associated with them.

### 6.5.3 Jump Diffusion Models

Two jump diffusion models, Hall-Ross (HR) and Singwi-Sjölander (SS), discussed in Section 3.4.1, were applied to the subsequent $Q^2$-dependency of the HWHM of the 280 and 320 K data for the LDH-TA. These are displayed in Figures 6.11(a) and 6.11(b) respectively. In addition, the trend expected for pure Fickian diffusion is represented by the straight red line on each graph, obtained by a linear regression fit on the two lowest $Q$-values. The Fickian model requires this line to pass through the origin. The calculated diffusion coef-

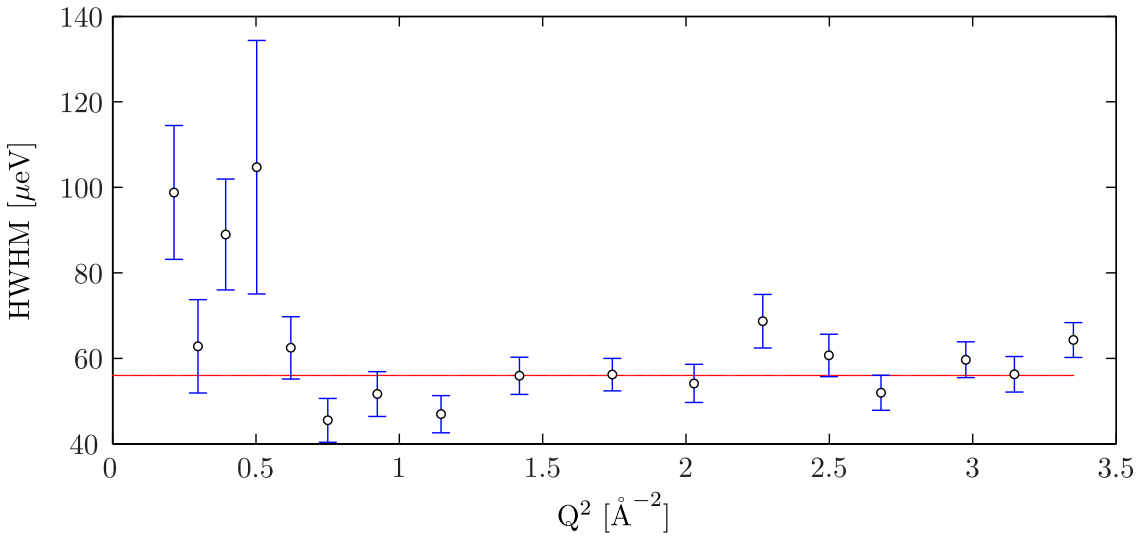


Figure 6.10: Horizontal straight line fit to the 20% added $H_2O$ LDH-TA at 260 K. The first 4 data points are left out of the fit due to the large error bars associated with them.

ficients $D_{trans}$, jump length $l$ and residence time $\tau_t$ have been calculated by least square fit with the experimental HWHM for both models and are presented in Table 7.3. Also stated is the QENS measurement for $D_{trans}$ for bulk water at 295 K measured on IRIS[10].

The best fit of the models is the Singwi-Sjölander model for both the 280 and 320 K data sets. It is clear that the diffusion at the these temperatures is not Fickian and confinement is having an effect on the motion of the water molecules. Although the calculated $D_{trans}$ of this model are relatively high i.e. compared to bulk, at 320 K we are 47 K above the melting point of water i.e. the system has an increased amount of thermal energy than bulk at room temperature (300K). Alos, the charged ends of the terephthalate ions interact with the clay surfaces as opposed to the water molecules and also act as barriers disrupting the hydrogen-bonding network of the water molecules. This can allow the water molecules to move faster through the interlayer than they would in bulk. The terephthalate ions also have a hydrophobic aromatic ring at the centre allowing for water molecules to ready pass through the interlayer. Added to this, we know that the *d*-spacing of the LDH at 20% added water content increases from 3.6 Å to ∼13.96 Å allowing more space for the water to travel through. We also see a larger $D_{trans}$ for the sample at 320 K compared to 280 K which is expected due to the increase in thermal energy to the system. The melting point of $H_2O$ is 273.8 K and therefore it is clear that the extent of the mobility of the water molecules is tied to this. Rotational motion freezes out at a slightly lower temperature, however since the $H_2O$ is confined within the LDH,

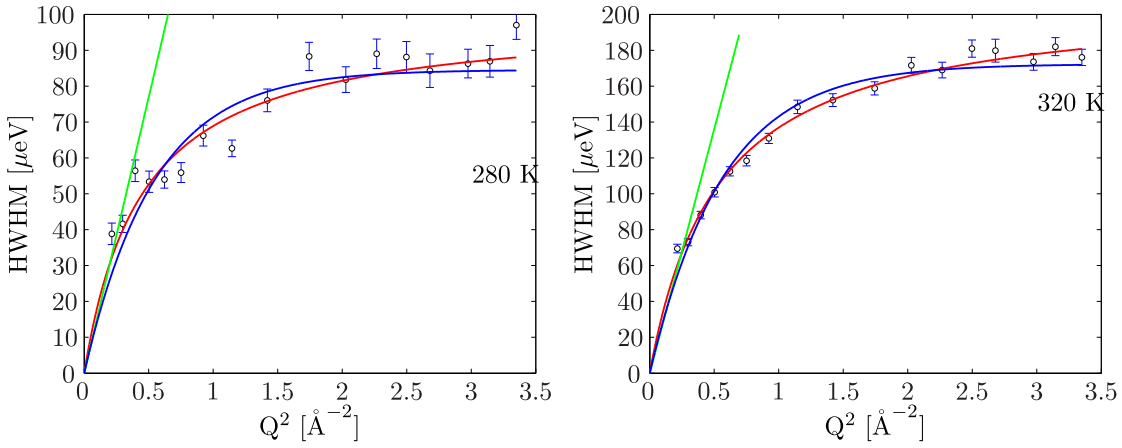


Figure 6.11: QENS HWHM data and models for water diffusion within the 20%-LDH-TA at **(a)** 280 K **(b)** 320 K. Singwi-Sjölander model, Hall-Ross, Fickian.

| T [$K$] | Fit Model | $l$ [Å] | $\tau - t$ [$ps$] | $D_{trans}$ $\times 10^{-9}[m^2\ s^{-1}]$ | Red $\chi^2$ |
|---|---|---|---|---|---|
| 280 | HR | 3.34 ±0.23 | 7.79 ± 0.36 | 2.4 ± 0.3 | 6.16 |
| | SS | 3.66 ±0.30 | 6.60 ± 0.33 | 3.4 ± 0.6 | 3.52 |
| 320 | HR | 3.26 ± 0.10 | 3.82 ± 0.09 | 4.6 ± 0.3 | 5.13 |
| | SS | 3.37 ± 0.09 | 3.15 ± 0.07 | 6.0 ± 0.4 | 1.94 |
| 295 bulk (Swenson[10]) | HR | 1.4 | 1.4 | 2.5 | |

Table 6.2: Comparison of parameters from Hall-Ross(HR) and Singwi-Sjölander(SS) jump diffusion fits to HWHM of 5% added LDH-TA QENS data at 280 and 320K, alongside the $D_{trans}$ for bulk $H_2O$ as measured by Swenson *et al*[10].

the melting point will be lower than 276.8 K.

## 6.6 Results 5% $H_2O$ LDH-TA

The second sample to be studied is the LDH-TA with 5% added $H_2O$. There is now 7.88 $H_2O$ molecules per terephthalate anion, about half compared to the previous sample. Figure 6.13 shows the integrated intensity between ± 0.01 meV for the 20% added $H_2O$ LDH (red) and the 5% added $H_2O$ LDH (blue). If we calculate the total scattering of a system (total neutron cross-section) with 15% less water, the elastic intensity should drop by an equivalent amount. This is seen at 5K from the 20% added water LDH to the 5% added water LDH in Figure 6.13 thus confirming the amount of water absorbed by the LDH.

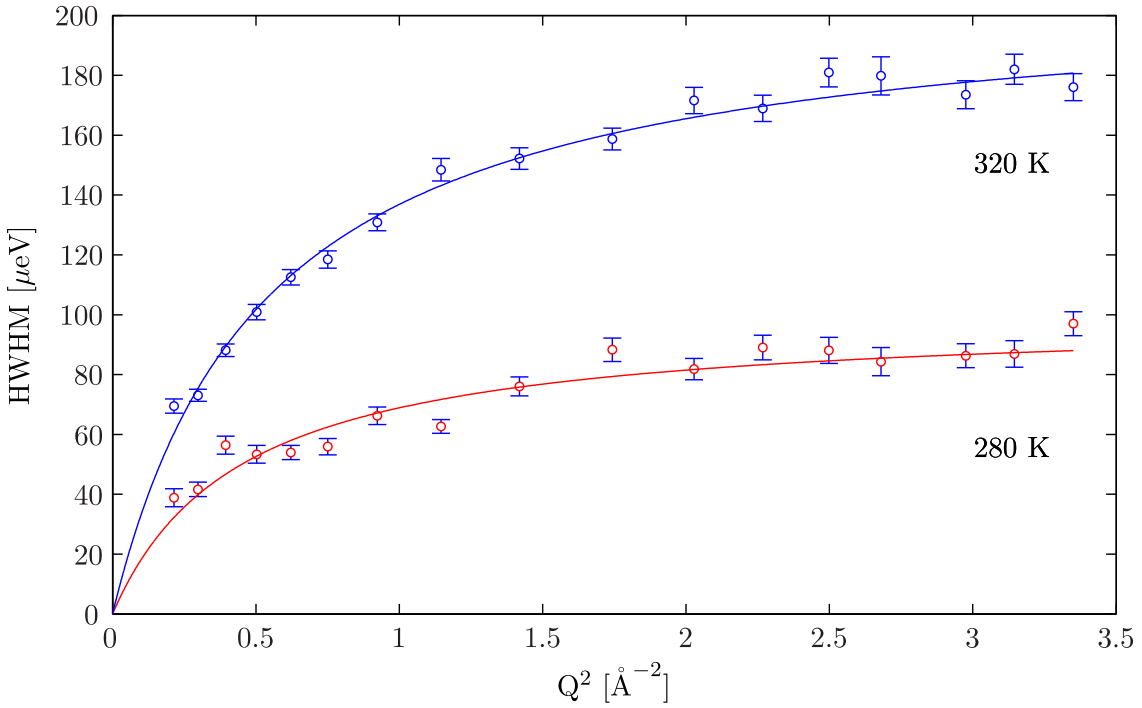


Figure 6.12: $Q^2$-dependence of the broadening of the quasi-elastic components with data and Singwi-Sjölander fit for the LDH-TA with 20% added water at ○ 280 K and ○ 320 K.

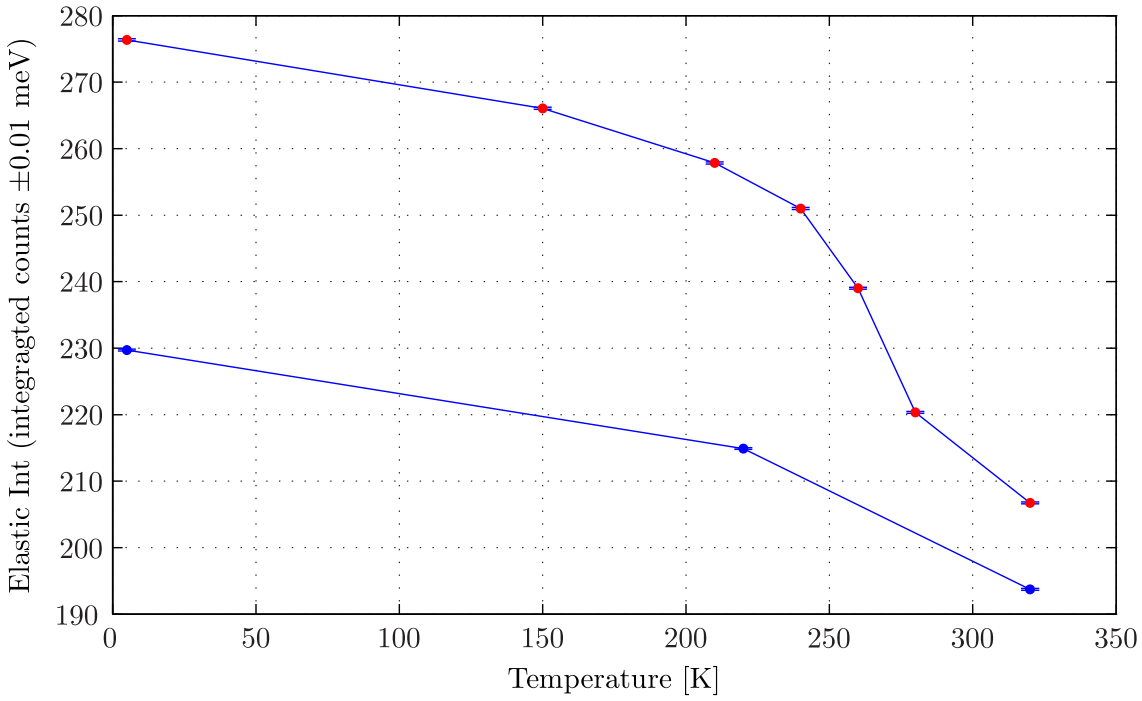


Figure 6.13: Elastic intensity calculated by integrating the counts from ± 0.01 meV of the fully grouped quasi-elastic data for the ● 20% $H_2O$–LDH-TA, ● 5% $H_2O$–LDH-TA. Note large difference in intensity at low temperatures however much less at higher temperatures.

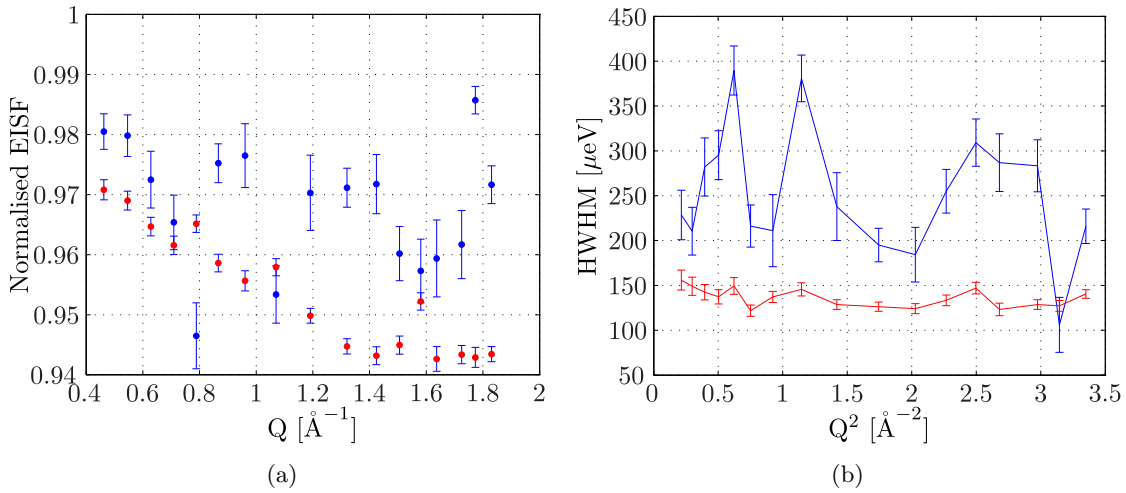


(a) (b)

Figure 6.14: **(a)**Normalise EISF and **(b)**HWHM data having fit 1 QE peak to the 5% added $H_2O$ LDH-TA —320 K, — 220 K. The lines between the points in **(b)** are not fits but used to emphasise the variation from one point to the next.

To identify how to best fit the 5% added $H_2O$ sample, the normalised EISF and HWHM, having fit 1 QE peak to the data, is plotted: Figure 6.14(a) and Figure 6.14(b) respectively. Again, looking at the data obtained at 220 K, the EISF and HWHM data points have extremely large error bars and show a completely random scatter as a function of $Q$. This implies that a 1 QE peak is an over-fit of the data and we can fit with just the elastic line. The EISF at 320 K however, shows relative $Q$-independence (a 0.03% variation between max and min) implying that the motion of the water and terephthalate is restricted to rotation only. The HWHM is tantamount to this since no $Q^2$ variation is measured. Looking at the ratio of the elastic scattering between 5 to 320 K and the ratio in the incoherent cross-section between all the atoms and assuming that only the water is moving, we obtain equal values. From this we can infer that the rotational motion observed is associated with the water.

The rotational diffusion coefficient of the 5% added $H_2O$ LDH-TA at 320 K data can be obtained by fitting the HWHM with a horizontal line and find the intercept with the $y$-axis. This is shown in Figure 6.15. Again, the EISF cannot be fitted to determine the type of rotation due to the presence of Bragg peaks in the data.

## 6.7 Summary

We do observe a dramatic effect in the mobility of the interlayer components depending on both temperature and water content. Firstly, we have quite a small gallery spacing of 3.46

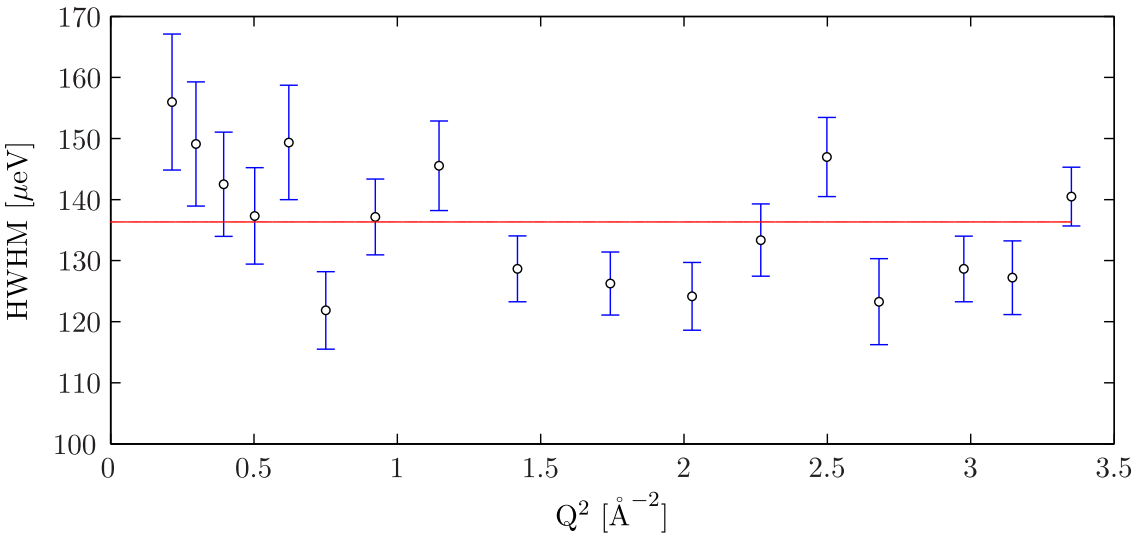


Figure 6.15: Horizontal straight line fit to the 5% added $H_2O$ LDH-TA at 320 K to show therefore, that motion is rotational.

Å which indicates that the TA are lying flat in the interlayer at lab humidity. Although we do not have data to show this, we assume that at 5% added $H_2O$ i.e. TA:water 1:7.88, the interlayer spacing does not increase that much. No motion is observed in the system until the temperature is increased to 320 K at which point we are able to fit 1 QE peak to the data indicating that some translational or rotational motion is present in the system. We found a $Q$-independent HWHM indicating that the motion is solely rotational. Since both the TA and the water is hydrogenated, we are not able to quantitatively uncouple the rotation of the two molecules however we can assume that most of the contribution of the rotation is from the water by comparing the drop in elastic intensities and incoherent cross-sections of the mobile parts of the system.

Increasing the water content to 1:16.24 TA:water, expands the interlayer spacing to $\sim$ 13.96 Å. We are able to resolve the freezing out of the water motion: no rotation or translational motion below 260 K, only rotation at 260 K temperature and full translation between 280 and 320 K however. Since the terephthalate is a bulky ion it can disrupt the hydrogen bond network of the water alongside minimally interacting with the water. This allows the water to move passed relatively quickly with translational diffusion coefficient calculated using the Singwi-Sjölander $D_{trans}$ = 6.0 $\times 10^{-9}$ $m^2s^{-1}$ and 3.4 $\times 10^{-9}$ $m^2s^{-1}$ at 320 K and 280 K respectively which is larger than bulk at similar temperatures[10]. We do observe the trend of increasing diffusion coefficient with temperature as previous studies have shown[139]. This is attributed to the fact that at this layer spacing, the terephthalate

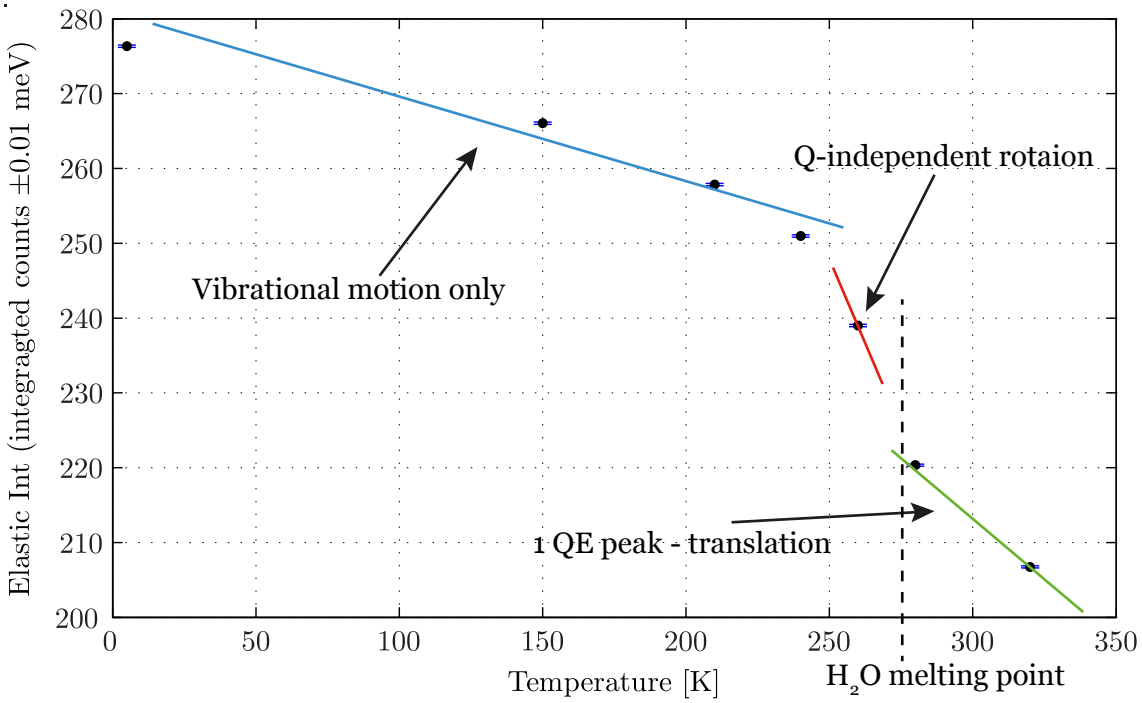


Figure 6.16: Elastic intensity calculated by integrating the counts from ± 0.01 meV of the fully grouped quasi-elastic data for the 20% $H_2O$–LDH-TA at each temperature. Blue, red and green lines indicate the temperature width of the types of motion exhibited by the water molecules in the interlayer.

ions are lying in plane to the *c*-axis and opening up the layers. Since it minimally interacts with the water and the fact that it is a bulky ion which disrupts the hydrogen bonding of the interlayer water, though confined in the interlayer, water molecules are unhindered in mobility. At 260 K only rotation is observed and below this all motion is frozen out of the system. The temperature at which motion freezes out of the system, does seem coupled with the melting point of water since just below 273 K we observe only rotation which is possible since confined water has a lower melting point. Below this, all motion of the water and terephthalate is frozen. Returning to the three aims set out at the beginning, we have observed that the terephthalate does not contribute to the translational diffusion coefficient of the sample. The rotation of the anion is however coupled to the rotation of the water molecules and can not be distinguished quantitatively from the water rotation since the sample used contained both hydrogenated terephthalate and $H_2O$, however the discussion explains why we believe we are seeing primarily the water rotation. The motion of the water very heavily depends on the number of molecules per terephthalate and is coupled with an increase in the interlayer spacing of the LDH allowing more freedom for movement. We can therefore redefine the three regions across which each type of motion

is frozen out of the $H_2O$ in the 20% added LDH, Figure 6.16.

# Chapter 7

# Macroscopic Linear Swelling Measurements

This chapter presents a preliminary investigation into the macroscopic clay swelling of compacted vermiculite-talc samples during the very initial stages (0 - 5 mins) of fluid addition. This is because we aim to investigate the very initial problems that occur, described in Section 2.5, when drilled cuttings are released from the walls of the wellbore. Measurements have been made using a bespoke instrument using non-contact sensors to measure the expansion, with the manufacture of the instrument occurring at the Durham University. The design of the instrument and work in this chapter was motivated by a five-week placement spent in the research laboratories at M-I Swaco[144] who co-funded this project. Since I have designed and coded the equipment, it is also a test study of the instrument itself and has been trialled in the following manner:

**Aims**

- To design and build a robust instrument that will allow for controlled humidity clay swelling measurements on compacted clay samples in an environment where the clay samples are in minimal contact with other aspects of the instrument.
- To measure the *initial* macroscopic (uniaxial) swelling response of compacted hexamethylene diamine (HMDA) and tetramethylammonium (TMA) exchanged vermi-

| Sample No. | $H_2O$ (g) | NaCl (g) | HMDA (g) | Molarity (M) |
|---|---|---|---|---|
| 1 | 280 | - | - | - |
| 2 | 280 | 6.6 | - | 0.40 |
| 3 | 280 | 12.3 | - | 0.75 |
| 4 | 22 | - | 5.10 | 2.00 |

Table 7.1: Masses and molarity for each of the fluids with which the macroscopic swelling of the vermiculites were tested.

culites in $H_2O$ and also in test solutions of brine and $HMDA_{(aq)}$ at ambient pressure and temperature conditions.

The experiments described here are the macroscopic swelling analogues of the high pressure neutron studies performed in Chapter 5 in which we observed no crystalline swelling of the minerals. We have defined 'macroscopic' in this case to be the behaviour of the *compacted* samples in the test fluids.

### 7.0.1 Methods

#### Sample Preparation

The as received Li-purified clays were vermiculites from Flexitallic gasket makers with clay composition:

$$[Si_{6.30}Mg_{5.44}Al_{1.65}Fe_{0.6}O_{20}(OH)_4]^{1.3-}1.3Li^+ \bullet 4H_2O \tag{7.1}$$

To prepare the clay in a homoionic form, the existing lithium interlayer cations were exchanged for mono- and di-valent cations by placing batches of the as received clay in an excess 2 molar solution of the chosen salt. 50g batches of the as received vermiculite were placed in a 2 molar solution of NaCl, KCl, TMACl and HMDA obtained from Sigma Aldrich $> 98\%$ purity. The TMA- and HMDA-exchanged vermiculite were prepared in order to compare with the preceding work in chapter 5. The K- and Na-exchanged vermiculites have been used as a guide to the relative swelling inhibition of the TMA- and HMDA-vermiculites since potassium is a standard addition to drilling fluids in terms of minimising swelling via cation exchange as described in Section 2.6.1. The clay was soaked in these solutions for 24 hours, washed with de-ionised water and then placed in the oven to dry at 80°C for 24 hours. This was repeated 3 times. X-Ray diffraction was performed

on the sampled pre and post treatment to verify that the $d$-spacings of the exchanged vermiculites and to see whether in the case of the HMDA, the exchange was successful.

The resulting formulae of the clays were thus:

$$[Si_{6.30}Mg_{5.44}Al_{1.65}Fe_{0.6}O_{20}(OH)_4]^{1.3-}[1.3Li^+/1.3Na^+/1.3TMA^+/0.65HMDA^{2+}]\bullet 4H_2O \tag{7.2}$$

The cation exchange capacity of this vermiculite is in the range 50 - 100 mEq /100g which is slightly low for vermiculites in general and more akin to a CEC found for montmorillonites. The exchanged clays were ground to particle size of 20 $\mu$m ready for pressing into compacted disks for the experiments. 1.25 g of milled, exchanged vermiculite was mixed with 1.25 g of talc of particle size 20 $\mu$m i.e in a 1:1 ratio. Talc was added in order to take a first step towards creating a more 'natural' sample with a non-swelling component for the experiments. In natural mined samples, quartz is the common non-swelling component. The mixed talc and vermiculite clay was pressed in a 20 mm diameter die at 10 Tonnes of pressure (20,000 psi). The average thickness of the compacted disks was $\sim$ 3.5 - 4.0 mm. These were left to equilibrate at lab humidity for 24 hours before using in a measurement.

Test fluids were prepared in a fume hood as hygroscopic ammoniated salts evaporate . The fluids were made up to 280 ml volume such that only the base of the clay pellets were in contact with the test fluid. Four representative fluids were tested given in Table 7.1. Data was collected for:

- All the various exchanged vermiculites in distilled water
- Li- and TMA-exchanged in brine at seawater concentration and at 0.75M $NaCl_{(aq)}$.
- Li-exchanged in 2M $HMDA_{(aq)}$.

**Experimental Setup**

Figure 7.1 shows the sketch of the final version of the bespoke instrument designed and manufactured to perform the non-contact clay swelling experiments. The 'non-contact' refers to the contact-less linear displacement meters from Omega®[145] used to measure the height evolution of the clay pellets. The theory describing how the sensors work can be found in Appendix A.1. The inductive method used by these sensors does not require

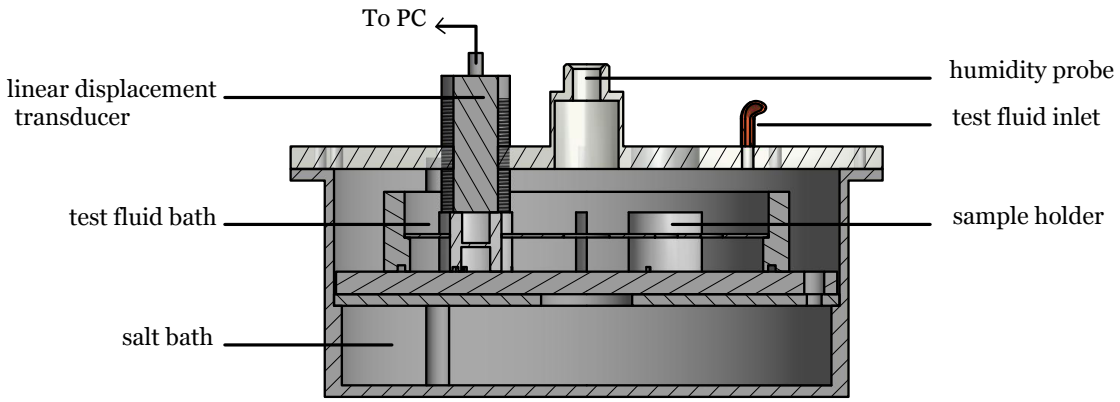


Figure 7.1: Custom designed and built swellometer for the macroscopic measurements of clay swelling within a controlled humidity environment.

any part of the sensor to be in contact with the clay or the inductive metal disk placed on top of the sample, Figure 7.2(a). This means there is no damping to the swelling response of the clay due to friction as observed in existing sensor technology.

The instrument allows for measurements on four pellets simultaneously in a single test drilling fluid and pre-equilibrated at a chosen humidity. The humidity probe could be used to measure the change in the humidity of the chamber as the pellets equilibrate in the relative humidity created by the salt solution. This is achieved by placing a chosen saturated salt solution in the salt chamber and leaving the pellets in the sealed instrument overnight (12 hours minimum) to equilibrate to the relative humidity governed by the salt. The results presented here do not show the application of this however the opportunity to do so is available.

Compacted clay samples were set up in the sample holder as shown in Fig 7.2 having been equilibrated with the lab humidity. The diameter of the sample holder was chosen to be 25 mm so that there was room for the clay to expand laterally. This is important primarily to avoid friction between the clay and the sample holder walls, thus heavily dampening the overall swelling response of the clay. It is also a viable design since when cuttings are released from the wellbore, they are no longer confined and are free to expand in all directions. The data acquisition was started just as the final portion of the test fluid was added and measurements of the height of the pellets were taken every 0.5 seconds for the duration of 30 minutes. Since the investigation focussed on the the initial swelling response, 30 minutes was deemed sufficient, however the standard time used in the oil industry to measure the full swelling response of the material is 16 hours which was

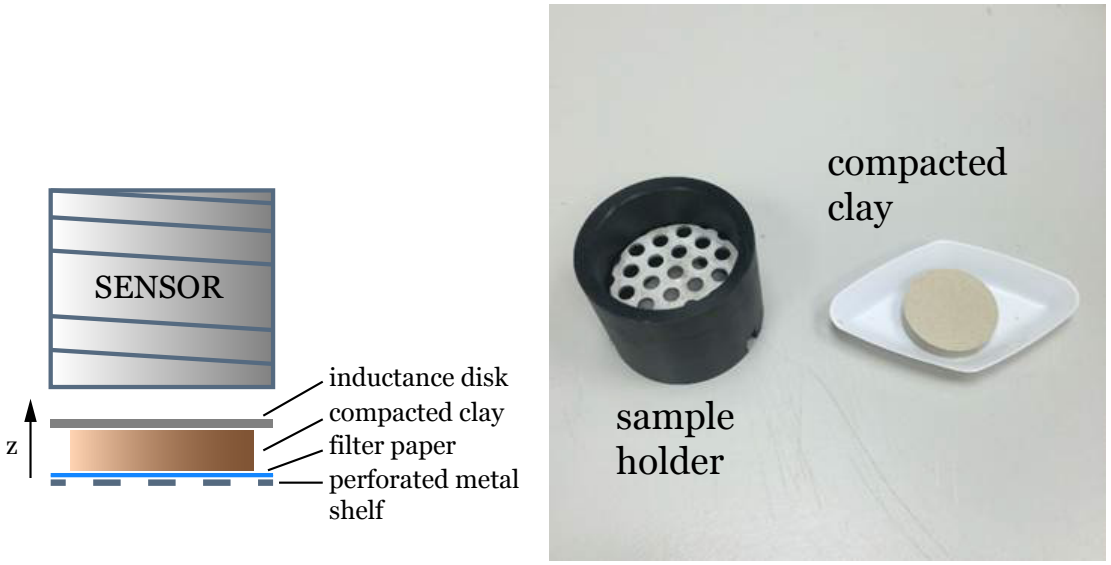


(a) (b)

Figure 7.2: **(a)** Sketch of sample setup inside the sample holder. **(b)** Photo of sample holder and an example of a compacted vermiculite:talc pellet.

possible if required.

#### Data Acquisition

For a full description of the LabVIEW code used to control the measuring of the instrument, see Appendix A. The sensors were connected into the analogue ports of the Data Acquisition Card (DAQ card) and then controlled via LabVIEW.

Figure 7.3 shows the simple circuit sketch for the instrument. Each sensor was calibrated such that the voltages read by the sensors corresponded to a measured height between the sensor and the metal inductance plate (placed above the clay pellet, Figure 7.2(a)). The calibration distances were then loaded into a LabVIEW script so that the raw data was mapped and scaled using these values to turn the voltage readings into a distance. The distances recorded needed inverting since the actual distance measured by the sensor decreased as the compacted disk increased in height. This final plotted distance is presented as an increasing uniaxial swelling height as a function of time. Using the data obtained from 2M $HMDA_{(aq)}$ measurements, the initial rate of the linear portion of the swelling has been calculated using an ordinary least squares calculation for two identical samples. This has been used as a primary guide as to the error within the measurements also encompassing human error.

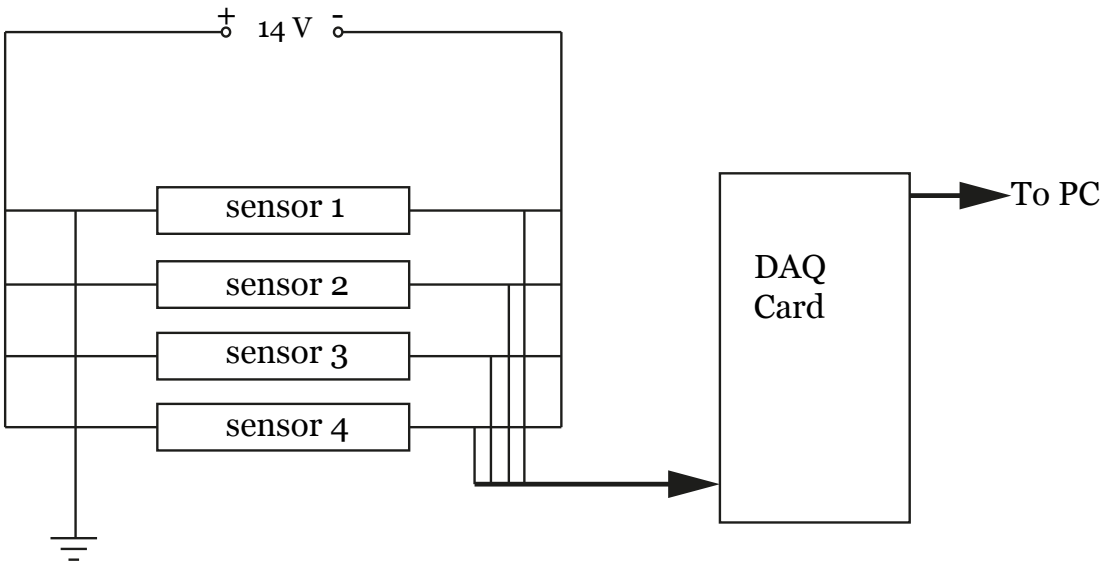


Figure 7.3: Sketch of circuit diagram for simultaneous measurements using four non-contact linear displacement sensors in the "swellometer".

| Species | $Li^+$ | $Na^+$ | $K^+$ | $TMA^+$ | $HMDA^{2+}$ |
|---|---|---|---|---|---|
| $\sim$ *d*-spacing Å | 14.0 | 14.2 | 10.1 | 14.6 | 13.5 |

Table 7.2: Approximate *d*-spacings for the exchanged vermiculites used to make the compacted clay samples for the macroscopic swelling experiments. These are taken from the peak position of the furthest peak to the right of each XRD pattern in Figure 7.4(b).

### 7.0.2 XRD Analysis of Exchanged Samples

Figure 7.4 shows the XRD patterns of the milled, exchanged vermiculites after drying in the oven at 80°C overnight and then equilibrating to lab humidity for 24 hours. The scans were taken with a stepsize of 0.02 degrees and 10 s scan time at each step. The datasets are shifted vertically for ease of viewing. The Na-vermiculite has a high low-$Q$ scattering and is not as clean as the other XRD patterns due to amorphous material in the sample. This is due to not having washed the excess $NaCl_{(aq)}$ from the clay adequately post final exchange, however this does not affect the measurement of the *d*-spacing. Figure 7.4(b) shows the *d*-spacing measurements of the Li-as received and the subsequently exchanged vermiculites which is the is the first peak on the left of each XRD peak pattern and converted into $d$ via Bragg's law.

Table 7.2 lists the approximate measured *d*-spacing, (001) peak of the exchanged vermiculites. The peaks were not fit to obtain their precise location however the XRD was

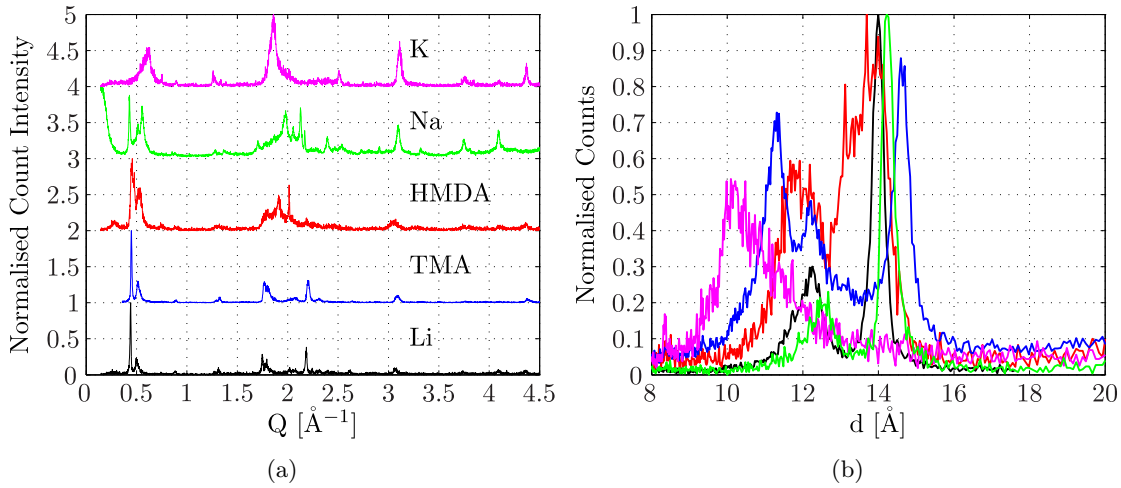


Figure 7.4: **(a)** XRD of the exchanged vermiculite clay. (001) peak is the first peak on the left. **(b)**: Focus on XRD showing $d$-spacing of the exchanged vermiculite clay according to Bragg's law conversion from $Q$ to $d$. — $Na^+$, — $K^+$, — $TMA^+$, — $HMDA^{2+}$, — $Li^+$

performed in order to gauge whether exchange had occurred specifically in the case of HMDA since we did not observe exchange in the high pressure HMDA flooding of Li-vermiculite. We believe the HMDA has exchanged since distances match with those give from Suter *et al*[43].

### 7.0.3 Results and Discussion

Preliminary measurements on the uniaxial swelling of compacted as received $Li^+$-vermiculite, $Na^+$, $K^+$, $TMA^+$ exchanged and HMDA exchanged vermiculite in water are shown in Figure 7.5.

The first thing to note is the discontinuities present in some of the data sets. In Figure 7.5 it is for the Li- and K-exchanged vermiculite. This is because there are no cohesive interactions between the clay platelets and due to the high layer charge, there is a sharp drop of the electric double layer which means it does not extend greatly towards the neighbouring platelets. Whereas conversely, smoother swelling curves are observed for montmorillonites due to the self-sealing property they have[44]. As water is absorbed into the pores pushing the clay platelets apart, the weight of the metal inductance plate on top of the compacted clay is occasionally enough to overcome the pore pressure as water is drawn into the clay and the platelets move outwards. This is especially evident in the $Na^+$ data as we see a decrease in height after the maximum is reached at which point there is no outward pore pressure and the dominant force on the clay is the mass of the inductance

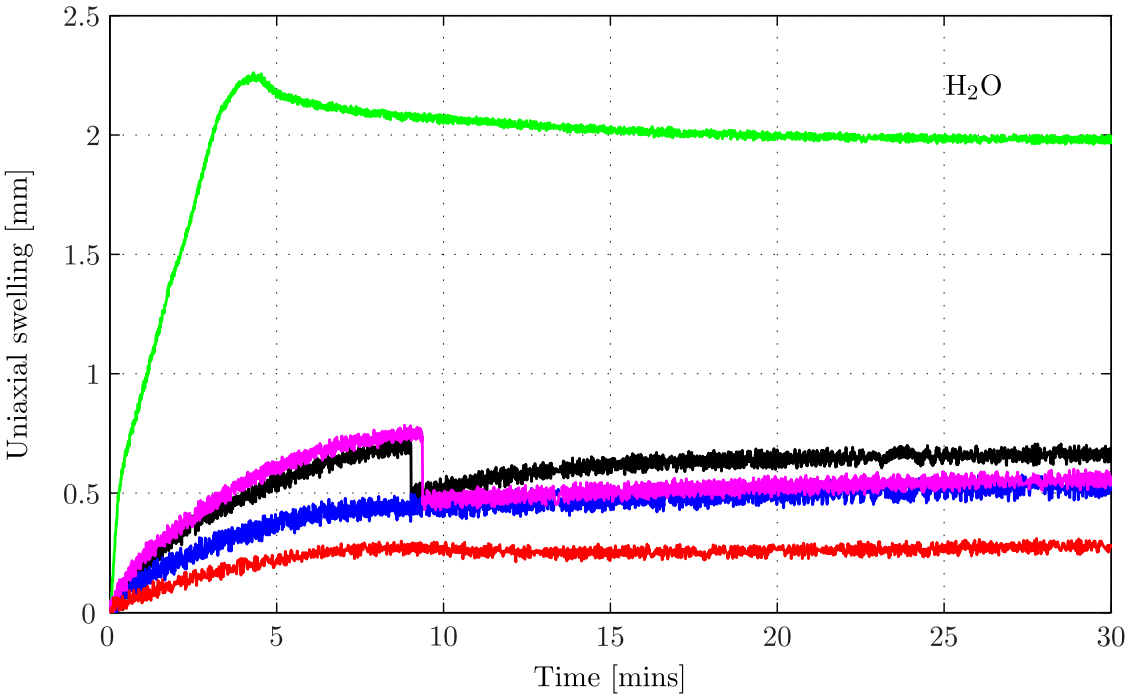


Figure 7.5: Uniaxial expansion (along $z$-axis) of the vermiculite with varying interlayer composition: — $Na^+$, — $K^+$, — $TMA^+$, — $HMDA^{2+}$, — $Li^+$ in test fluid of distilled water. Note the enhanced inhibitive effect of the $TMA^+$ and $HMDA^{2+}$ compared to $K^+$ on the overall swelling response of the clay.

plate pushing down on the compacted clay disk. Conversely to the high pressure and temperature neutron study on the TMA-vermiculite, a macroscopic height increase is observed in the presence of water. This is observed for all the exchanged vermiculites and is attributed to the capillary effect of having air in pore spaces. We observe less overall macroscopic swelling for the HMDA- and TMA-exchanged vermiculites than we do for the K-vermiculite indicating that although the $K^+$ has the lowest enthalpy of hydration (this has not been measured for HMDA), this is not the only contributing factor to the swelling of the mineral as has previously been focussed on[33–36]. The hydrophobicity of the molecules must therefore also contribute[43].

The $Na^+$ exchanged vermiculite also shows a very clear two step swelling profile in the initial stages. During compaction, pore sizes generated increase from centre to the outer edge of the disk[146] and therefore it is inferred that the swelling should occur in a two step process: faster as the outer-larger pores fill and then slower as the inner-smaller pores fill.

Figure 7.6 shows the macroscopic swelling of the Li- and TMA-vermiculite in brine solution at seawater concentration of 0.4M NaCl and at 0.75M NaCl. At seawater concentration we observe an overall slower initial expansion rate and overall less smaller height

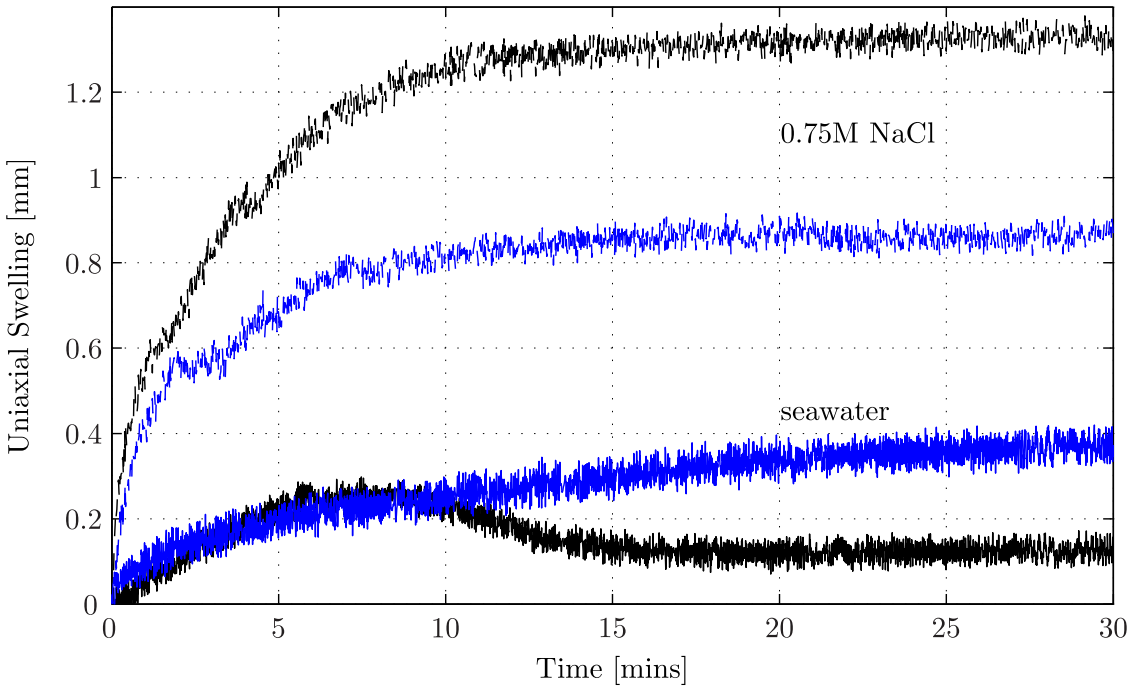


Figure 7.6: Uniaxial expansion of — $TMA^+$ and — $Li^+$ in test fluid of NaCl at seawater concentration (solid line) and 0.75M NaCl (dashed line).

change compared to the 0.75M brine solution. If we consider the process to be osmotic then we can expect greater expansion observed for the higher concentration test fluid. 0.75M brine concentration was chosen since at this concentration, interlayer expansion [18] of the clay mineral is eliminated however an overall height increase of ∼40 % of the original height of the clay disk is observed. Despite this, the effects of the TMA are still felt, since less swelling is measured for the $TMA^+$ than the $Li^+$ indicating that there is some effects of the interlayer which bleed into the macroscopic swelling that we observe.

The final example of macroscopic swelling of compacted clay samples is shown in Figure 7.7 of Li-vermiculite in 2M $HMDA_{(aq)}$ designed to observe the macroscopic swelling of the same materials used for the high pressure experiment in Section 5.2. Both data sets are for the Li-vermiculite and compacted in the same manner. A dramatic macroscopic expansion of the compacted clay is observed for both with a linear initial expansion rate. From Figures 7.6 and 7.7, we observe an increasing initial expansion rate with increasing solute concentration of the test fluid to almost a linear initial expansion rate.

This chapter presents the bespoke instrument designed to measure the uniaxial swelling of compacted clay samples and a preliminary set of results investigating variation of interlayer cation in the presence of water and test fluids of brine and $HMDA_{(aq)}$.

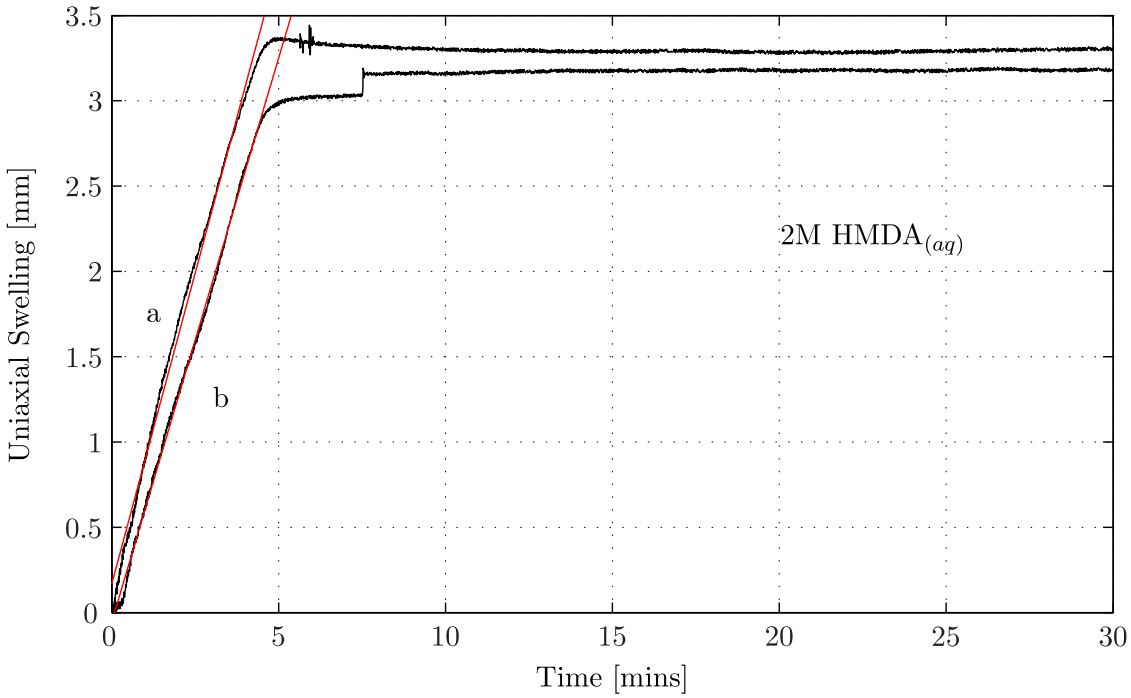


Figure 7.7: Uniaxial expansion of Li-vermiculite in test fluid of 2M HMDA$_{(aq)}$. Two swelling curves are plotted to highlight the repeatability of the measurements. — $Li^+$ data and — $y = m_i x + c$ fit to linear portion of swelling curve.

| $i$ | $m_i$ mm min$^{-1}$ | r$^2$ |
|---|---|---|
| a | 0.6612 | 0.99 |
| b | 0.7292 | 0.99 |

Table 7.3: Comparison of gradients $m_i$ (in mm ) from fitting linear regression using ordinary least squares calculation to linear portion of the swelling curves in Figure 7.7. According to the square of the correlation coefficients r$^2$, we observe quite good fits and a ratio of $\frac{m_a}{m_b} = 0.91$. I.e. the data are within 10%.

The data indicates that the instrument is robust and does allow for repeatable measurements within a $\sim$ 10 % error and it can be used for systematic tests on any compacted swelling clay whether natural or synthetic and test fluid-inhibitor systems. This repeatability includes the contribution of human error involved when compacting the samples and sample loss in the die alongside the variation incurred during the synthesis of the compacted samples from uneven mixing and different pore-size distributions. Although not shown directly here, the instrument allows for humidity controlled measurements and improves on existing instruments measuring height change of compacted clays in that non-contact sensors are used.

The swelling data from all the results show that regardless of the fluid chosen and the interlayer cation present, a macroscopic expansion is measured for all the clay samples. A possible two-step swelling profile is observed due to the nature of the pore distribution in the compacted sampled during compaction[146]. We also observe a macroscopic expansion when the interlayer expansion is known to be suppressed although the type of interlayer cation does affect the initial rate and overall expansion of the material. We believe this to be an interplay between the hydration enthalpy of the interlayer counterion and in the case of the $TMA^+$ and $HMDA^2+$ the hydrophobicity of the ions[43].

# Chapter 8

# Conclusions

The work presented in this thesis is the first investigation into the coupled effect of temperature and pressure, conditions like those found in the wellbore, on the liquid structure of organo-amine and ammonium compounds and their ability to act as clay swelling inhibitors at these conditions in the crystalline regime. The initial aim of the liquid structure investigations was to see if there were any hydrophobic interactions an ion-pairing at the elevated pressure and temperature conditions since this would be unfavourable for clay swelling inhibition. This was then linked to the crystalline and macroscopic swelling of the clay minerals either exchanged with or in the presence of the organo-amine compounds. Since we observed a disparity between the clay swelling data in the mico- and macro-scales, we performed a 'proof of concept' investigation into whether spin-echo small angle neutron scattering is a viable technique to look at pore-swelling of compacted clays. Finally we investigated the dynamics of water and terephthalate diffusion between expanded, relatively unreactive mineral sheets since the literature showed that even the non-swelling minerals pose problems down-hole.

The liquid neutron diffraction data of 1-molar TMACl in $D_2O$ at oil well conditions revealed that with the addition of the TMA salt, there is an increased inter-solvent structure compared to bulk. This is ascribed to the very slight reorientation of the solvent $D_2O$ around the TMA ions however the perturbation of the ion is small since the bulk hydrogen-bond network is maintained. We observed that the externally applied temperature and pressure act in opposition to each other: pressure reduces distances between

molecules and temperature increases them. Therefore in systems such as the TMA solution where the perturbation of the salt is minimal to the intersolvent structure compared to bulk, the pressure and temperature effects are not felt to such a great extent. The data also revealed that $TMA^+$ and $Cl^-$ exist as solvent separated pairs throughout increasing p & T conditions and do not ion pair (salting-in). Neither do we observe any hydrophobic clustering of $TMA^+$ (salting-out), in fact we see solute ions being pushed apart. This is attributed to the size of the TMA ion which is relatively large and therefore there is minimal binding to the water molecules. MD simulations have shown that there is no excess chemical potential in the TMA solutions therefore no preference for salting-in or salting-out is observed[147].

The liquid diffraction data for 2 molar HMDA solution reveals a very highly ordered intersolvent structure which can be considered ice-like since the water RDFs resemble those of ice and the coordination numbers in the HMDA solution are less than for bulk. The hydrophobicity of the molecule has yet to be probed and simulations determining the spherical density plots are ongoing.

The high pressure and temperature investigations into the crystalline swelling of TMA-vermiculite and Li-vermiculite in the presence of $D_2O$ and 2 molar HMDA solution revealed that cation exchange does not need to occur in order for a clay swelling inhibitor to minimise the crystalline swelling of the mineral. Both of the clays are structurally stable as a 2-waterlayer hydrate at these conditions. Similarly, for both clays we measured an initial expansion of the *d*-spacing with introduction of water into the system to a probable 2-water layers[43,136] however no further swelling was observed. MD simulations of TMA-smectite attribute the lack of clay expansion due to unfavourable interactions of the water with the hydrophobic molecule[43] since if solely hydration energies are taken into consideration, expansion should occur beyond the observed. However our liquid diffraction of aqueous TMA solution showed a minimal perturbation of the TMA to the water and a cage like water structure around the ion allowing hydrogen bond networking to remain. The reason for the lack of expansion is therefore attributed to a change in the hydration energy due to vermiculites having higher layer charge and therefore TMA ions reside closer to the sheets. For the Li-vermiculite, we do not observe exchange of lithium with HMDA since we do not observe a *d*-spacing increase corresponding to HMDA-exchanged clay[43] but argue that the HMDA sits on the surfaces of the clay sheets and that the hydrophobic backbone makes interaction with the water unfavourable and therefore acts as a barrier

for the water entering the clay.

Performing macroscopic measurements with methods used in Chapter 7, is an important comparison to the microscopic swelling data. It is common in the field to identify the total swelling response of the clay by overall expansion of these compacted clay samples subjected to water and drilling fluid submersion. The data from the macroscopic swelling experiments indicate that the instrument designed is robust and reliable allowing for repeatable measurements within a $\sim$ 10 % error. The swelling data from all the results show that regardless of the fluid chosen and the interlayer cation present, a macroscopic expansion is measured for all the clay samples. We also observe a macroscopic expansion when the interlayer expansion is known to be suppressed although the type of interlayer cation does affect the initial rate and overall expansion of the material. The outcome of these experiments highlights that although cation exchange is *a* solution to overcome the problem of clay swelling in the oilfield, the expansion in the pore spaces *cannot* be neglected.

Since tests on recompaction of mined clays is still the primary method for measuring macroscopic clay swelling behaviour, we performed a 'proof of concept' investigation into whether spin-echo small angle neutron scattering is a viable technique to look at the pore-swelling of these compacted clay samples. Despite measuring relatively high scattering from the system, we were able to observe for the first time with resolution from 150 nm to 15. $\mu m$, that overall, the larger of the pores filled before the smaller ones. Although an intuitive assumption, it highlights the fact that the drilling fluid must pass through the larger macro- and meso-pores before arriving at the interlayer. This would therefore shift the locus of the clay swelling problem to the pore spaces, allowing more refined targeting of the the larger pores by the swelling inhibitors[51] corroborating out macroscopic swelling experiments.

The QENS measurements made on the diffusion of terephthalate and water in hydrated layered double hydroxides show that water content has a substantial effect on the motion of the anion and overall mobility of the water. At lower water content only rotation of the water molecules are observed at maximum temperature of 320 K and below this temperature no rotational or translational motion is observed. Increasing the water content to 1:16.24 TA:water, allows for full mobility of the water molecules. We found that the terephthalate did not contribute to the translational motion in the system and coupled with the water can only contribute to the overall rotation corroborating NMR

studies showing that the terephthalate can only reorient within the interlayer and not translate[148]. We are able to resolve the freezing out of the water motion: full translation between 280 and 320 K however again only rotation at 260 K and no rotation or translational motion below this temperature. The $D_{trans}$ is measured for our data at 280 k and 320 K: $D_{trans}$ 3.4 $\times 10^{-9}$ $m^2s^{-1}$ and 6.0 $\times 10^{-9}$ $m^2s^{-1}$ respectively for the higher water content sample. This shows that water can move faster than in bulk at 295 K[10] and attributed to the minimal interactions of the terephthalate and water and the increased gallery spacing as the higher water content pushes the sheets apart allowing the TA to act as pillars.

## 8.1 Future Work

Our data for the 2 molar $HMDA_{(aq)}$ looks very promising in that at a concentration of 1:28 water:HMDA, we expect to observe some hydrophobic ordering. Also since the molecule is hygroscopic, investigations into the enthalpic and entropic considerations of the dissolution of the HMDA would especially aid in discerning the mechanism of solvation. More information on the diffusion of HMDA in bulk and within the clay interlayers is needed to ascertain whether exchange is favourable at the conditions of the well pore and how much of a role the porosity of the material plays in whether this exchange can occur since the HMDA molecule is bulky and in water we observe this 'ice-like' structure. Therefore I would propose QENS studies on HMDA-exchanged smectites and vermiculites and also if possible QENS on compacted HMDA-exchanged clays.

The spin-echo experiment was very much a test investigation since the spin-echo SANS technique has not previously been used on compacted clay samples and it is clear that optimisation of the sample and experiment is required. Similarly, due to the complex nature of the clay, using natural sample as opposed to pure synthetic and the lack of control over the pore distribution induced during compaction, fitting of the data is very difficult. Many different fractal models can be used to fit the data but focus on making thinner samples and minimising fluid in the beam would prove most efficient at reducing scatter from the sample and improving the experiment. Once optimised, this could be linked with neutron imaging of fluid invasion into the compacted sample using selective isotopic substitution on the various parts of the clay-water-inhibitor system. We did submit proposals to do this experiment but unfortunately beam time was not awarded.

In terms of the oil-field applications, the instrument designed in Chapter 7 can be used for a plethora of further tests of the effectiveness of inhibitor-fluids. I think here a systematic investigation into the swelling behaviour of these compacted samples as a function of fluid viscosity and dielectric constant and surface tension map of polar and non-polar solvents. This is so that we can try and relate the bulk properties of the clay to the surface interaction of the platelets and the fluids i.e. making and breaking interfacial tension of the clay-air and clay-fluid surfaces which I think should be explored within the clay swelling regime.

# Appendix A

# Appendix A

## A.1 Detection of Non-contact Sensors

The detection method of the sensors is based on inductance. The sensor contains a coil of segment length $\mathrm{d}l$, through which a current $I$ is passed and a magnetic field $B$ is generated according to Amps Law. We can find the magnitude of the field at a radial distance $\vec{r}$ from the coil by integrating the Biot-Savart Law:

$$\vec{B}(\vec{r}) = \int \mathrm{d}\vec{B} = \frac{\mu_0 I}{4\pi} \int \frac{I\,\mathrm{d}\vec{l} \times \vec{r}}{r^3} \tag{A.1}$$

The sensor contains an oscillator within the circuitry to constantly flip the polarity of the applied current at a frequency of 500Hz which in turn causes a constant changing $B$ field, $\frac{\mathrm{d}\Phi_B}{\mathrm{d}t}$ ($\Phi_B$ is the magnetic flux). When a metal object is placed close to the sensor, the oscillating field from the coil induces eddy currents in the metal according to Lenz' Law:

$$Emf = \frac{\mathrm{d}\Phi_B}{\mathrm{d}t} = -L\frac{\mathrm{d}I}{\mathrm{d}t} \tag{A.2}$$

the $Emf$ is the electro motive force (energy) induced and $L$ is the 'inductance' in the metal object. Since the induced current is also changing, we reverse engineer a $\frac{\mathrm{d}\Phi_B metal}{\mathrm{d}t}$ of the metal object which is detected in the sensor by another coil (set of coils) and is proportional to the distance of the metal object. We can therefore calibrate the sensors such that the measured voltages converts to distance from the sensor.

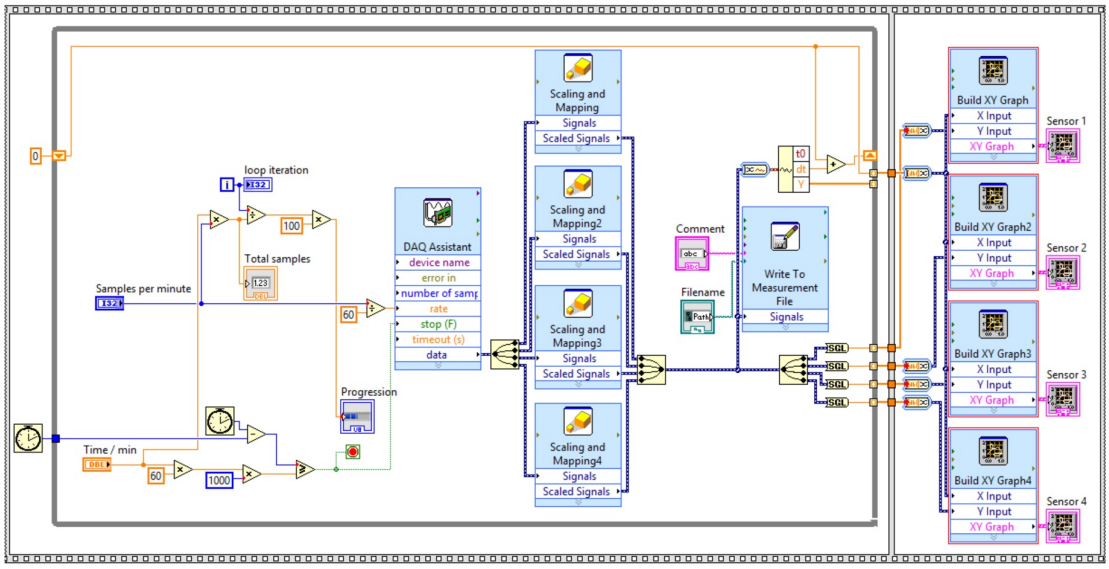


Figure A.1: Full circuit block diagram for LabVIEW code used to take a measurement from the swellometer.

## A.2 Recording Measurements on Swellometer

Figure A.1 is a screenshot of the graphical LabVIEW code written for taking measurements simultaneously with the four sensors within the swellometer. It incorporates the scaling and calibration required to have an output conversion from voltage to distance given from the sensors.

# Bibliography


[1] D. Cebula, R. Thomas, S. Middleton, R. Ottewill, and J. White, "Neutron diffraction from clay-water systems," *CLAYS CLAY MINER. Clays Clay Miner.*, vol. 27, no. 1, p. 39, 1979.

[2] B. Willis and C. Carlile, *Experimental Neutron Scattering*. Oxford University Press, 2009.

[3] A. Pietropaolo and R. Senesi, "Electron volt neutron spectrometers," *Physics Reports*, vol. 508, no. 3, pp. 45 – 90, 2011.

[4] D. Bowron, A. Soper, K. Jones, S. Ansell, S. Birch, J. Norris, L. Perrott, D. Riedel, N. Rhodes, S. Wakefield, *et al.*, "Nimrod: The near and intermediate range order diffractometer of the isis second target station," *Review of Scientific Instruments*, vol. 81, no. 3, p. 033905, 2010.

[5] Science and T. F. Council, "Offspec instrument," October 2015.

[6] Science and T. F. Council, "Modes software," September 2015.

[7] ©The Royal Society of Chemistry 2006, "Enthalpies of hydration," 2006.

[8] S. Lovesey, *Theory of Neutron Scattering from Condensed Matter*. Oxford University Press, 1984.

[9] N. C. for Neutron Research, "Neutron scattering lengths and cross sections," January 2013.

[10] J. Swenson, R. Bergman, and W. S. Howells, "Quasielastic neutron scattering of two-dimensional water in a vermiculite clay," *The Journal of Chemical Physics*, vol. 113, no. 7, 2000.

[11] R. E. Grim, G. Kulbicki, and A. V. Carozzi, "Clay minerology of the sediments of the great salt lake, utah," *Bulletin of the Geological Society of America*, vol. 71, pp. 515–520, 1960.

[12] M. J. Wilson, "The origin and formation os clay minerals in soils; past, present and future perspectives," *Clay Minerals*, vol. 34, pp. 7–25, 1999.

[13] G. Brindley and G. Brown, *Crystal Structures of Clay Minerals and Their X-ray Identification*. Mineralogical Society, 1980.

[14] F. North, *Petroleum Geology*. Unwin Hyman, 1990.

[15] D. Eberl, "The reaction of montmorillonite to mixed-layer clay: the effect of interlayer alkali and alkaline earth cations," *Geochimica et Cosmochimica Acta*, vol. 42, no. 1, pp. 1–7, 1978.

[16] A. Inoue, A. Meunier, G. Touchard, and B. Velde, "Mechanism of illite formation during smectite-to-illite conversion in a hydrothermal system," *American Mineralogist*, vol. 73, no. 11-12, pp. 1325–1334, 1988.

[17] D. Eberl, B. Velde, and T. McCormick, "Synthesis of illite-smectite from smectite at earth surface temperatures and high ph," *Clay Minerals*, vol. 28, pp. 49–49, 1993.

[18] K. Norrish, "The swelling of montmorillonite," *Discuss. Faraday Soc.*, vol. 18, pp. 120–134, 1954.

[19] A. Newman, *Chemisrty of Clays and Clay Minerals*. Mineralogical Society, 1987.

[20] D. Fink and G. Thomas, "X-ray studies of crystalline swelling in montmorillonites.," *Soil Science Society of America Journal*, vol. 28, pp. 747–750, 1964.

[21] E. J. M. Hensen and B. Smit, "Why clays swell," *The Journal of Physical Chemistry B*, vol. 106, no. 49, pp. 12664–12667, 2002.

[22] G. Sposito, N. T. Skipper, R. Sutton, S.-h. Park, A. K. Soper, and J. A. Greathouse, "Surface geochemistry of the clay minerals," *Proceedings of the National Academy of Sciences*, vol. 96, no. 7, pp. 3358–3364, 1999.

[23] P. Slade, J. Quirk, and K. Norrish, "Crystalline swelling of smectite samples in concentrated nacl solutions in relation to layer charge," *Clays and Clay Minerals*, vol. 39, no. 3, pp. 234–238, 1991.

[24] F. Santarelli and S. Carminati, "Do shales swell?," *Society of Petroleum Engineers*, vol. SPE/IADC29421, pp. 741–756, 1995.

[25] A. V. de Siqueira, C. Lobban, N. T. Skipper, G. D. Williams, A. K. Soper, R. Done, J. W. Dreyer, R. J. Humphreys, and J. A. R. Bones, "The structure of pore fluids in swelling clays at elevated pressures and temperatures," *Journal of Physics: Condensed Matter*, vol. 11, no. 47, p. 9179, 1999.

[26] D. Laird, "Influence of layer charge on swelling of smectites," *Applied clay science*, vol. 34, no. 1, pp. 74–87, 2006.

[27] D. E. O'Brien, M. E. Chenevert, *et al.*, "Stabilizing sensitive shales with inhibited, potassium-based drilling fluids," *Journal of Petroleum Technology*, vol. 25, no. 09, pp. 1–089, 1973.

[28] C. Carpacho, M. Ramirez, J. Osorio, and P. Kenny, "Replacing potassium with aluminum complex overcomes wellbore instability problems in kaolinitic shales in south america," *Texas, Abril*, 2004.

[29] E. Van Oort, "On the physical and chemical stability of shales," *Journal of Petroleum Science and Engineering*, vol. 38, no. 3, pp. 213–235, 2003.

[30] T. a. Geehan, "Reducing the oilfield's environmental footprint," *Oilfield Review2*, vol. 4, pp. 53–63, 1990.

[31] E. S. Boek, P. V. Coveney, and N. T. Skipper, "Monte carlo molecular modeling studies of hydrated li-, na-, and k-smectites: Understanding the role of potassium as a clay swelling inhibitor," *Journal of the American Chemical Society*, vol. 117, no. 50, pp. 12608–12617, 1995.

[32] R. Anderson, I. Ratcliffe, H. Greenwell, P. Williams, S. Cliffe, and P. Coveney, "Clay swelling  a challenge in the oilfield," *Earth-Science Reviews*, vol. 98, no. 34, pp. 201 – 216, 2010.

[33] V. A. Colten-Bradley, "Role of pressure in smectite dehydration–effects on geopressure and smectite-to-illite transformation," *AAPG Bulletin*, vol. 71, no. 11, pp. 1414–1427, 1987.

[34] W.-L. Huang, W. A. Bassett, and T.-C. Wu, "Dehydration and hydration of montmorillonite at elevated temperatures and pressures monitored using synchrotron radiation," *American Mineralogist*, vol. 79, no. 7-8, pp. 683–691, 1994.

[35] T.-C. Wu, W. Bassett, W.-L. Huang, S. Guggenheim, and A. Koster Van Groos, "Montmorillonite under high h2o pressures: Stability of hydrate phases, rehydration hysteresis, and the effect of interlayer cations," *American Mineralogist*, vol. 82, no. 1-2, pp. 69–78, 1997.

[36] N. Skipper, G. Williams, A. De Siqueira, C. Lobban, and A. Soper, "Time-of-flight neutron diffraction studies of clay-fluid interactions under basin conditions," *Clay Minerals*, vol. 35, no. 1, pp. 283–290, 2000.

[37] V. A. Colten, "Hydration states of smectite in nacl brines at elevated pressures and temperatures," *Clays and Clay Minerals*, vol. 34, no. 4, pp. 385–389, 1986.

[38] A. V. de Siqueira, N. T. S. P. V. C. BOEK, and E. S, "Computer simulation evidence for enthalpy driven dehydration of smectite clays at elevated pressures and temperatures," *Molecular Physics*, vol. 92, no. 1, pp. 1–6, 1997.

[39] L. De Pablo, M. Chávez, A. Sum, and J. De Pablo, "Monte carlo molecular simulation of the hydration of na–montmorillonite at reservoir conditions," *The Journal of chemical physics*, vol. 120, no. 2, pp. 939–946, 2004.

[40] D. A. Young, , and D. E. Smith*, "Simulations of clay mineral swelling and hydration: dependence upon interlayer ion size and charge," *The Journal of Physical Chemistry B*, vol. 104, no. 39, pp. 9163–9170, 2000.

[41] G. Odriozola*, , and F. de J. Guevara-Rodrguez, "Na-montmorillonite hydrates under basin conditions: hybrid monte carlo and molecular dynamics simulations," *Langmuir*, vol. 20, no. 5, pp. 2010–2016, 2004.

[42] M. Smalley, R. Thomas, L. Braganza, and T. Matsuo, "Effect of hydrostatic pressure on the swelling of n-butylammonium vermiculite," *Clays and Clay Minerals*, vol. 37, no. 5, pp. 474–478, 1989.

[43] J. Suter, P. Coveney, R. Anderson, H. Greenwell, and S. Cliffe, "Rule based design of clay-swelling inhibitors," *Energy & Environmental Science*, vol. 4, no. 11, pp. 4572–4586, 2011.

[44] H. Komine and N. Ogata, "Prediction for swelling characteristics of compacted bentonite," *Canadian Geotechnical Journal*, vol. 33, no. 1, pp. 11–22, 1996.

[45] P. Wersin, L. Johnson, and I. McKinley, "Performance of the bentonite barrier at temperatures beyond 100 c: A critical review," *Physics and Chemistry of the Earth, Parts A/B/C*, vol. 32, no. 814, pp. 780 – 788, 2007. Clay in natural and engineered barriers for radioactive waste confinement - Part 2.

[46] L. Schmitt, T. Forsans, and F. Santarelli, "Shale testing and capillary phenomena," in *International journal of rock mechanics and mining sciences & geomechanics abstracts*, vol. 31, pp. 411–427, Elsevier, 1994.

[47] H. Santos, A. Diek, S. Da Fontoura, and J. Roegiers, "Shale reactivity test: a novel approach to evaluate shale-fluid interaction," *International Journal of Rock Mechanics and Mining Sciences*, vol. 34, no. 3, pp. 268–e1, 1997.

[48] B. Singh and R. Gilkes, "An electron optical investigation of the alteration of kaolinite to halloysite," *Clays and Clay Minerals*, vol. 40, no. 2, pp. 212–229, 1992.

[49] H. Zhong, Z. Qiu, W. Huang, and J. Cao, "Shale inhibitive properties of polyether diamine in water-based drilling fluid," *Journal of Petroleum Science and Engineering*, vol. 78, no. 2, pp. 510 – 515, 2011.

[50] H. Y. Zhong, Z. S. Qiu, W. A. Huang, J. Cao, F. W. Wang, and B. Q. Xie, "Inhibition comparison between polyether diamine and quaternary ammonium salt as shale inhibitor in water-based drilling fluid," *Energy Sources, Part A: Recovery, Utilization, and Environmental Effects*, vol. 35, no. 3, pp. 218–225, 2013.

[51] M. Wilson and L. Wilson, "Clay mineralogy and shale instability: an alternative conceptual analysis," *Clay Minerals*, vol. 49, no. 2, pp. 127–145, 2014.

[52] J. Quirk and L. Aylmore, "Domains and quasi-crystalline regions in clay systems," *Soil Science Society of America Journal*, vol. 35, no. 4, pp. 652–654, 1971.

[53] B. Velde, *Introduction to clay minerals: chemistry, origins, uses, and environmental significance*. Chapman & Hall, 1992.

[54] B. K, "Clay mineral diagenesis in sedimentary basins - a key to the prediction of

rock properties. examples from the north sea basin," *Clay Minerals*, vol. 33, no. 1, pp. 15–34, 1998.

[55] E. Roaldset, H. Wei, and S. Grimstad, "Smectite to illite conversion by hydrous pyrolysis," *Clay Minerals*, vol. 33, no. 1, pp. 147–158, 1998.

[56] G. Sposito and R. Prost, "Structure of water adsorbed on smectites," *Chemical Reviews*, vol. 82, no. 6, pp. 553–573, 1982.

[57] R. Pashley and J. Quirk, "The effect of cation valency on dlvo and hydration forces between macroscopic sheets of muscovite mica in relation to clay swelling," *Colloids and surfaces*, vol. 9, no. 1, pp. 1–17, 1984.

[58] K. Tamura, H. Yamada, and H. Nakazawa, "Stepwise hydration of high-quality synthetic smectite with various cations," *Clays and Clay Minerals*, vol. 48, no. 3, pp. 400–404, 2000.

[59] R. Mooney, A. Keenan, and L. Wood, "Adsorption of water vapor by montmorillonite. ii. effect of exchangeable ions and lattice swelling as measured by x-ray diffraction," *Journal of the American Chemical Society*, vol. 74, no. 6, pp. 1371–1374, 1952.

[60] D. Laird, "Layer change influences on the hydration of expandable 2: 1 phyllosilicates.," *Clays and Clay Minerals*, vol. 47, no. 9, pp. 630–636, 1999.

[61] S. Hendricks, R. Nelson, and L. Alexander, "Hydration mechanism of the clay mineral montmorillonite saturated with various cations1," *Journal of the American Chemical Society*, vol. 62, no. 6, pp. 1457–1464, 1940.

[62] J. Cases, I. Bérend, G. Besson, M. Francois, J. Uriot, F. Thomas, and J. Poirier, "Mechanism of adsorption and desorption of water vapor by homoionic montmorillonite. 1. the sodium-exchanged form," *Langmuir*, vol. 8, no. 11, pp. 2730–2739, 1992.

[63] D. Laird, C. Shang, and M. Thompson, "Hysteresis in crystalline swelling of smectites," *Journal of colloid and interface science*, vol. 171, no. 1, pp. 240–245, 1995.

[64] T. Tambach, P. Bolhuis, E. Hensen, and B. Smit, "Hysteresis in clay swelling induced

by hydrogen bonding: accurate prediction of swelling states," *Langmuir*, vol. 22, no. 3, pp. 1223–1234, 2006.

[65] Y. Zheng, A. Zaoui, and I. Shahrour, "A theoretical study of swelling and shrinking of hydrated wyoming montmorillonite," *Applied Clay Science*, vol. 51, no. 12, pp. 177 – 181, 2011.

[66] T. Sato, T. Watanabe, and R. Otsuka, "Effects of layer charge, charge location, and energy change on expansion properties of dioctahedral smectites," *Clays and Clay Minerals*, vol. 40, no. 1, pp. 103–113, 1992.

[67] Y. Nagano, M. Sakiyama, T. Fujiwara, and Y. Kondo, "Thermochemical study of tetramethyl-and tetraethylammonium halides: nonionic cohesive energies in the crystals and hydration enthalpies of the cations," *The Journal of Physical Chemistry*, vol. 92, no. 20, pp. 5823–5827, 1988.

[68] W. G. Garret and G. F. Walker, "Swelling of some vermiculite-organic complexes in water," *Clays and Clay Minerals*, vol. 9, pp. 557–567, 1962.

[69] R. A. Vaia, R. K. Teukolsky, and E. P. Giannelis, "Interlayer structure and molecular environment of alkylammonium layered silicates," *Chemistry of Materials*, vol. 6, no. 7, pp. 1017–1022, 1994.

[70] G. Williams, N. Skipper, M. Smalley, A. Soper, and S. King, "Structure of alkyl ammonium solutions in vermiculite clays," *Faraday Discussions*, vol. 104, pp. 295–306, 1996.

[71] M. Alexandre and P. Dubois, "Polymer-layered silicate nanocomposites: preparation, properties and uses of a new class of materials," *Materials Science and Engineering: R: Reports*, vol. 28, no. 12, pp. 1 – 63, 2000.

[72] R. Crawford, M. Smalley, and R. Thomas, "Swelling of n-butylammonium vermiculite in water," *Clays and Clay Minerals*, vol. 38, no. 1, pp. 90–96, 1990.

[73] T. Sasaki and M. Watanabe, "Osmotic swelling to exfoliation. exceptionally high degrees of hydration of a layered titanate," *Journal of the American Chemical Society*, vol. 120, no. 19, pp. 4682–4689, 1998.

[74] N. T. Skipper, M. V. Smalley, G. D. Williams, A. K. Soper, and C. H. Thompson, "Direct measurement of the electric double-layer structure in hydrated lithium vermiculite clays by neutron diffraction," *The Journal of Physical Chemistry*, vol. 99, no. 39, pp. 14201–14204, 1995.

[75] O. Stern, "Zur theorie der electrolytischen doppelshicht," *Z. Elektrochem.*, vol. 30, pp. 203–224, 1924.

[76] E. Verwey, J. Overbeek, and K. Van Nes, *Theory of the stability of lyophobic colloids: the interaction of sol particles having an electric double layer*. Elsevier New York, 1948.

[77] B. Derjaguin and L. Landau, "Theory of the stability of strongly charged lyophobic sols and of the adhesion of strongly charged particles in solutions of electrolytes," *Progress in Surface Science*, vol. 43, no. 14, pp. 30 – 59, 1993.

[78] S. Guggenheim and A. K. van Groos, "An integrated experimental system for solid-gas-liquid environmental cells," *Clays and Clay Minerals*, vol. 62, no. 6, pp. 470–476, 2014.

[79] H. Darley and G. Gray, *Composition and Properties of Drilling and Completion Fluids*. Gulf Publishing, 2011.

[80] Health and S. Executive, "Drilling fluids composition and use within the uk offshore drilling industry," 1999.

[81] M. Thatcher, M. Robson, L. R. Henriquez, C. C. Karman, and G. Payne, "Charm, chemical hazard assessment and risk management," Feb 2005.

[82] E. Malachosky, B. Shannon, J. Jackson, and W. Aubert, "Offshore disposal of oil-based drilling-fluid waste: An environmentally acceptable solution," *SPE Drilling & Completion*, vol. 8, no. 4, pp. 283–287, 1993.

[83] R. Caenn and G. V. Chillingar, "Drilling fluids: State of the art," *Journal of Petroleum Science and Engineering*, vol. 14, no. 34, pp. 221 – 230, 1996.

[84] J. Davies, J. Addy, R. Blackman, J. Blanchard, J. Ferbrache, D. Moore, H. Somerville, A. Whitehead, and T. Wilkinson, "Environmental effects of the use of

oil-based drilling muds in the north sea," *Marine Pollution Bulletin*, vol. 15, no. 10, pp. 363 – 370, 1984.

[85] D. E. O'Brien and M. E. Chenevert, "Stabilizing sensitive shales with inhibited, potassium-based drilling fluids," *Journal of Petroleum Technology*, vol. 25, pp. 1089–1100, 1973.

[86] L. Bailey, M. Keall, A. Audibert, and J. Lecourtier, "Effect of clay/polymer interactions on shale stabilization during drilling," *Langmuir*, vol. 10, no. 5, pp. 1544–1549, 1994.

[87] R. Zolfaghari, A. A. Katbab, J. Nabavizadeh, R. Y. Tabasi, and M. H. Nejad, "Preparation and characterization of nanocomposite hydrogels based on polyacrylamide for enhanced oil recovery applications," *Journal of Applied Polymer Science*, vol. 100, no. 3, pp. 2096–2103, 2006.

[88] R. Steiger, "Fundamentals and use of potassium/polymer drilling fluids to minimise drilling and completion problems associated with hydratable clays," *Journal of Petroleum Technology*, vol. 34, pp. 1661–1670, 1982.

[89] P. Reid, B. S. C. R. Dolan, and S. S. D. Cliffe, "Mechanism of shale inhibition by polyols in water based drilling fluids," *Society of Petroleum Engineers*, vol. 23, pp. 393–404, 1995.

[90] L. Quintero, "An overview of surfactant applications in drilling fluids for the petroleum industry," *Journal of dispersion science and technology*, vol. 23, no. 1-3, pp. 393–404, 2002.

[91] L. R. Rudnick and R. L. Shubkin, *Synthetic Lubricants And High- Performance Functional Fluids*. CRC Press, 1999.

[92] S. Liu, X. Mo, C. Zhang, D. Sun, and C. Mu, "Swelling inhibition by polyglycols in montmorillonite dispersions," *Journal of Dispersion Science and Technology*, vol. 25, no. 1, pp. 63–66, 2004.

[93] E. Van Oort, D. Ripley, I. Ward, J. Chapman, R. Williamson, and M. Aston, "Silicate-based drilling fluids: competent, cost-effective and benign solutions to wellbore stability problems," in *IADC/SPE drilling conference*, pp. 189–204, 1996.

[94] P. P. Scott, "Shale hydration inhibitors for clear," Jan. 16 1962. US Patent 3,017,351.

[95] H. C. Greenwell, M. J. Harvey, P. Boulet, A. A. Bowden, P. V. Coveney, and A. Whiting, "Interlayer structure and bonding in nonswelling primary amine intercalated clays," *Macromolecules*, vol. 38, no. 14, pp. 6189–6200, 2005.

[96] J. Gieseking, "The mechanism of cation exchange in the montmorillonite-beidellite-nontronite type of clay minerals," *Soil Science*, vol. 47, no. 1, pp. 1–14, 1939.

[97] R. F. Miller, "Shale hydration inhibition agent(s) and method of use," 02 2012.

[98] B. Peng, P.-Y. Luo, W.-Y. Guo, and Q. Yuan, "Structureproperty relationship of polyetheramines as clay-swelling inhibitors in water-based drilling fluids," *Journal of Applied Polymer Science*, vol. 129, no. 3, pp. 1074–1079, 2013.

[99] Y. Xuan, G. Jiang, Y. Li, J. Wang, and H. Geng, "Inhibiting effect of dopamine adsorption and polymerization on hydrated swelling of montmorillonite," *Colloids and Surfaces A: Physicochemical and Engineering Aspects*, vol. 422, no. 0, pp. 50 – 60, 2013.

[100] A. J. Son, V. S. Neal, and C. M. Garvey, "Shale and salt stabilizing drilling fluid," July 2 1985. US Patent 4,526,693.

[101] A. D. Patel and H. C. McLaurine, "Drilling fluid additive and method for inhibiting hydration," June 13 1995. US Patent 5,424,284.

[102] A. D. Patel, C. J. Thaemlitz, H. C. McLaurine, and E. Stamatakis, "Drilling fluid additive and method for inhibiting hydration," June 1 1999. US Patent 5,908,814.

[103] M. Hodder, A. Popplestone, P. Gwynne, and D. Reynolds, "High-performance, water-based drilling fluid helps achieve early oil with lower capital expenditure," *Offshore Europe*, 2005.

[104] A. D. Patel, "Low toxicity shale hydration inhibition agent and method of use," May 10 2011. US Patent 7,939,473.

[105] J. Enderby, S. Cummings, G. Herdman, G. Neilson, P. Salmon, and N. Skipper, "Diffraction and the study of aqua ions," *Journal of Physical Chemistry*, vol. 91, no. 23, pp. 5851–5858, 1987.

[106] G. Squires, *Introduction to the Theory of Thermal Neutron Scattering*. Cambridge University Press, 2012.

[107] H. E. Fischer, A. C. Barnes, and P. S. Salmon, "Neutron and x-ray diffraction studies of liquids and glasses," *Reports on Progress in Physics*, vol. 69, no. 1, p. 233, 2006.

[108] M. Bee, *Quasielastic neutron scattering*. United Kingdom: Adam Hilger, 1988.

[109] M. Be, "A physical insight into the elastic incoherent structure factor," *Physica B: Condensed Matter*, vol. 182, no. 4, pp. 323 – 336, 1992. Quasielastic Neutron Scattering.

[110] P. L. Hall and D. Ross, "Incoherent neutron scattering functions for random jump diffusion in bounded and infinite media," *Molecular Physics*, vol. 42, no. 3, pp. 673–682, 1981.

[111] K. S. Singwi and A. Sjölander, "Diffusive motions in water and cold neutron scattering," *Phys. Rev.*, vol. 119, pp. 863–871, Aug 1960.

[112] C. T. Chudley and R. J. Elliott, "Neutron scattering from a liquid on a jump diffusion model," *Proceedings of the Physical Society*, vol. 77, no. 2, p. 353, 1961.

[113] F. Mezei, "Neutron spin echo: A new concept in polarized thermal neutron techniques," *Zeitschrift fr Physik*, vol. 255, no. 2, pp. 146–160, 1972.

[114] M. Rekveldt, "Novel {SANS} instrument using neutron spin echo," *Nuclear Instruments and Methods in Physics Research Section B: Beam Interactions with Materials and Atoms*, vol. 114, no. 34, pp. 366 – 370, 1996.

[115] J. Turner, A. Soper, and J. Finney, "A neutron-diffraction study of tetramethylammonium chloride in aqueous solution," *Molecular Physics*, vol. 70, no. 4, pp. 679–700, 1990.

[116] J. Turner, A. Soper, and J. Finney, "Water structure in aqueous solutions of tetramethylammonium chloride," *Molecular Physics*, vol. 77, no. 3, pp. 411–429, 1992.

[117] A. Soper, "Inelasticity corrections for time-of-flight and fixed wavelength neutron diffraction experiments," *Molecular Physics*, vol. 107, no. 16, pp. 1667–1684, 2009.

[118] C. A. Jeffery and P. H. Austin, "A new analytic equation of state for liquid water," *The Journal of Chemical Physics*, vol. 110, no. 1, pp. 484–496, 1999.

[119] A. Soper, *GudrunN and GudrunX*
*Programs for correcting raw neutron and x-ray total scattering data to differential cross section*, 2012.

[120] A. Soper, "Empirical potential monte carlo simulation of fluid structure," *Chemical Physics*, vol. 202, no. 23, pp. 295 – 306, 1996.

[121] A. Soper, "Partial structure factors from disordered materials diffraction data: An approach using empirical potential structure refinement," *Physical Review B*, vol. 72, no. 10, p. 104204, 2005.

[122] A. Soper, "The radial distribution functions of water and ice from 220 to 673 k and at pressures up to 400 mpa," *Chemical Physics*, vol. 258, no. 2, pp. 121–137, 2000.

[123] H. S. Frank and W.-Y. Wen, "Ion-solvent interaction. structural aspects of ion-solvent interaction in aqueous solutions: a suggested picture of water structure," *Discuss. Faraday Soc.*, vol. 24, pp. 133–140, 1957.

[124] D. T. Bowron and J. L. Finney, "Structure of a salt–amphiphile–water solution and the mechanism of salting out," *The Journal of Chemical Physics*, vol. 118, no. 18, pp. 8357–8372, 2003.

[125] A. K. Soper and K. Weckstrom, "Ion solvation and water structure in potassium halide aqueous solutions," *Biophysical Chemistry*, vol. 124, no. 3, pp. 180 – 191, 2006.

[126] J. Stewart, "Mopac," 2007.

[127] H. J. C. Berendsen, J. R. Grigera, and T. P. Straatsma, "The missing term in effective pair potentials," *The Journal of Physical Chemistry*, vol. 91, no. 24, pp. 6269–6271, 1987.

[128] S. Dixit, J. Crain, W. Poon, J. Finney, and A. Soper, "Molecular segregation observed in a concentrated alcohol–water solution," *Nature*, vol. 416, no. 6883, pp. 829–832, 2002.

[129] A. K. Soper, "The radial distribution functions of water as derived from radiation total scattering experiments: is there anything we can say for sure?," *ISRN Physical Chemistry*, vol. 2013, 2013.

[130] A. Soper, J. Turner, and J. Finney, "Solute-solute correlations in aqueous solutions of tetramethylammonium chloride," *Molecular Physics*, vol. 77, no. 3, pp. 431–437, 1992.

[131] R. Mancinelli, A. Botti, F. Bruni, , M. A. Ricci*, and A. K. Soper, "Hydration of sodium, potassium, and chloride ions in solution and the concept of structure maker/breaker," *The Journal of Physical Chemistry B*, vol. 111, no. 48, pp. 13570–13577, 2007. PMID: 17988114.

[132] D. H. Powell, A. C. Barnes, J. E. Enderby, G. W. Neilson, and P. S. Salmon, "The hydration structure around chloride ions in aqueous solution," *Faraday Discussions of the Chemical Society*, vol. 85, pp. 137–146, 1988.

[133] Y. Marcus, "Effect of ions on the structure of water: structure making and breaking," *Chemical reviews*, vol. 109, no. 3, pp. 1346–1370, 2009.

[134] W. Wang, X. Bian, J. Qin, L. Zhang, and Y. Ye, "Gaussian peaks decomposing of simple liquids rdf," *Science in China Series E: Technological Sciences*, vol. 42, no. 6, pp. 631–636, 1999.

[135] W. Seidl and J. Breu, "Single crystal structure refinement of tetramethylammonium-hectorite," *Zeitschrift für Kristallographie/International journal for structural, physical, and chemical aspects of crystalline materials*, vol. 220, no. 2/3/2005, pp. 169–176, 2005.

[136] R. Martos-Villa, S. Guggenheim, and C. I. Sainz-Díaz, "Interlayer water molecules in organocation-exchanged vermiculite and montmorillonite: A case study of tetramethylammonium," *American Mineralogist*, vol. 98, no. 8-9, pp. 1535–1542, 2013.

[137] A. Vahedi-Faridi and S. Guggenheim, "Crystal structure of tetramethylammonium-exchanged vermiculite," *Clays and Clay minerals*, vol. 45, no. 6, pp. 859–866, 1997.

[138] R. Dalgliesh, S. Langridge, J. Plomp, V. de Haan, and A. van Well, "Offspec, the isis spin-echo reflectometer," *Physica B: Condensed Matter*, vol. 406, no. 12, pp. 2346

– 2349, 2011. ¡ce:title¿Proceedings of the 8th International Workshop on Polarised Neutrons for Condensed Matter Investigation¡/ce:title¿.

[139] W. W. Kagunya, "Properties of water adsorbed in anionic clays: a neutron scattering study," *The Journal of Physical Chemistry*, vol. 100, no. 1, pp. 327–330, 1996.

[140] C. Carlile and M. A. Adams, "The design of the iris inelastic neutron spectrometer and improvements to its analysers," *Physica B: Condensed Matter*, vol. 182, no. 4, pp. 431–440, 1992.

[141] H. C. Greenwell, W. Jones, S. L. Rugen-Hankey, P. J. Holliman, and R. L. Thompson, "Efficient synthesis of ordered organo-layered double hydroxides," *Green Chemistry*, vol. 12, no. 4, pp. 688–695, 2010.

[142] . Steven P. Newman, . Samuel J. Williams, . Peter V. Coveney, *, , and W. Jones, "Interlayer arrangement of hydrated mgal layered double hydroxides containing guest terephthalate anions: comparison of simulation and measurement," *The Journal of Physical Chemistry B*, vol. 102, no. 35, pp. 6710–6719, 1998.

[143] Science and T. F. Council, "Iris instrument," October 2015.

[144] "Mi swaco, a schlumberger company," 2012.

[145] Omega®, "Non-contact displacement sensor," November 2015.

[146] S. Saba, J.-D. Barnichon, Y.-J. Cui, A. M. Tang, and P. Delage, "Microstructure and anisotropic swelling behaviour of compacted bentonite/sand mixture," *Journal of Rock Mechanics and Geotechnical Engineering*, vol. 6, no. 2, pp. 126 – 132, 2014.

[147] A. Kalra, N. Tugcu, S. M. Cramer, , and S. Garde*, "Salting-in and salting-out of hydrophobic solutes in aqueous salt solutions," *The Journal of Physical Chemistry B*, vol. 105, no. 27, pp. 6380–6386, 2001.

[148] . Robert S. Maxwell, R. K. Kukkadapu, J. E. Amonette, , and H. Cho*, "2h solid-state nmr investigation of terephthalate dynamics and orientation in mixed-anion hydrotalcite-like compounds," *The Journal of Physical Chemistry B*, vol. 103, no. 25, pp. 5197–5203, 1999.